

MEASUREMENT AND PREDICTION OF LOW-FREQUENCY NOISE IN
INDUSTRIAL WORKROOMS

by

GALEN WONG

B.Sc., The University of British Columbia, 2002

A THESIS SUBMITTED IN THE PARTIAL FULFILMENT OF
THE REQUIREMENTS FOR THE DEGREE OF

MASTER OF APPLIED SCIENCE

in

THE FACULTY OF GRADUATE STUDIES

(Mechanical Engineering)

THE UNIVERSITY OF BRITISH COLUMBIA

January, 2006

© Galen Wong, 2006

Abstract

Workers in industrial workrooms are routinely subjected to high levels of low-frequency noise (below 200 Hz) caused by machinery, ventilation systems, and other noise-generating sources. Although low-frequency noise is not usually considered to be damaging to hearing unless at very high, sustained levels, it may cause other problems, such as masking warning sounds, hindering communication, general annoyance and uneasiness, and nausea when accompanied by low-frequency vibrations. It is thus of interest to investigate and determine the characteristics of low-frequency sound propagation in such facilities for the purpose of better understanding how to control the sound using active noise control, since passive methods are often ineffective in controlling low-frequency sound. Prediction models can be used in helping to predict the benefits of and to optimize control measures. Two main factors alter the sound in workrooms at low frequencies – the boundary conditions of the room, and the obstacles in the room (the fittings) – and should be accounted for in prediction models. Thus, to investigate the propagation of low-frequency noise in workrooms, experiments were performed in three situations; a real workroom (empty and fitted), a scale-model workroom (empty and fitted), and a semi-free-field environment (a hemi-anechoic chamber -- empty and fitted). Prediction models were employed to predict the sound

fields in the measured configurations. Modal and image-phase prediction models were used to model the empty configuration, while a finite-element model was used to model the effects of fittings. It was shown that fittings significantly alter the low-frequency sound field in the real workroom with octave-band-limited noise. The scale-model test results showed relatively little influence of the fittings on the low-frequency sound field, with the same noise. The hemi-anechoic chamber results, without the effect of the room, indicate some small effects of the fittings. The room plays a larger role in affecting the sound field than do the fittings. The prediction results are discussed. It has proven difficult to accurately model the room and its boundary conditions with the modal and image-phase prediction models. Finite-element methods can be used to model very low-frequency effects, but memory limitations prevent modeling at higher frequencies.

Table of Contents

| | |
|---|-----|
| Abstract..... | ii |
| Table of Contents..... | iv |
| List of Tables..... | vi |
| List of Figures..... | vii |
| Acknowledgements..... | xi |
| Chapter 1 Introduction..... | 1 |
| 1.1 Low-Frequency Noise and Workrooms..... | 1 |
| 1.2 Scattering of Sound by Fittings..... | 8 |
| 1.3 General Room Acoustics and Boundary Conditions..... | 11 |
| 1.4 Control Methods..... | 16 |
| 1.5 Research Objectives..... | 19 |
| Chapter 2 Workroom Measurements..... | 21 |
| 2.1 Real Workroom..... | 21 |
| 2.1.1 Details of the Machine Shop..... | 21 |
| 2.1.2 Equipment Setup..... | 23 |
| 2.1.3 Measurement Results in the Workroom..... | 26 |
| 2.1.4 Low-Frequency Source Tests..... | 27 |
| 2.1.5 Omnidirectional Source Tests..... | 34 |
| 2.1.6 Summary..... | 38 |
| 2.2 Scale Model Measurements..... | 38 |
| 2.2.1 Scale Modeling Theory..... | 38 |
| 2.2.2 Scale Model Setup..... | 40 |
| 2.2.3 Results..... | 44 |
| 2.2.4 Summary..... | 53 |
| 2.3 Comparison between scale-model and real workroom measurements..... | 53 |
| 2.4 Anechoic Chamber Tests..... | 54 |
| 2.4.1 Equipment Setup..... | 54 |
| 2.4.2 Results and Discussion..... | 55 |
| 2.5 Comparison between the Anechoic Chamber and Scale-Model Measurements .. | 59 |

| | |
|--|-----|
| Chapter 3 Prediction | 61 |
| 3.1 Approaches | 61 |
| 3.2 The Modal Model | 62 |
| 3.2.1 Implementation | 63 |
| 3.3 Image-Phase Model | 64 |
| 3.3.1 Validation..... | 67 |
| 3.3.2 Comparison between the Modal Model and the Image Phase Model | 69 |
| 3.3.3 Scale Model | 81 |
| 3.4 Modeling the Fittings using Finite Elements | 84 |
| 3.4.1 The Finite-Element Model..... | 85 |
| 3.4.2 Fitted Anechoic Fitted Room Results | 86 |
| 3.4.3 Summary..... | 96 |
| Chapter 4 Conclusion..... | 97 |
| 4.1 Conclusions..... | 97 |
| 4.2 Future Work..... | 100 |
| Bibliography | 102 |
| Appendix A Source Characterization | 104 |
| A.1 Low-frequency source..... | 104 |
| A.2 Scale Model Source | 107 |
| Appendix B Green's Function Solution for the Helmholtz Equation..... | 111 |
| Appendix C Transfer Matrix Impedance Calculation..... | 115 |
| Appendix D Pictures at X- Positions | 118 |
| Appendix E Matlab Code..... | 121 |

List of Tables

| | |
|---|----|
| Table 2.1. Measured RT (seconds) of the real workroom, with the low-frequency source and the omnidirectional source. | 27 |
| Table 2.2. Calculated absorption coefficients of the real workroom, with the low-frequency source and the omnidirectional source..... | 27 |
| Table 2.3. Positions of the measurement lines taken in the scale model room; distances X, Y and Z are as shown on Figure 5 above..... | 42 |
| Table 2.4. Reverberation times (sFS) measured in the scale model room when empty and fitted with small and large fittings. | 44 |
| Table 2.5. Absorption coefficients calculated from the reverberation times measured in the scale model room when empty and fitted with small and large fittings. | 45 |
| Table 3.1 Average properties of plywood, as used in the calculation of the impedance of the scale-model walls..... | 71 |
| Table 3.2. Complex impedances and reflection coefficients calculated by the transfer-matrix method using the scale model plywood boundary properties. | 72 |

List of Figures

| | |
|--|----|
| Figure 2.1 Dimensions and layout of the real workroom. | 22 |
| Figure 2.2 Flow diagram of the equipment setup in the real workroom measurements... .. | 24 |
| Figure 2.3 The X-positions in the real workroom..... | 25 |
| Figure 2.4. 63Hz pure tone measured at 1m intervals along Line 1 (a) and Line 2 (b) in the workshop..... | 29 |
| Figure 2.5. 31.5, 63 and 125 Hz octave band noise measured at 1 m intervals along Line 1 in the workshop when empty and fitted..... | 31 |
| Figure. 2.6. Measured sound pressure levels in the empty and fitted conditions at X-positions 1 to 6 in the workroom. | 32 |
| Figure 2.7. Measured sound pressure levels in the empty and fitted conditions at X-positions 7 to 12 in the workroom. | 33 |
| Figure 2.8. Octave band sound pressure level measured along Line 1 of white noise output by omnidirectional source..... | 35 |
| Figure 2.9. Octave band sound pressure level measured along Line 1 of white noise output by omnidirectional source..... | 36 |
| Figure 2.10. Measured sound pressure level at the X-positions in the workroom. The source output white noise and sound level measurements were recorded at 1/3 octave-band intervals. | 37 |
| Figure 2.11. Diagram of the measurement lines in the scale model room; distances X, Y and Z are listed in Table 5 below..... | 42 |
| Figure 2.12. The empty scale model room set up at 1/8th scale, 30mFS x 15mFS x 7.5mFS. | 43 |
| Figure 2.13. The large (a) and small (b) fittings in the scale model room. The source placement can be seen in the photo with the large fittings. | 43 |

| | |
|---|----|
| Figure 2.14. Measurements along Line 1 with the source output at 31.5, 63, 125 and 250 Hz pure tone. (Solid Black line – Empty, Dotted line – Small Fittings, Grey line – Large Fittings)..... | 46 |
| Figure 2.15. Measurements along Line 2 with the source output at 31.5, 63, 125 and 250 Hz pure tone. (Solid Black line – Empty, Dotted line – Small Fittings, Grey line – Large Fittings)..... | 47 |
| Figure 2.16. Measurements along line 3 of the source output at 31.5, 63, 125 and 250Hz pure tone. (Solid Black line – Empty, Dotted line – Small Fittings, Grey line – Large Fittings)..... | 48 |
| Figure 2.17. Measurements along Line 1 of the source output at 31.5, 63, 125 and 250Hz octave band. (Solid Black line – Empty, Dotted line – Small Fittings, Grey line – Large Fittings)..... | 50 |
| Figure 2.18. Measurements along line 2 of the source output at 31.5, 63, 125 and 250HzOB. (Solid Black line – Empty, Dotted line – Small Fittings, Grey line – Large Fittings)..... | 51 |
| Figure 2.19. Measurements along line 3 of the source output at 31.5, 63, 125 and 250HzOB. (Solid Black line – Empty, Dotted line – Small Fittings, Grey line – Large Fittings)..... | 52 |
| Figure 2.20. Measurements along Line 1 of the source output at 31.5, 63, 125 and 250 Hz pure tone. (Solid Black Line – Empty, Dashed Line – Small Fittings, Dotted Line – Large Fittings) | 56 |
| Figure 2.21. Measurements along Line 2 of the source output at 31.5, 63, 125 and 250 Hz pure tone. (Solid Black Line – Empty, Dashed Line – Small Fittings, Dotted Line – Large Fittings) | 57 |
| Figure 2.22. Measurements along line 2 of the source output at 31.5, 63, 125 and 250 Hz pure tone. (Solid Black Line – Empty, Dashed Line – Small Fittings, Dotted Line – Large Fittings) | 58 |
| Figure 3.1. Illustration of the image-phase model concept..... | 65 |
| Figure 3.2. Test for convergence of the Modal Model. | 68 |

| | |
|--|----|
| Figure 3.3. Comparison of the modal model with the Image-Phase model..... | 69 |
| Figure 3.4. 31.5Hz in the 5x5x1 room, with 75 images and 100,000 modes. | 73 |
| Figure 3.5. 31.5Hz in the 5x5x1 room, with 175 images and 100,000 modes. | 74 |
| Figure 3.6. 63Hz in the 5x5x1 room, with 75 images and 100,000 modes. | 75 |
| Figure 3.7. 63Hz in the 5x5x1 room, with 175 images and 100,000 modes. | 76 |
| Figure 3.8. 125Hz in the 5x5x1 room, with 75 images and 100,000 modes. | 77 |
| Figure 3.9. 125Hz in the 5x5x1 room, with 175 images and 100,000 modes. | 78 |
| Figure 3.10. 250Hz in the 5x5x1 room, with 75 images and 100,000 modes. | 79 |
| Figure 3.11. 250Hz in the 5x5x1 room, with 75 images and 100,000 modes. | 80 |
| Figure 3.12 Measured and predicted sound pressure levels along Line 1 in the scale model room. Solid line indicates measured, dashed is modal model, and dotted is image-phase model. | 82 |
| Figure 3.13 Measured and predicted sound pressure level along Line 2 in the scale model room. Solid line indicates measured, dashed is modal model, and dotted is image- phase model. | 83 |
| Figure 3.14 Measured and predicted sound pressure level along Line 2 in the scale model room. Solid line indicates measured, dashed is modal model, and dots is image- phase model. | 84 |
| Figure 3.15. Comparison of the 31.5 HzFS hemi-anechoic chamber measurement (solid line) with the FEM prediction (dotted line) in the empty room..... | 88 |
| Figure 3.16. Comparison of the 63 HzFS hemi-anechoic chamber measurement (solid line) with the FEM prediction (dotted line) in the empty room..... | 89 |
| Figure 3.17. Comparison of the 31.5 Hz hemi-anechoic chamber measurement (solid line) with the FEM prediction (dotted line) with small fittings. | 92 |
| Figure 3.18. Comparison of the 31.5 Hz hemi-anechoic chamber measurement (solid line) with the FEM prediction (dotted line) with large fittings. | 93 |

| | |
|---|-----|
| Figure 3.19. Comparison of the 63 Hz hemi-anechoic chamber measurement (solid line) with the FEM prediction (dotted line) with small fittings. | 94 |
| Figure 3.20. Comparison of the 63 Hz hemi-anechoic chamber measurement (solid line) with the FEM prediction (dotted line) with large fittings. | 95 |
| Figure A1 The low-frequency source. | 104 |
| Figure A2 Frequency response of the low-frequency source, as measured at 1m, using MLSSA. | 105 |
| Figure A3 Directivity of the low-frequency source with a 63Hz pure tone output. | 106 |
| Figure A4 Directivity of the low-frequency source with a 31.5 Hz Octave Band filtered noise. | 106 |
| Figure A5 Directivity of the low-frequency source with a 63 Hz Octave Band filtered noise signal. | 107 |
| Figure A6 Frequency response of the scale model source, measured using MLSSA | 108 |
| Figure A7 Directivity of the scale model source, measured using pure tones. | 109 |
| Figure A8 Directivity of the scale model source, measured with octave-band noise. | 110 |

Acknowledgements

I have faced many challenges throughout my time in university, but none which have been as difficult as those faced during my time working on this research. I am very thankful and in great debt to the many people who have helped and supported me during this time.

First, my supervisor, Professor Murray Hodgson, has kept a watchful eye on me since I first approached him for a summer-student position in his laboratory. My interest in acoustics grew tremendously under his guidance and teaching, and I have learned so much from him over the years. Murray, you're a great teacher and mentor, and I hope to keep in collaboration with you in the future.

Thanks go to Desheng Li for helping me so much when I started this work, with our many discussions on acoustics and your help with my experimental setup and measurements. You were also wonderful company to have on our several trips together to conferences and performing measurements.

Vincent Valeau, your knowledge of acoustical theory astounds me, and I wish I could manipulate equations and explain difficult theory as well as you could. I wish I had more time to spend with you to get to know you better. Thank you for your invaluable counsel and advice.

Mom and Dad – I really was at school at all hours of the day and night whenever I wasn't at home. Thank you for your patience and support throughout my long school career. Mom, I wish I could explain better to you what it is that I do - at least I know that you understand that this is what I love doing, and I thank you for giving me the freedom and encouragement to pursue my dream.

Ann Nakashima, your encouragement has always helped to get me through my tough times during this work. Thank you for enduring my many ramblings on acoustics – you're one of the few who understands me, and is willing to put up with me. I hope we can have many more "Scrabble nights" and coffee runs in the future.

Izzy Li, I haven't known you that long, but it seems like we've known each other for ages! Our carpooling and daily morning coffee runs will remain some of the most memorable times of my university career (believe it or not). And thank you for introducing me to Ultimate!

Galen Wong, January 2006.

Chapter 1

Introduction

1.1 Low-Frequency Noise and Workrooms

Low-frequency noise is prevalent in many industrial workrooms due to its emission from sources such as machinery, ventilation systems and vehicles. This noise comes from the many engines and motors and other vibrating machinery, as well as from the walls and enclosures that are excited mechanically by the vibrating machinery. Workers working in such areas are routinely subjected to high levels of low-frequency noise - often over long exposure times. Because hearing damage is most commonly caused by loud mid- and high-frequency sounds, there has been little focus on protection from low-frequency noise. While many safety and health regulations have been implemented to lessen the impact of mid- and high-frequency noise on workers, low-frequency noise has commonly been ignored as a health and safety issue in the community and workplace. This is evident in many of the current occupational workplace regulations, which primarily use the A-weighted sound pressure level as a measure of the noise exposure that workers endure. The use of this weighting scheme attempts to account for the frequency

dependent sensitivity of human ears, because they are more sensitive at mid- and high-frequencies than at low frequencies. The generally accepted range of human hearing spans the frequencies from 20 Hz to 20 kHz. At very high and very low frequencies, the level must be proportionately higher to be able to perceive it at the same level as at the mid-frequencies and for it to cause the same hearing damage. This is shown in the Fletcher-Munson measured equal-loudness contours [1] of Figure 1.1. These contours show the level of sound that is perceived to be at the same

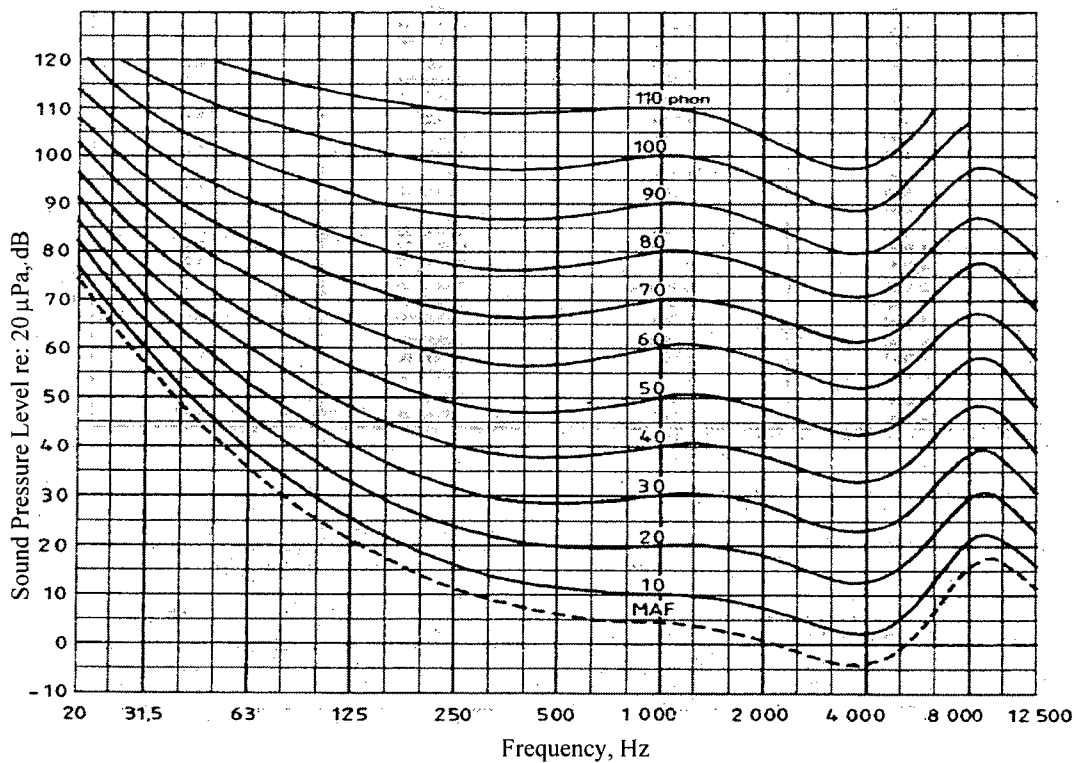


Figure 1.1. Fletcher-Munson equal loudness contours. MAF is the Minimum Audible Field [1]

loudness at different frequencies. The lowest curve is the threshold of audibility, which is the minimum perceptible level of a tone that can be detected at each frequency, over the entire range of the ear. According to Figure 1.1, for sound of 20 Hz to be audible, its intensity must exceed approximately 70 dB (re: 10^{-12} W/m²). For frequencies above 20 Hz, levels lower than 70 dB are detectable. The detection of low-frequency sound, however, does not occur solely through the external ear – much of the perception of low-frequency noise occurs through indirect methods, such as through vibrations in bones, tactile senses or resonances in body organs [2]. Thus, hearing-protection devices, commonly relied on for industrial noise control, are not effective against these low-frequency sounds which are sometimes felt more than heard. Moreover, they mask detection of the more important mid- and high-frequency sounds used for communication [2]. Infrasound, sound which is below the accepted lowest limit of human hearing – below 20 Hz – also has the ability to affect the human body. Vibrations caused by low-frequency noise or infrasound from below 0.5 Hz and up to 200 Hz are detectable and have some influence on the overall perception of the noise [2]. Increasingly, C-weighted sound pressure levels are being recommended and used in assessing workplace noise exposure, but the most widely used limit is still based on the A-weighting. The C-weighting discounts only the very low frequencies and infra-sound, while the A-weighting discounts some of the mid- as well as much of the low-frequencies.

Prolonged exposure to high levels of low-frequency noise has been shown to cause significant hearing damage, not in the frequency range of the noise source, but in the more important mid-frequency range, at 1k and 2k Hz [3, 4]. Moreover, it was found that, in tests whereby subjects were subjected to high levels of low-frequency noise, “a much greater area of the cochlea [the organ containing the detectors that send auditory information to the brain] is affected by 63 Hz than by 4 kHz, and therefore, the number of sensory cells and other elements at “potential risk” is significantly greater with low-frequency exposures” [4]. Studies have also shown that exposure to moderate levels of low-frequency noise causes adverse effects on the human body and well-being, increasing levels of agitation and annoyance, and affecting the ability to sleep well during exposure at nighttime [5]. In a workplace setting, increased agitation and annoyance can cause a decrease in a worker’s concentration – which may have dangerous consequences. It has also been reported that high levels of low-frequency noise decreases the ability to hear and comprehend speech and other acoustic signals due to a masking effect and modulation of voices [5]. In addition, infrasound adversely affects the human body through indirect effects such as when it induces motion sickness and nausea. Changes in heart rate have been measured, but this may be linked to a habituation effect in the subjects, linked to the environment in which they were exposed to this long-term noise exposure. Other long-term effects of low-frequency noise include elevated blood-pressure levels and slight increases in heart-disease risk [5]. Overall, these effects can

cause productivity loss in the workplace through decreased concentration, and may hinder communication and the ability to hear warning signals. Hearing loss is also possible in extreme cases. The ability to decrease worker exposure to low-frequency noise is thus of great importance.

The exposure of workers to low-frequency noise is compounded by the characteristics of its propagation. Compared to high-frequency sounds, low-frequency sounds are much less attenuated by obstacles such as walls and structures, and they display modal response characteristics. Modal responses occur in enclosed spaces, where the wall boundaries reflect the sound waves, and through wave addition and cancellation cause peaks and dips in the sound pressure level throughout the room. For objects much smaller than the wavelength of the sound, the waves are able to diffract or 'bend' easily around the object. Also, low-frequency waves have the ability to travel large distances outdoors with little air absorption and little ground attenuation. This causes problems in the ability to control low-frequency noise, because of its inherent ability to diffract easily around the obstacles in a room (called the 'fittings'), and its difficulty in being absorbed in a material. Low-frequency sounds, because of the nature of their long wavelengths, also tend to radiate in an omnidirectional pattern from the source, while high frequencies are more directional – the directivity of the source is dependent on the size of the radiating surface of the source relative to the sound wavelength and the diffraction

properties of the surrounding area. Often, a machine is only one or two meters in length, and the wavelength of, for example, a 31.5 Hz wave is about 11 meters.

In order to be able to determine methods to decrease worker exposure to low-frequency noise in industrial workrooms, the characteristics of low-frequency sound and its propagation must be studied. This involves the understanding of the effects of the characteristics of the low-frequency noise generated by the machines, the source location in the room, as well as the room boundaries itself. We must also consider other possible impediments to the propagation of the low-frequency noise in the workroom - namely the fittings, which modify the sound field in the room due to the reflection and scattering of the sound energy. These characteristics are difficult to account for since they are different for each workroom configuration and are dependent on many different factors. The prediction of low-frequency noise propagation in workrooms is also useful, to aid in the design or modification of workrooms in order to decrease worker exposure to low-frequency noise.

To be able to predict workroom noise, we must consider the general characteristics of workrooms and the low-frequency sound propagation issues and effects. The shapes and types of surfaces of the workroom are two of the main characteristics of workrooms which must be considered, since they affect greatly the sound field within the room at low frequencies. Workrooms are typically characterized by large volumes and complex shapes, enclosing industrial sites such as factories and machine shops. The

surfaces of the workroom buildings usually consist of concrete, cinder block, metal paneling (possibly corrugated) or gypsum drywall for the walls, while the floor is usually bare concrete. The roof is usually constructed of similar metal paneling to the walls (and also possibly corrugated). Spray-on absorption or acoustically absorbent panels sometimes line the walls or roof panels to increase the sound absorption within the room. Also, there are often windows and large roll-up equipment doors along the walls. Office space sometimes takes up significant space in the workroom.

The noise sources in workrooms range from generators and compressors and ventilation outlets to any of a number of machines that generate noise in the industrial building. Many of the sources generate tonal noise, related to the rotational frequency of the machine components, rather than broadband noise. This generated noise is often of low frequency, non-varying in frequency and persistent for long periods, if the machine is running full-time. Other types of noise often found in workrooms include impulsive sounds such as those that occur when two hard materials collide and there is a short, sharp noise produced though this tends to be of mainly high frequency.

In workrooms, the noise generating machines may also serve as the fittings that block and scatter the sound. Other obstacles to the propagating sounds in the room may be stockpiles of material, benches, etc., and these are often of irregular shapes and sizes. The characterization of the fittings in a workroom is very difficult, as they are often

numerous, and each fitting will reflect and modify the sound energy incident upon it in a different way. The next section discusses this in more detail.

1.2 Scattering of Sound by Fittings

At mid and high frequencies, fittings reflect and scatter incident sound. Hodgson [6] found that the introduction of fittings in industrial workrooms decreases the reverberation time (RT) (the RT is defined as the time required for the level of the sound to decay by 60 dB) in a room. As well, with the introduction of fittings, an increase in the rate of sound decay with increasing distance from the source has been measured. However, backscattering - the reflection of sound energy back to the source - has been found to increase the sound pressure levels in the area near the source. The decrease in RT is due to an increase in the effective sound absorption in the room because of the fittings, resulting in higher temporal sound decay rates. The higher effective sound absorption in the room is a result of the increase in scattering and resulting propagation directions, which modifies the angles of incidence of sound on the absorbent surfaces [6].

Several prediction models have been developed to account for fittings in the prediction of the sound field at mid and high frequencies in rooms [7] but, to the author's knowledge, no previous work has been performed to characterize or model the effects of the industrial fittings on low-frequency sound.

The scattering of sound occurs when a sound wave encounters an obstacle, reflects from it, and interferes with the original wave. The deflected wave is called the scattered wave, and this wave spreads out from the obstacle in all directions; the spreading pattern depends on the ratio of the wavelength to the size of the obstacle, and on the shape of the obstacle. It is possible to calculate the scattered wave for simple cases – an example is the scattering caused by a cylinder of radius a , of a plane wave traveling perpendicular to its axis [8]. In cylindrical coordinates, with the cylinder centered at the origin, the plane pressure wave, p_p , is defined as,

$$p_p = P_o e^{ik(r \cos \phi - ct)}, \quad (1.1)$$

where k is the wavenumber, $k=2\pi f/c$, related to the frequency f , of the wave, and the speed of sound in air, c . $P_o = \sqrt{\rho c I}$, where I is the intensity of the plane wave and ρ is the density of air. The plane wave in turn, can be expressed in terms of cylindrical waves,

$$p_p = P_o \left[J_0(kr) + 2 \sum_{m=1}^{\infty} i^m \cos(m\phi) J_m(kr) \right] e^{-2\pi i vt}, \quad (1.2)$$

with the radial velocity of the wave as,

$$u_{pr} = \frac{P_o}{\rho c} \left\{ i J_1(kr) + \sum_{m=1}^{\infty} i^{m+1} [J_{m+1}(kr) - J_{m-1}(kr)] \cos(m\phi) \right\} e^{-2\pi i vt}, \quad (1.3)$$

where the J_n are Bessel functions.

The cylinder acts to distort this plane wave, which passes around it, and also causes a scattered wave to be propagated outward from the surface of the cylinder. The solution for the pressure and velocity of the scattered wave can be shown to be,

$$p_s = -\sqrt{\frac{2\rho c I a}{\pi r}} \frac{1}{\sqrt{ka}} \left(\sum_{m=0}^{\infty} \varepsilon_m \sin(\gamma_m) e^{-i\gamma_m} \cos(m\phi) \right) e^{ik(r-ct)}, \quad (1.4)$$

and

$$u_s = \frac{p_s}{\rho c}, \quad (1.5)$$

with the boundary condition such that, at the surface of the cylinder, the velocity of the wave is zero (a rigid cylinder surface). The s subscript indicates the scattered wave. The resulting intensity of the scattered wave is,

$$\Gamma_s = \frac{I a}{\pi r} \left| \frac{1}{ka} \sum_{m,n=0}^{\infty} \varepsilon_m \varepsilon_n \sin(\gamma_m) \sin(\gamma_n) \cos(\gamma_m - \gamma_n) \cos(m\phi) \cos(n\phi) \right|^2. \quad (1.6)$$

The phase angles, γ_m , are defined as,

$$\left. \begin{aligned} \gamma_0 &= ka - \frac{\pi}{4} \\ \gamma_m &= ka - \frac{1}{2} \pi \left(m + \frac{1}{2} \right) \end{aligned} \right\} \text{for } ka < m + \frac{1}{2}, \quad (1.7)$$

$$\left. \begin{aligned} \gamma_0 &= \pi \left(\frac{ka}{2} \right)^2 \\ \gamma_m &= -\frac{\pi m}{(m!)^2} \left(\frac{ka}{2} \right)^{2m} \end{aligned} \right\} \text{for } ka > m + \frac{1}{2}. \quad (1.8)$$

Thus it is possible to calculate the phase and intensity of a wave scattered from an obstacle such as a cylinder. For complex and irregularly shaped objects such as those found in workrooms, the task of computing the scattered waves for even one fitting becomes very difficult. If we account for the fact that there are (more often than not) many such complex shaped fittings in the room, the possibility of calculating the exact sound field becomes nearly impossible. It is of interest then, to find methods of calculating the sound field at low-frequencies which require less precision, yet are sufficient for determining effective methods of control.

1.3 General Room Acoustics and Boundary Conditions

It is possible to calculate the low-frequency response of a room using a wave theory approach. This method is solvable for simple enclosures of rectangular parallelepiped shape and uniform boundary conditions. Because the method only accounts for the dimensions and boundary types of the room for determining the standing waves in the room, it cannot be used to model a fitted room.

The general wave equation is given by,

$$\nabla^2 p - \frac{1}{c_o^2} \frac{\partial^2 p}{\partial t^2} = 0 \quad (1.9)$$

$$\text{with } \nabla^2 p = \frac{\partial^2 p}{\partial x^2} + \frac{\partial^2 p}{\partial y^2} + \frac{\partial^2 p}{\partial z^2},$$

where p is the sound pressure, c_o is the speed of sound waves in the medium, and t is time. This equation is the foundation of all acoustical phenomena, and governs the propagation of sound waves. More specifically, the equation that is most suited to the application of active noise control, which is the static or steady-state room sound field that we want to control, is the Helmholtz equation. This equation is the time invariant wave equation, and can be derived by separating the time and space portions of the wave equation, giving,

$$\nabla^2 p + k^2 p = 0 \quad (1.10)$$

where $k = \omega/c_o$ is the wavenumber, $\omega=2\pi f$ is the angular frequency of a harmonic fluctuation, and c_o is the speed of sound in air. For the analysis to hold in rooms, two assumptions must be made: that there are harmonic waves propagating and that the room surfaces are locally reacting [9]. A wave that is not harmonic is one that is not periodic, such as a hissing sound, and does not follow the harmonic time law ($p \propto e^{i\omega t}$). With the output of the noise sources in a workroom being tonal, the Helmholtz equation holds in this case (i.e., the wave approach is a single-frequency model). A locally reacting surface is one where the reflection of a wave from the surface is not dependent on the angle of incidence of the wave. The acoustical properties of the wall may be characterized by its coordinates and frequency, but not on the angle of incidence.

For an ideal or simplified room, the walls, ceiling and floor are considered to be completely rigid, such that the particle velocity at the wall is zero, and there is a resulting pressure maximum at the surface. The gradient of the pressure is also zero;

$$\frac{dp_x}{dx} = 0 \text{ for } x = 0 \text{ and } x = L_x, \quad (1.11)$$

for the x -direction in the enclosure with a wall at $x = 0$, and a wall at $x = L_x$, and similarly in the other dimensions. From the boundary conditions, and using the general solution for second order differential equations to solve the Helmholtz equation, the solution can be derived as,

$$p_n(x, y, z) = C \cos(k_x x) \cos(k_y y) \cos(k_z z), \quad (1.12)$$

where C is an arbitrary constant governing the magnitude, and in three dimensions, $k^2 = k_x^2 + k_y^2 + k_z^2$. From the definition above and using the boundary conditions, k can be related to the dimensions of the enclosure;

$$k_n^2 = \frac{\omega_n^2}{c_o^2} = \left[\frac{n_x \pi}{L_x} \right]^2 + \left[\frac{n_y \pi}{L_y} \right]^2 + \left[\frac{n_z \pi}{L_z} \right]^2, \quad (1.13)$$

where $n = (n_x, n_y, n_z)$ are the integer node numbers which indicate the numbers of nodal planes perpendicular to the x -, y - and z -axes. The k values represent the eigenvalues for the wave equation, with eigenfrequencies given by,

$$f_n = \frac{c}{2\pi} k_n. \quad (1.14)$$

Thus, for a given nodal number, it is possible to find the corresponding modal response in a room, and also its eigenfrequency.

At higher frequencies, the solution to the wave equation becomes very difficult to calculate because the number of eigenfrequencies grows exponentially with increasing frequency, and the computing time grows accordingly. Fortunately, at higher frequencies, the modal effects of the waves become less apparent because of their shorter wavelengths, and if a uniform distribution of sound energy is formed, a diffuse-field is produced. The theory of diffuse fields is based on a ray model of a room, whereby the rays of sound energy are partly reflected and partly absorbed by the boundaries of the room. After a large number of reflections of the rays, the sound in the room is assumed to have become diffuse, with the energy density in the room the same throughout the space and in all directions. Diffuse-field theory can be used to calculate some of the characteristics of rooms, such as RT and absorption.

One of the most important boundary characteristics of a room is its absorption. The absorption in a room will decrease the amount of energy reflecting from the boundaries, and play a role in the strength of the different modes in a room. If the total average absorption of the boundaries in the room is known, it is possible to calculate the RT in the room. Using diffuse-field theory and the Sabine RT formula, the following equation can be used,

$$RT = \frac{0.161V}{S\bar{a} + 4mV}, \quad (1.15)$$

where V is the volume of the room, S is the surface area of the room, m is the air absorption and \bar{a} is the area averaged room-surface absorption. Conversely, if we can measure the RT in the room, it is possible to calculate the absorption in the room, solving for \bar{a} in Eq. 1.7.

The absorption coefficient of a wall is a real valued number representing the fraction of the incident energy that is lost during reflection. The reflection of a plane wave by a wall, however, affects the phase as well as the amplitude. The changes to a wave that take place upon reflection can be represented by a complex reflection coefficient, R , related to the absorption coefficient by the following equation,

$$a = 1 - |R|. \quad (1.16)$$

The reflection coefficient is related to the physical properties of the wave medium and the physical properties of the wall through the complex impedance, Z , of the wall

$$R = \frac{Z \cos \theta - \rho_o c}{Z \cos \theta + \rho_o c}, \quad (1.17)$$

where ρ_o is the density of the air. The reflection coefficient and wall impedance are dependent on the angle of incidence of the wave on the wall, accounted for by the $\cos \theta$ term, where θ is the angle with respect to the surface normal. The wall impedance is

defined as the quotient of the pressure, p , and the particle velocity normal to the wall, v_n , at the wall surface,

$$Z = \left(\frac{p}{v_n} \right)_{\text{surface}} . \quad (1.18)$$

The modal model, described in Chapter 4.2, uses the Helmholtz equation and its eigenvalue solutions to solve for the modal response of the room. Non-rigid walls perturb the modal response and are accounted for by using a damping factor calculated from the surface impedance, Z . This damping factor is a complex value and can account for non-rigid walls that affect the phase but not necessarily the amplitude of the reflected wave.

1.4 Control Methods

There are generally two control methods used to reduce noise levels (besides silencing the noise-generating device itself) - passive and active noise control.

Passive control relies on the use of materials to absorb or block the noise being radiated. The materials used to absorb sound energy usually consist of a layer of porous, flexible material that absorbs the energy through dissipation within the material. Absorption performance depends on porosity, density, and the thickness of the material in relation to the wavelength of the sound. Barriers may be installed between sources and receivers to block noise, but they also have the effect of increasing the energy on the

source side of the barrier, since the barrier may also act as a reflector of the energy output by the source. It is also possible for sound to diffract around the barrier, so the barrier must be constructed with this in mind.

Another method of passively controlling noise is through the use of enclosures to enclose the noise-generating device. Depending on the size of the enclosure needed, and the type of access to the device required, an enclosure may not be feasible, or at least may be difficult and costly to implement. Performance of the enclosure is also low at low-frequencies due to the increased transmission through the enclosure, and due to modal effects within the enclosure. Enclosures suffer from a similar effect as a barrier, in the sense that they enclose the source and reflect the energy back towards the source. This causes the inside of the enclosure to have a much higher sound pressure level which must be blocked, but lining the enclosure with absorptive material helps to mitigate the problem.

Because of the long wavelengths of low-frequency sounds, they are difficult to control using passive methods. Barriers must be large enough to prevent diffraction effects; for absorption to be effective, it must be very thick. Enclosures also must be stiff to resist flexing and thus transmitting the energy outside.

Active noise control relies on the use of transducers to output a signal of equal magnitude and opposite phase to the noise signal, which effectively cancels the overall noise output through the principle of wave superposition and destructive interference.

The transducers are controlled by either a feedforward or feedback controller which relies on the use of a sensor placed at the noise source to detect the noise output. In the case of a feedback controller, error microphones are also used to further optimize the output of the transducers, to more effectively cancel the noise in the area around the microphone.

The concept of active control has been around for many years [10], but only recently has the technology been available to implement this type of control. This method, however, is difficult to implement for high-frequency control because of the very short wavelengths of high frequency sounds. Also, with increasing frequency of the sounds, the overall sound field becomes more diffuse, and the source directivity changes, making it much more difficult to control. Active noise-canceling headphones have been used for many years to decrease the ear's exposure to low-frequency noise, but this method also has its problems. The use of headphones only limits the exposure at the ear, and does not prevent exposure to the rest of the body. Also, headphones limit the ability to detect high-frequency sounds, and add another inconvenience to a worker who often must already wear and use many other protective devices. Decreasing the overall level of low-frequency noise would make the workplace much safer and more welcoming for workers and other people in the workroom.

In the spring of 2002, Li started work at UBC on a project involving the active control of noise in industrial workrooms. This followed from work performed by Guo [11], who had previously developed a general image-source prediction model to predict

the sound fields of rooms, and allowed the input of control sources and error microphones to predict the effect of an active noise control system on the room sound field. Li [12, 13] extended the prediction model by proposing a new ‘locally-global’ control strategy, and by using genetic algorithms to optimize the positions of the control sources and microphones to control a localized area (without increasing the sound pressure level elsewhere in the room). Parallel to this work is the study detailed in this thesis, into the characteristics of low-frequency sound propagation in industrial workrooms. More specifically, the work presented here investigated the effects of the fittings and the room boundary conditions on the sound field at low frequencies and methods for its prediction. This will aid in understanding and creating a more accurate prediction model for use in the active control of noise, and its optimization for use in fitted workrooms.

1.5 Research Objectives

With the review of the established literature and theory on fittings and boundaries in rooms completed, the specific research objectives were outlined. The overall objective was the investigation of the characteristics of low-frequency noise in rooms, the factors that affect them, and how to predict them. This objective was achieved as follows:

- Measuring and analyzing a real-world workroom with and without fittings to determine the effects of fittings on the workroom low-frequency sound field (in particular, on reverberation times and steady state noise levels);
- Measuring and analyzing a scale-model workroom with and without fittings to further understand their effects;
- Integrating wave and boundary effects at low-frequencies in room prediction models to understand their effects on the enclosed sound field. This involved both an image-phase, as well as a modal, prediction model;
- Comparing prediction to measurements in both the real-world workroom and the scale model room when empty to validate the prediction models;
- Modeling fitting effects in a free-field environment (i.e. without room effects) at low-frequencies and comparing them to measurements in an anechoic chamber with fittings.

This work effectively extends existing work by Hodgson [7, 8] characterizing and modeling mid- and high-frequency sound propagation in workrooms with fittings, to lower frequencies.

Chapter 2

Workroom Measurements

2.1 Real Workroom

In order to get a better understanding of the characteristics of low-frequency sound propagation, the steady-state sound field in large workrooms and the factors – for example, fittings – that affect them, measurements were taken in a full-scale machine shop while empty, and then with fittings in the room. Measurements were made of reverberation time and steady-state sound pressure level. A low-frequency sound source was designed and built, and used to generate pure tones and octave-band-filtered noise.

2.1.1 Details of the Machine Shop

The machine-shop inner dimensions were 73.8 m x 31.9 m x 10.1 m high. The floor consisted of unpainted concrete and the ceiling was constructed of corrugated metal panels, covered in a layer of spray-on acoustical absorbent. The walls were a mix of corrugated metal panels, drywall, and painted concrete. The West wall was made entirely of drywall. The East wall consisted of about 20 % painted concrete, and 80 % single-

layered corrugated metal paneling. The North wall was made up of about 50 % painted concrete forming the bottom half of the wall, with the top half and some large loading doors made of corrugated panels and absorbent covered paneling. The South wall consisted of 50 % painted concrete and 50 % corrugated paneling. Columns ran along the center of the room, spaced 5m apart. Fig. 2.1 shows the plan layout of the machine shop, showing the source position and the measurement lines (dashed line).

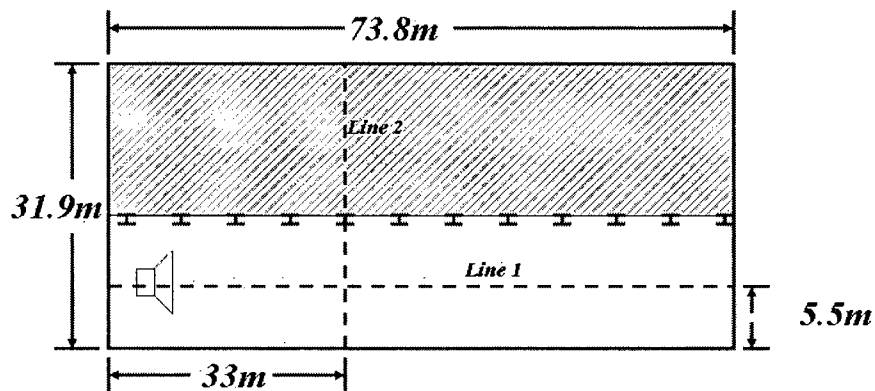


Figure 2.1 Dimensions and layout of the real workroom.

In the fitted configuration, the workroom was divided in half lengthwise into two sections. On the side containing the source, machines such as lathes, drill presses and mills were located along the length of the building on either side of Line 1. These machines averaged about 1 – 1.5 m in height and about 2 m in length. 2.4 m x 2.4 m x 12mm-thick particleboard partitions, were located between many of the machines as barriers between stations. The other half of the shop was used for temporary storage,

painting, welding, and fabrication of large pieces of metal. During the fitted-room testing, there were two very large obstacles on the storage side of the workshop, one being a large metal container about 6 m x 3 m x 3 m high.

2.1.2 Equipment Setup

A low-frequency loudspeaker source was constructed to generate the low-frequency sounds needed to test the large workroom. It consisted of two 380-mm low-frequency speaker drivers mounted on opposite ends of a sealed 460-mm cubic wooden box. Both speakers were driven in phase. The output level of the source was chosen to ensure adequate signal-to-noise, and was kept constant for the two cases – empty and fitted. The source was placed on the floor at one end of Line 1, 0.65 m from the wall. Four source signals were considered in the test; a 63 Hz pure-tone, and 31.5 Hz, 63 Hz, and 125 Hz octave-band-filtered white noise. Note that the frequencies of 31.5, 63 and 125 Hz correspond to wavelengths in air of 10.8 m, 5.4 m and 2.7 m, respectively, which are greater than or much greater than the fitting dimensions. The equipment setup follows the flow diagram in Fig 2.2. The low-frequency source was characterized in the anechoic chamber – these measurements are discussed in Appendix A.

The steady-state sound field was sampled along the width and length of the room, chosen along pathways which would not be later blocked by the fittings. For the pure-

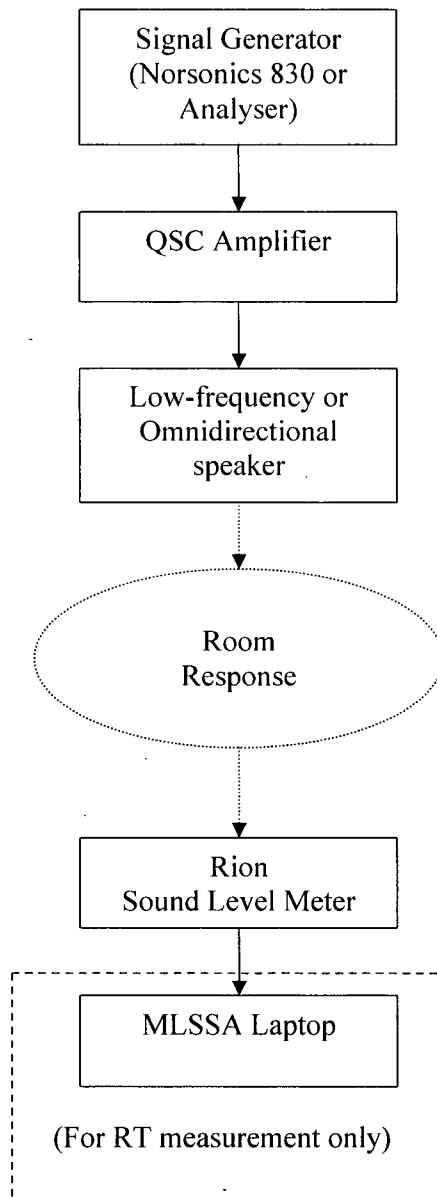


Figure 2.2 Flow diagram of the equipment setup in the real workroom measurements.

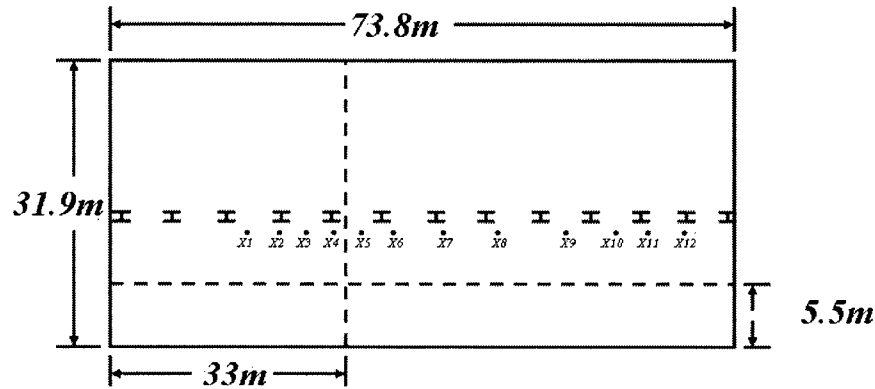


Figure 2.3 The X-positions in the real workroom

tone steady-state measurements, the sound pressure level was measured at 1 m intervals along Lines 1 and 2. For the octave-band tests, measurements were taken at 1m intervals from 1 m to 10 m, and every 10 m thereafter. Measurements were also taken at positions between locations at which the workshop machines would be placed; in positions where people would be standing to operate them. These are marked as the X-positions on the floor plan Fig 2.3. The receiver microphone was located at a height of 1.2 m above the floor for all measurements. Some pictures of the fittings around the X-positions are shown in Appendix B.

The RT was also measured to characterize the room, and the corresponding average workshop surface-absorption coefficients calculated from the values obtained. For the two lowest octave bands, the low-frequency source was used to measure the RT using the Norsonics analyzer. For the higher frequencies, an omnidirectional speaker was

used along with the MLSSA system to measure the RT. With both the low-frequency loudspeaker and the omnidirectional speaker, six measurements were taken with the microphone and speaker placed in random locations around the central part of the workroom, and the results averaged between the six measurements to determine the RT.

2.1.3 Measurement Results in the Workroom

The RT was first measured to characterize the room, and the corresponding absorption coefficients calculated from the values obtained. Table 2.1 shows the measured RT in the room, empty and with fittings. The surface absorption coefficient was calculated from the measured RT using the Sabine reverberation equation, Eq. 1.15. The absorption coefficients are listed in Table 2.2.

The RT in the empty room is almost 5 s at low frequency, and decreases with increasing frequency, with the 8 kHz octave band level being very short, at 0.52 s. In the fitted workshop, the RT decreases from over 4 s to 0.68 s. The RTs decreased with the addition of the fittings at all frequencies except at 125Hz and 8kHz. This appears in the absorption coefficient results as a decrease in the absorption coefficient at those particular frequencies. The RT decreases with increasing frequency, with the 8 kHz octave band level being very short, at 0.52 s. The RT generally decreases with the introduction of the fittings, as was found in previous work [7]. In the empty workroom, the RT in the room

Table 2.1. Measured RT (seconds) of the real workroom, with the low-frequency source and the omnidirectional source.

| Band [Hz] | Low Freq. Source | | Omnidirectional Source | | | | | | |
|-----------|------------------|------|------------------------|------|------|------|------|------|------|
| | 31.5 | 63 | 125 | 250 | 500 | 1000 | 2000 | 4000 | 8000 |
| Empty | 4.88 | 3.76 | 1.61 | 2.44 | 2.31 | 2.00 | 1.93 | 1.32 | 0.52 |
| Fitted | 4.22 | 2.52 | 2.78 | 1.93 | 1.29 | 1.42 | 1.26 | 1.01 | 0.68 |

Table 2.2. Calculated absorption coefficients of the real workroom, with the low-frequency source and the omnidirectional source.

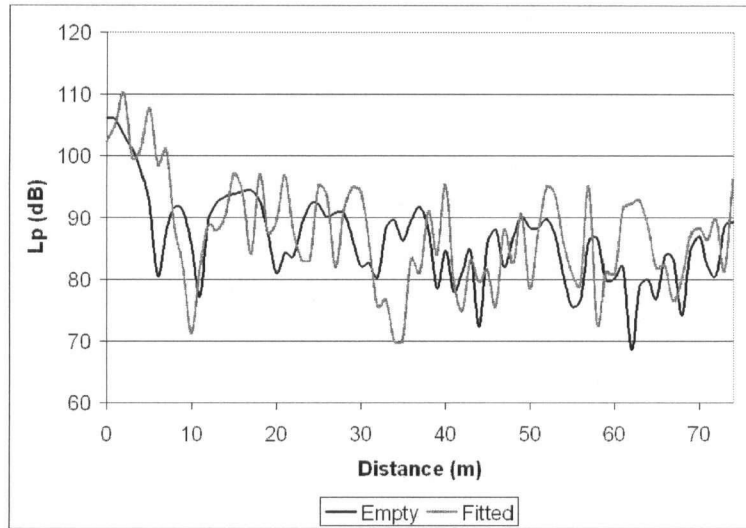
| Band [Hz] | Low Freq. Source | | Omnidirectional Source | | | | | | |
|-----------|------------------|------|------------------------|------|------|------|------|------|------|
| | 31.5 | 63 | 125 | 250 | 500 | 1000 | 2000 | 4000 | 8000 |
| Empty | 0.12 | 0.15 | 0.35 | 0.23 | 0.25 | 0.29 | 0.30 | 0.43 | 1.10 |
| Fitted | 0.14 | 0.23 | 0.21 | 0.30 | 0.44 | 0.40 | 0.45 | 0.54 | 0.84 |

was measured to be over 2 s in many of the octave bands. A high RT indicates that the temporal decay is slow, and sound energy remains in the room, effectively adding to the noise source's output in the room. Conversely, reducing the RT would decrease the overall level of the noise.

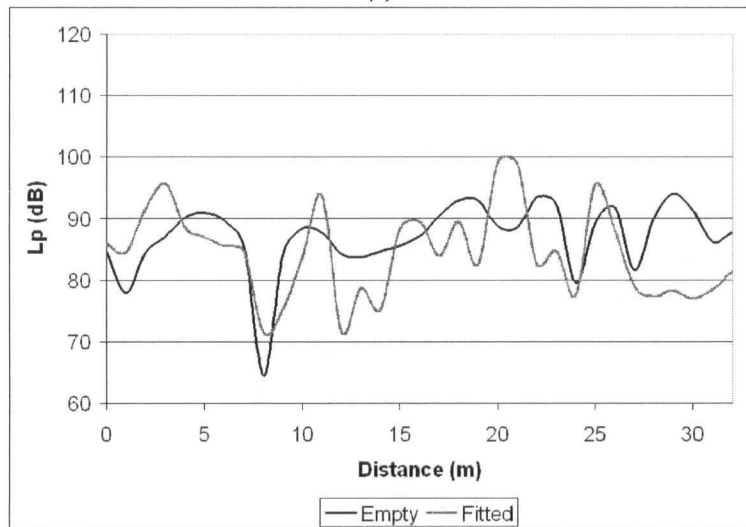
2.1.4 Low-Frequency Source Tests

Figure 2.4 shows the measured sound pressure level along Lines 1 and 2 for a 63 Hz pure tone signal output by the low-frequency source under the empty and fitted conditions. In the empty room, the modal pattern varies much less than with fittings – especially close to the source. In the fitted room levels vary strongly – by to 20 dB – due to modal effects. The differences between the empty and fitted case are quite dramatic. The addition of the fittings changes the sound pressure level (relative to the empty case)

in some instances by more than 20 dB. Close to the source, the fitted room causes a higher sound pressure level near the source, while far from the source the average sound pressure level is similar in both cases. Along the width of the room, the average sound pressure level is slightly lower and the sound pressure level varies more in the fitted case.



(a)



(b)

Figure 2.4. 63Hz pure tone measured at 1m intervals along Line 1 (a) and Line 2 (b) in the workshop.

The propagation of octave-band-filtered noise from the source at low frequencies was measured in the room and the results are shown in Figure 2.5. When the room was empty, levels generally decreased with distance with only small variations – that is, the measurement showed only slight modal response. With fittings, the measurement results showed a higher modal response with highly varying sound pressure level along the distance of the room. The number of peaks and dips in the sound pressure level did not change appreciably with the frequency. These results are partially explained by the fact that at lower frequency and longer wavelengths, the number of modes decreases and fewer instances of wave cancellation or addition occur.

Figures 2.6 and 2.7 show the sound pressure level measured at the X-positions in the room when empty and fitted for a 63 Hz pure tone and 31.5, 63, and 125 Hz octave band noise. In the empty room, the 63 Hz pure tone measurement shows quite a large variation in the sound pressure level at the X-positions. This is consistent with the data measured above, and the high modal response of the room with a pure tone excitation. With the octave band noise, the levels did not vary much and stayed quite even throughout the positions. In the fitted workroom, however, the sound pressure levels varied in some cases over 10dB from the values measured in the empty workroom. The fittings affect the various octave bands unpredictably; the measured sound pressure level does not follow the same trend for each of the frequencies.

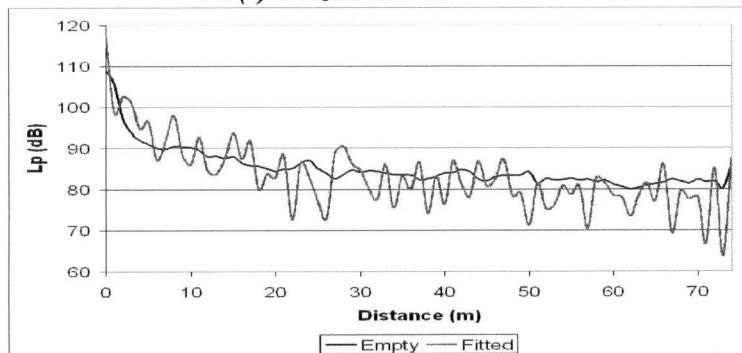
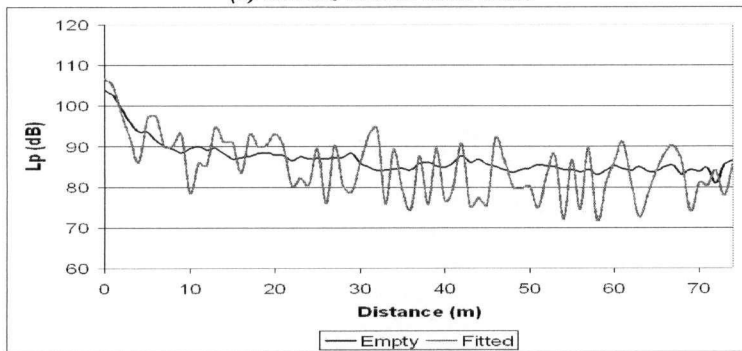
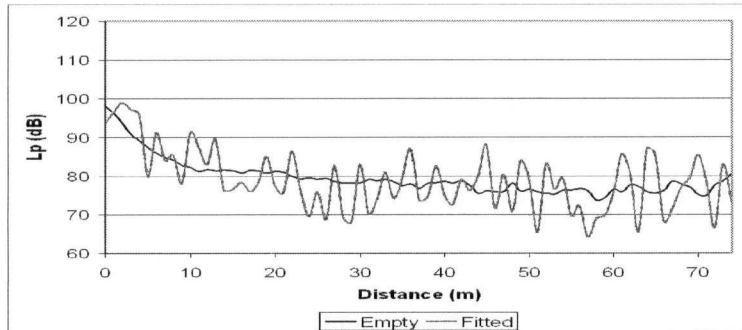


Figure 2.5. 31.5, 63 and 125 Hz octave band noise measured at 1 m intervals along Line 1 in the workshop when empty and fitted.

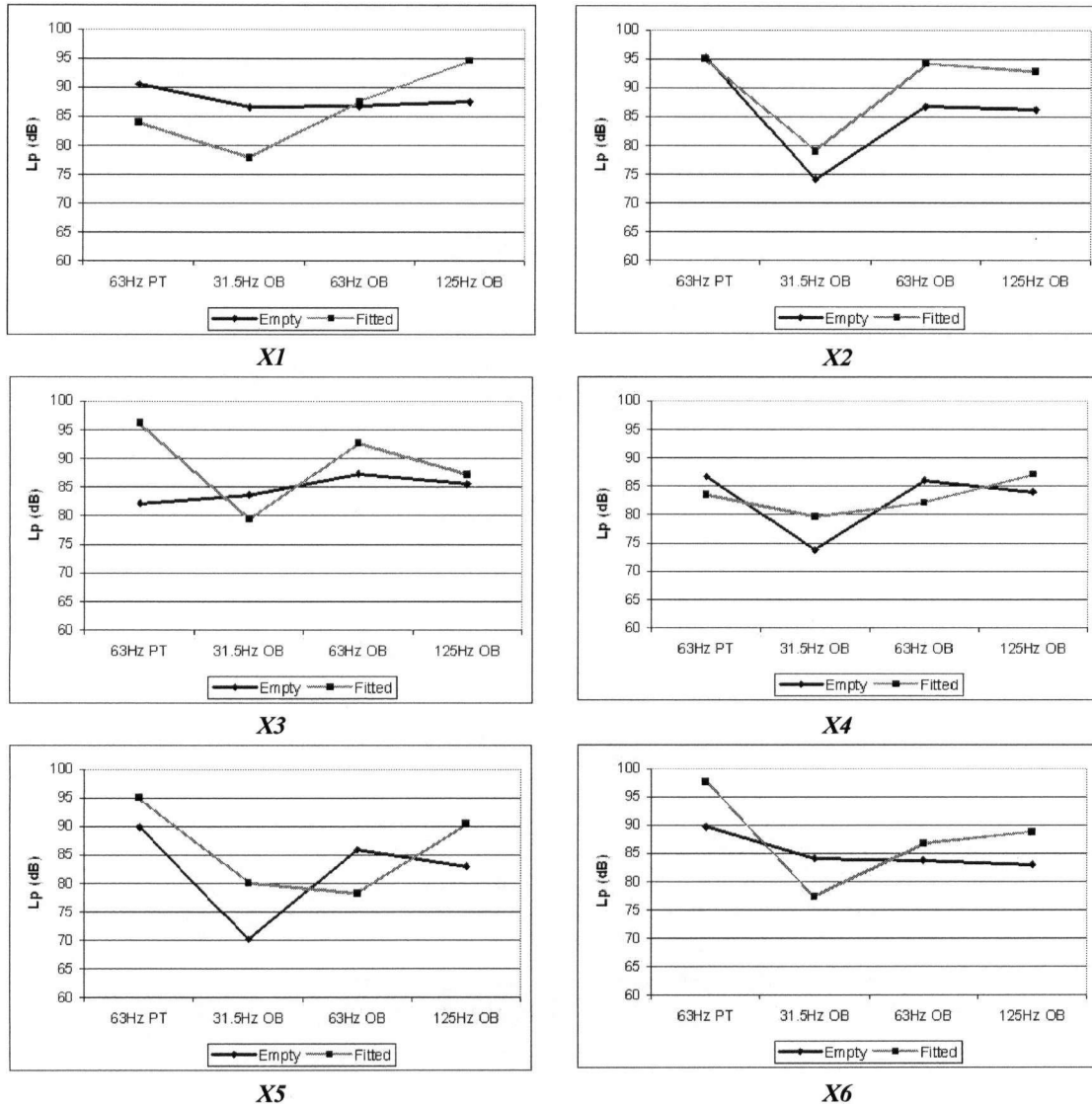
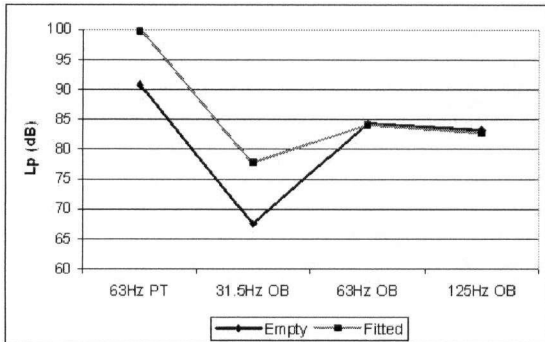
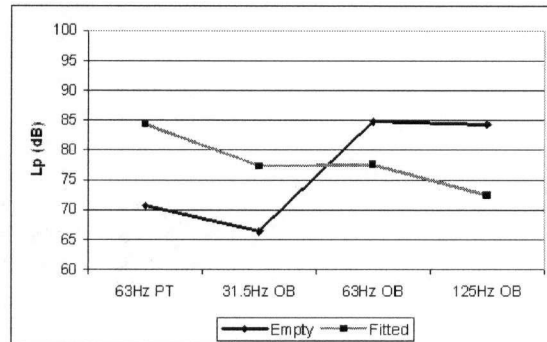


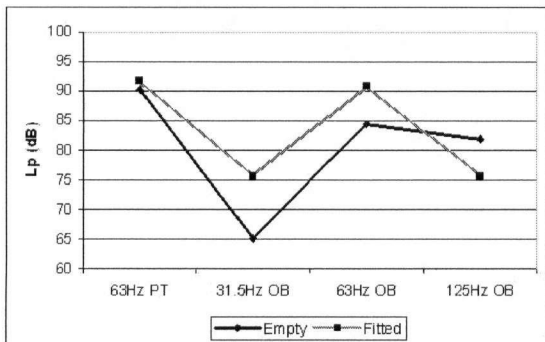
Figure. 2.6. Measured sound pressure levels in the empty and fitted conditions at X-positions 1 to 6 in the workroom.



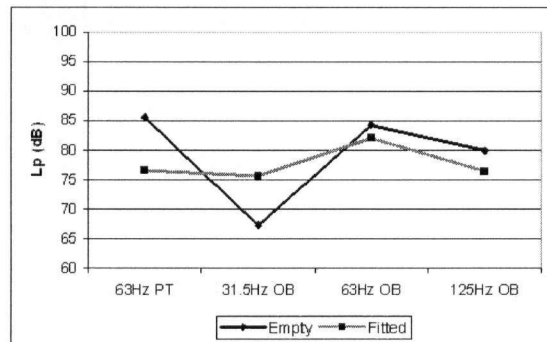
X7



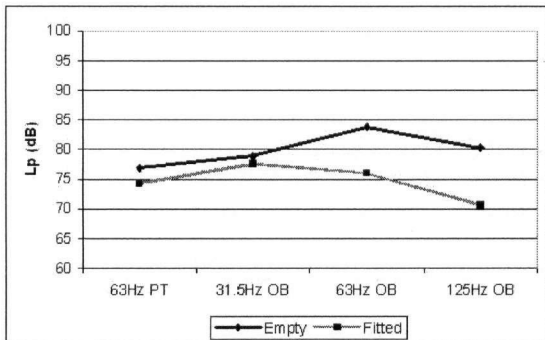
X8



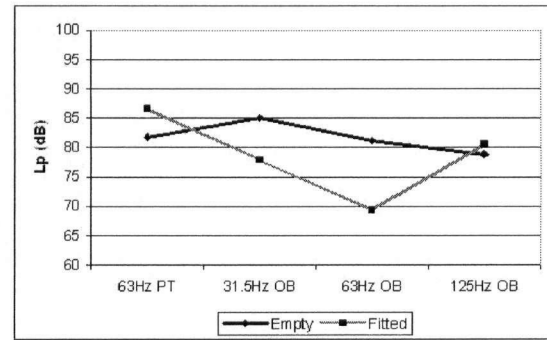
X9



X10



X11



X12

Figure 2.7. Measured sound pressure levels in the empty and fitted conditions at X-positions 7 to 12 in the workroom.

2.1.5 Omnidirectional Source Tests

Figures 2.8 and 2.9 show results of the measurement of the sound pressure level along Line 1 of the workroom, with white noise output from the omnidirectional loudspeaker. The introduction of fittings was found to alter the sound pressure level in an unexpected manner compared to measurements in fitted workshops by Hodgson [7], which did not show any indication of modal effects at the high frequencies. In the empty case, the sound pressure level decreases smoothly as expected. At higher frequencies it was expected that the sound pressure level near the source would be higher due to the energy reflection from the fittings back towards the source; farther from the source, the sound pressure level would be lower than without fittings. This also follows from findings by Hodgson [7] which show higher sound pressure levels near the source, and lower sound pressures far from the source, in a room with fittings. Such behaviour was not found in the present measurements.

Figure 2.10 shows the measured sound pressure level at the x-positions in the workroom, with white noise output from the omnidirectional source. In the case of the empty room, the sound pressure levels decreased monotonically with increasing distance from the source. In the fitted room, the sound pressure level varies highly with position. The measured sound pressure level at each of the frequencies does not seem to follow a similar trend.

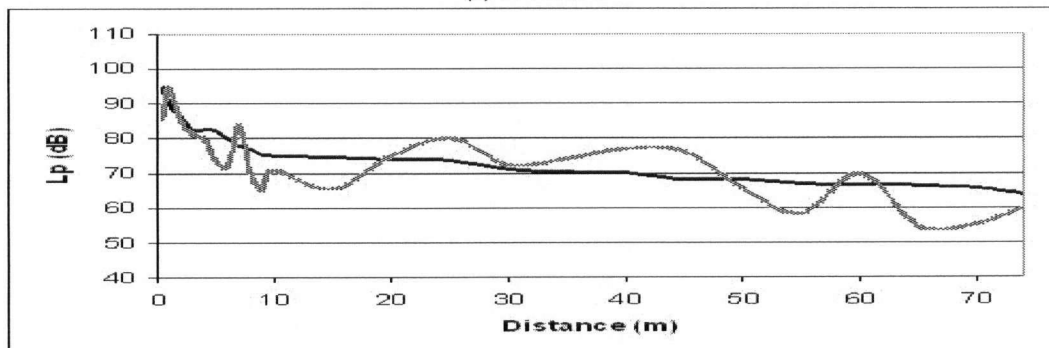
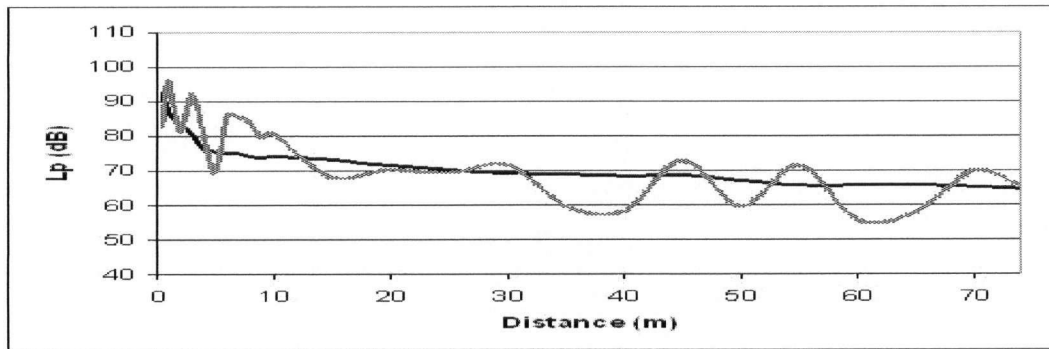
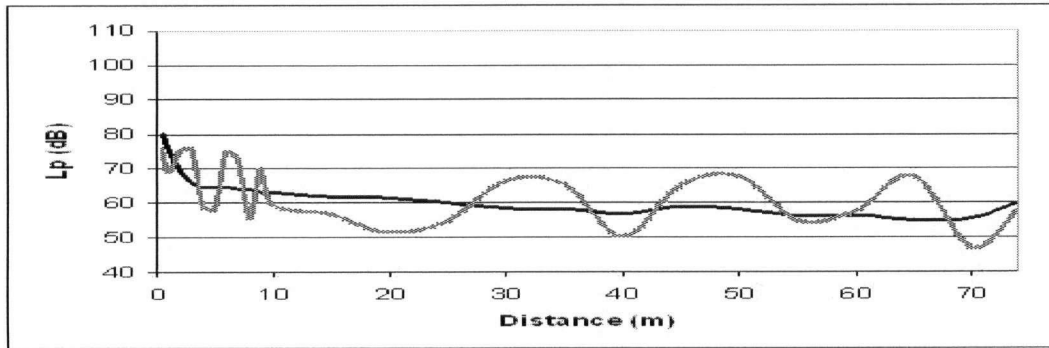
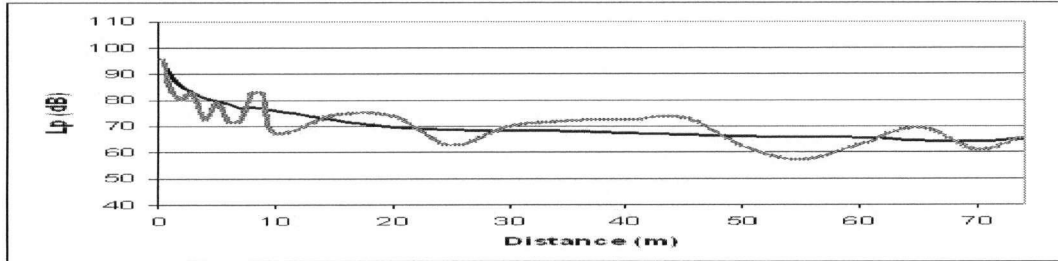
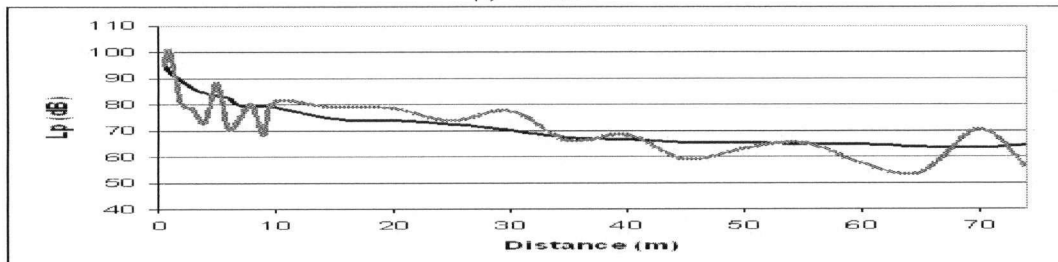


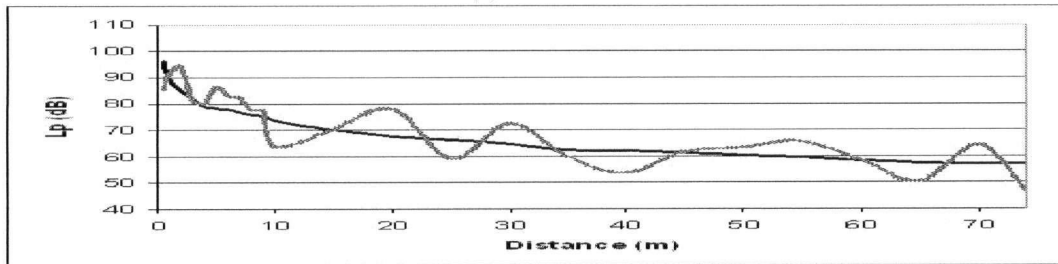
Figure 2.8. Octave band sound pressure level measured along Line 1 of white noise output by omnidirectional source.



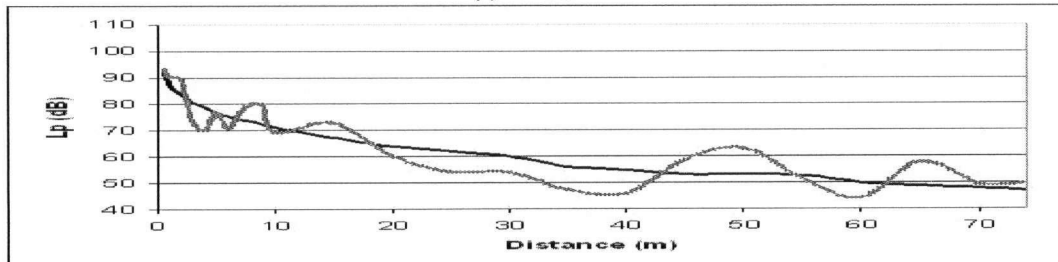
(a) 1k HzOB



(b) 2k HzOB

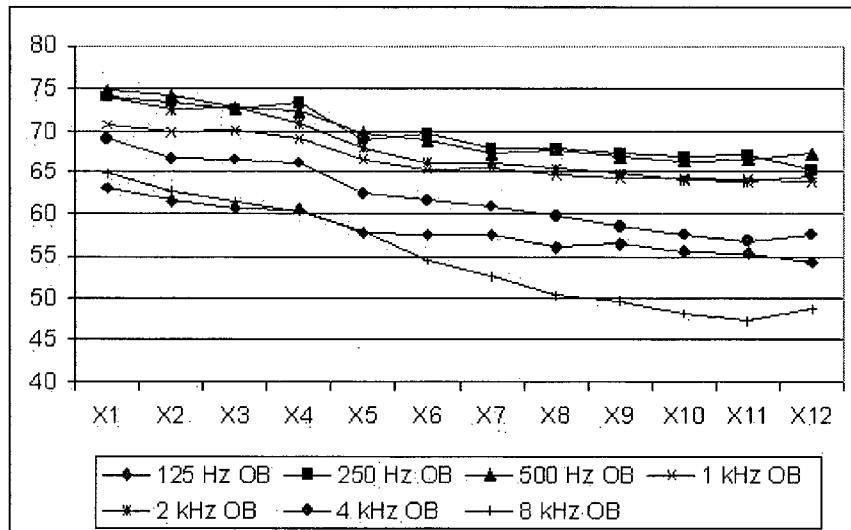


(c) 4k HzOB

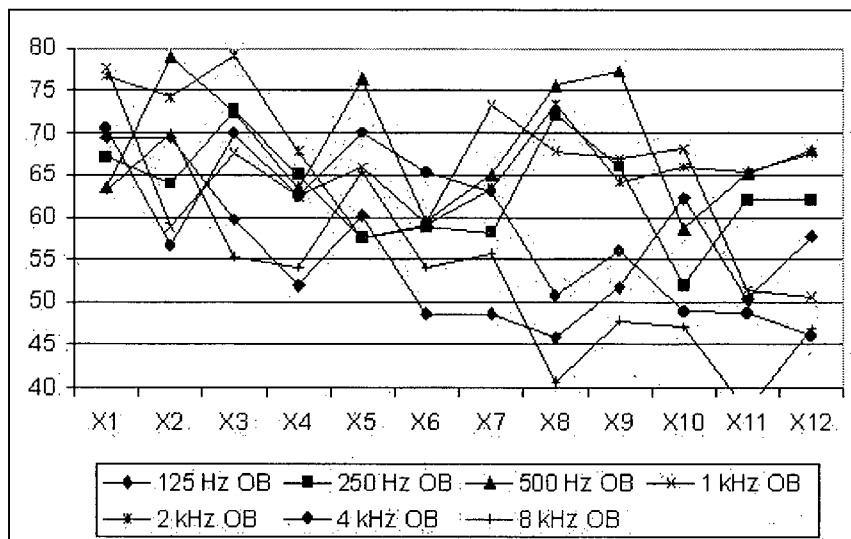


(d) 8k HzOB

Figure 2.9. Octave band sound pressure level measured along Line 1 of white noise output by omnidirectional source.



(a) Empty



(b) Fitted

Figure 2.10. Measured sound pressure level at the X-positions in the workroom. The source output white noise and sound level measurements were recorded at 1/3 octave-band intervals.

2.1.6 Summary

In the empty workroom, the RT was found to be very high, with very little absorption at low frequencies. The introduction of fittings decreased the RT in the room. With low-frequency pure-tone noise, the modal pattern varied much more with the introduction of fittings than in the empty room. This is likely due to the increased number of reflection surfaces from the fittings. With octave-band noise output from the low-frequency source, no modal patterns were measured in the empty workroom, however, with fittings, a highly varying modal pattern was measured. Also, the number of peaks and dips did not seem to increase with increasing frequency. At high frequencies, with white noise output from the omnidirectional speaker, it was found that the decay with fittings varied much more than as measured in previous work. Measurement results at the X-positions showed little evidence of a pattern.

2.2 Scale Model Measurements

2.2.1 Scale Modeling Theory

In order to get a better understanding of the propagation of low-frequency sound waves in a workshop setting, scale model tests were performed. This allowed for measurements in a controlled setting, where we could control the fittings and fitting density, room dimensions, surface properties, and have the measurements easily

repeatable. The principles and considerations needed for acoustic scale modeling have been well researched and documented [14], especially in factory and other industrial settings [6], and scale model testing has proven very useful in being able to model and help in the understanding of acoustical problems and the design of factory buildings.

With scale modeling, several things need to be considered to ensure the accuracy and reliability of the measurements, and its applicability to real-world conditions. The scale factor must be chosen with respect to the frequencies to be modeled and their corresponding wavelengths. Ease of modeling must also be taken into account with respect to the scaling factor, n . At a $1 : n$ scale, the dimensions are scaled by $1/n$ and frequencies are scaled by n . At higher frequencies, air absorption must be taken into account, and this value is scaled by a factor of n^2 . The air absorption may be greatly reduced by decreasing the humidity of the air in the scale model, and the scaling factor will be closer to n . The sound pressure level at the scaled distance is the same as the full-scale value at the full-scale distance, while the RT must be scaled by $1/n$. From this point on, it is useful to present the numbers and values reported in this text for the scale model in their full scale equivalent dimensions and values, with the FS notation after the units, where applicable.

2.2.2 Scale Model Setup

The scale model room was set up at $1/8^{\text{th}}$ scale to model a rectangular workroom with dimensions of 30mFS x 15mFS x 7.5mFS. The floor was unpainted concrete while the walls and roof were constructed from 10mm and 3mm plywood panels, respectively. The walls were varnished on the inner surface. The walls and roof were supported on a metal frame.

A single 100mm full-range loudspeaker was used as a source in all of the scale model tests. Its radiation characteristics were measured and the results presented in Appendix A. It was placed in a 120mm x 120mm x 200mm enclosure, with the speaker set in 80mm from the top face of the enclosure for increased directivity. For these tests, the speaker was positioned facing one corner of the room, in an effort to obtain the maximum excitation of the modal response in the scale model.

To simulate fittings, wooden cubes were used. Two different fitting conditions were tested; small and large fittings. The large fittings were 2 mFS cubes constructed of 6mm plywood. Ten large fitting cubes were evenly distributed around the room in random orientations, leaving an area around the source unobstructed. The small fittings were simply solid blocks of wood with dimensions of 1 mFS x 0.65 mFS x 0.65 mFS. Forty blocks were placed in random orientations, evenly distributed around the room, again leaving an area of about 8 mFS around the source unobstructed. The large fittings

served to increase the total surface area in the room by 160 mFS^2 , and decrease the volume by 80 mFS^3 . The small fittings took up 16.9 mFS^3 of volume in the room, and increased surface area by 85.8 mFS^2 . Note that both types of fittings were small compared to the wavelengths of the low-frequency test sounds.

The air absorption was considered to be very small in the scale model at the frequencies used in the tests, and it was not necessary to reduce the humidity. At 20°C and 50% humidity in the room, the air absorption at 250 HzFS and scaled by n^2 is calculated by ANSI S1.26 to be about 0.3 dB over the distance of the scale model [15]. However, the difference in the sound pressure level caused by the effect of air absorption is within measurement error. This effect is also further reduced at lower frequencies, since air absorption increases with increasing frequency.

To characterize the scale model room, measurements of the RT were performed, and the total surface absorption coefficients of the room were calculated from these values. The RT was measured using the MLSSA system, with the same source as used in all subsequent tests, as well as the same microphone. A standard room measurement setup was used, with the results averaged over six different measurements with the source and microphone at different positions in the room each time. The Sabine reverberation equation was used again to calculate the absorption coefficient from the measured RT values (as in the real workroom measurements).

Sound pressure level measurements were taken along a length of the scale model room. Also, two lines along the width of the room were measured, one close to the source and one far from the source. To ensure that the line measured was not along a nodal line, the lines were carefully chosen and measurements were made along lines with many antinodes in the empty room. This resulted in choosing slightly different lines for

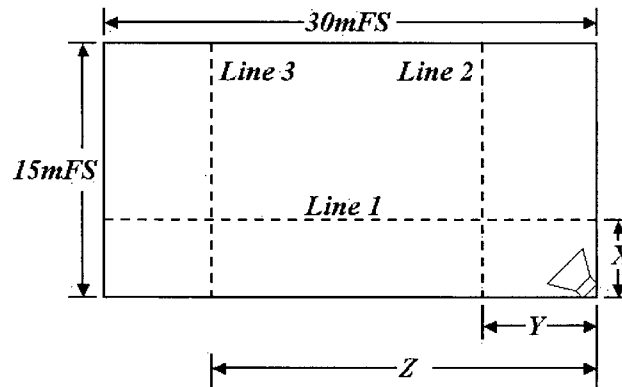


Figure 2.11. Diagram of the measurement lines in the scale model room; distances X, Y and Z are listed in Table 5 below.

Table 2.3. Positions of the measurement lines taken in the scale model room; distances X, Y and Z are as shown on Figure 5 above.

| <i>Frequency (Hz)</i> | <i>X (mFS)</i> | <i>Y (mFS)</i> | <i>Z (mFS)</i> |
|---|----------------|----------------|----------------|
| 31.5 | 4 | 6.4 | 24.4 |
| 63 | 12 | 12 | 21.6 |
| 125 | 6.8 | 6.4 | 23.6 |
| 250 | 6.8 | 6.4 | 21.6 |
| <i>Octave Band noise, all frequencies</i> | 4 | 6.4 | 24.4 |

each of the frequencies measured (see Table 2.3). The receiver microphone was placed at a height of 1.6mFS for all measurements in the scale model.

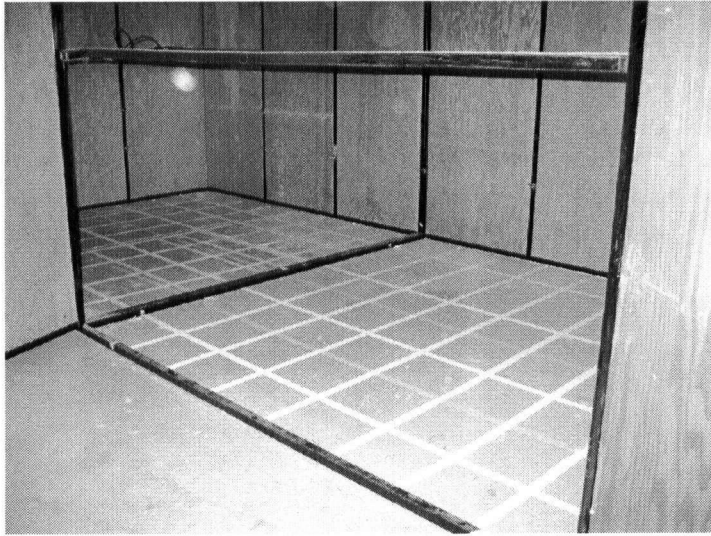


Figure 2.12. The empty scale model room set up at 1/8th scale, 30mFS x 15mFS x 7.5mFS.

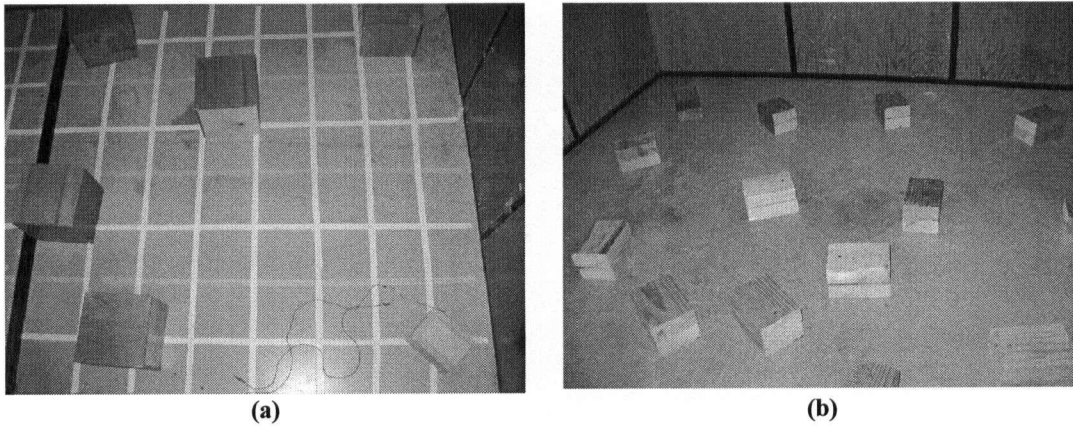


Figure 2.13. The large (a) and small (b) fittings in the scale model room. The source placement can be seen in the photo with the large fittings.

The scale model was tested under pure tone and octave band filtered noise at 31.5, 63, and 125Hz frequencies for each of the empty, small fitted, and large fitted room conditions.

2.2.3 Results

The measured RT values are shown in Tables 2.4 and 2.5. The high RT values are indicative of a room with very little absorption. The RT was highest when the room was empty, while small fittings caused the RT to decrease slightly. With large fittings, the RT at 31.5 and 63HzFS decreased by nearly 3 seconds, while at 125 and 250HzFS, it did not decrease as much. With the large fittings taking up more volume in the room, and having more exposed surface area than the small fittings, the RT is expected to decrease more with the large fittings than the small fittings. This is shown to be the case in the measurement results. The absorption coefficient increased most at the lower frequencies with the addition of the large fittings. The small fittings caused a slight increase of the absorption coefficient in the room.

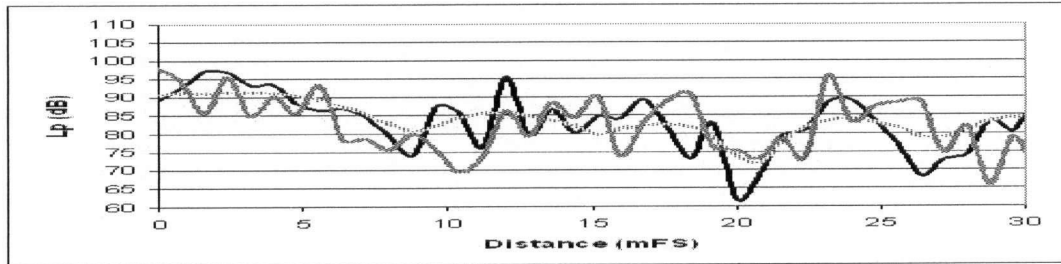
Table 2.4. Reverberation times (sFS) measured in the scale model room when empty and fitted with small and large fittings.

| | 31.5HzFS | 63HzFS | 125HzFS | 250HzFS |
|-----------------------|----------|--------|---------|---------|
| Empty Room | 6.3 | 7.6 | 7.2 | 6.6 |
| Small Fittings | 6.0 | 6.6 | 6.2 | 6.0 |
| Large Fittings | 3.5 | 5.0 | 5.7 | 6.0 |

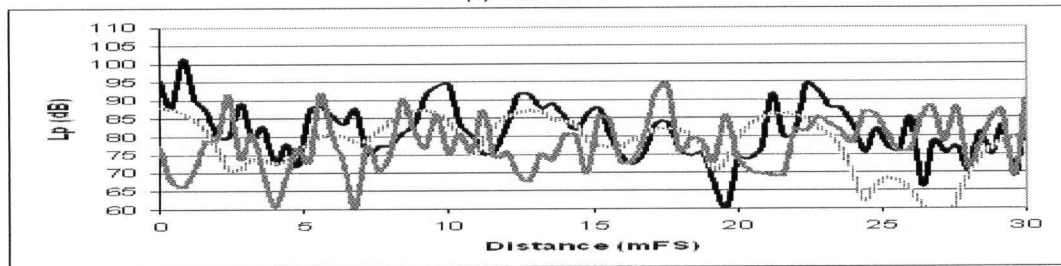
Table 2.5. Absorption coefficients calculated from the reverberation times measured in the scale model room when empty and fitted with small and large fittings.

| | 31.5HzFS | 63HzFS | 125HzFS | 250HzFS |
|-----------------------|-----------------|---------------|----------------|----------------|
| Empty Room | 0.055 | 0.045 | 0.047 | 0.050 |
| Small Fittings | 0.057 | 0.052 | 0.054 | 0.056 |
| Large Fittings | 0.098 | 0.070 | 0.060 | 0.056 |

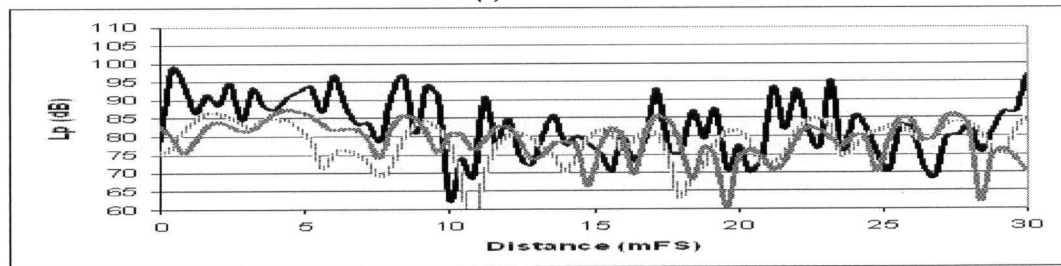
Figure 2.14 shows the result of the measurement of the sound pressure level for the pure tone signal along Line 1 with the source in the corner of the room. Without fittings, there is a high modal response at each of the frequencies measured. The addition of the small fittings tended to smooth out the variations and, as such, the curves had fewer and smaller peaks and dips in the sound pressure level. At the lower frequencies 31.5, 63 and 125Hz, the variation in sound pressure level was much higher than at 250Hz.



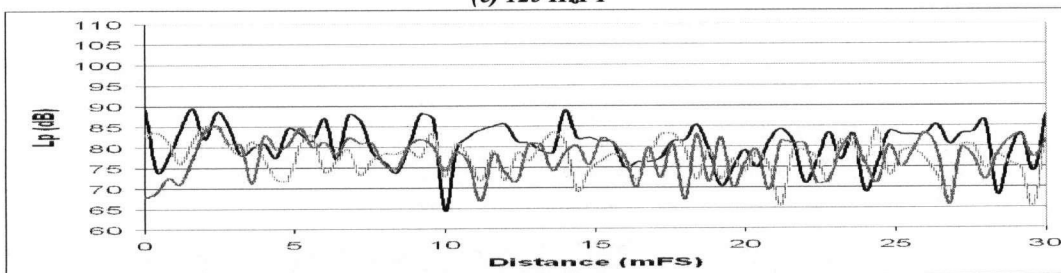
(a) 31.5 HzPT



(b) 63 HzPT

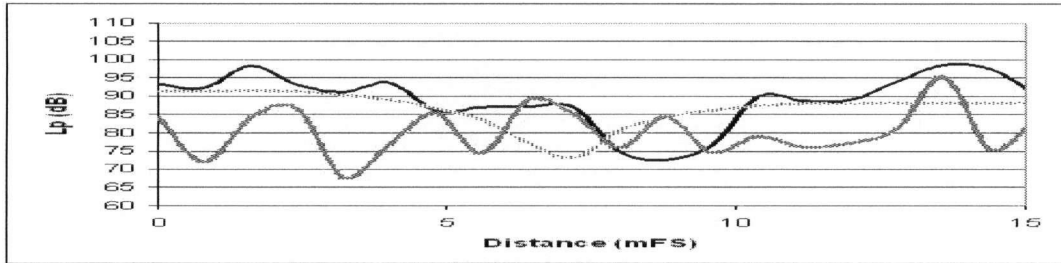


(c) 125 HzPT

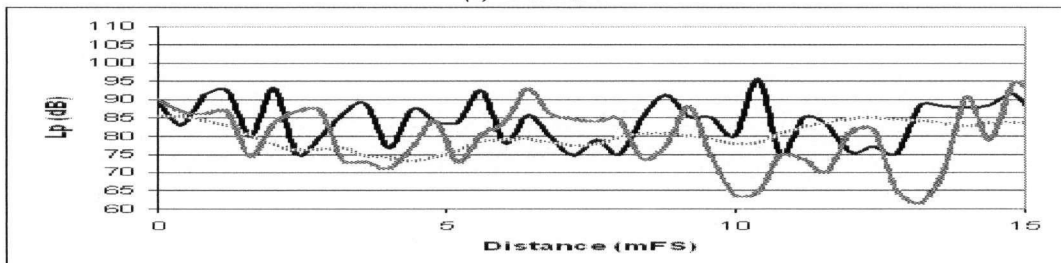


(d) 250 HzPT

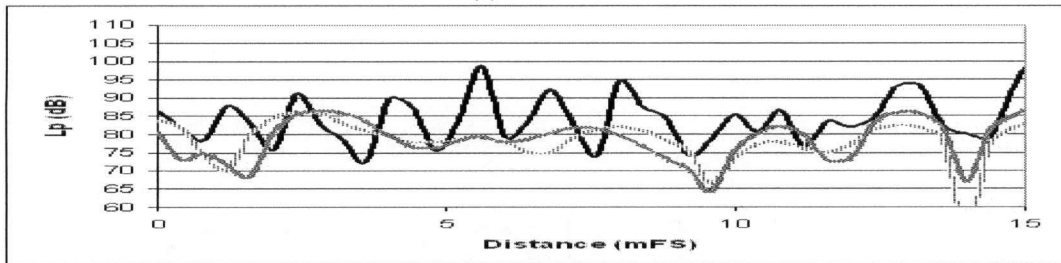
Figure 2.14. Measurements along Line 1 with the source output at 31.5, 63, 125 and 250 Hz pure tone. (Solid Black line – Empty, Dotted line – Small Fittings, Grey line – Large Fittings)



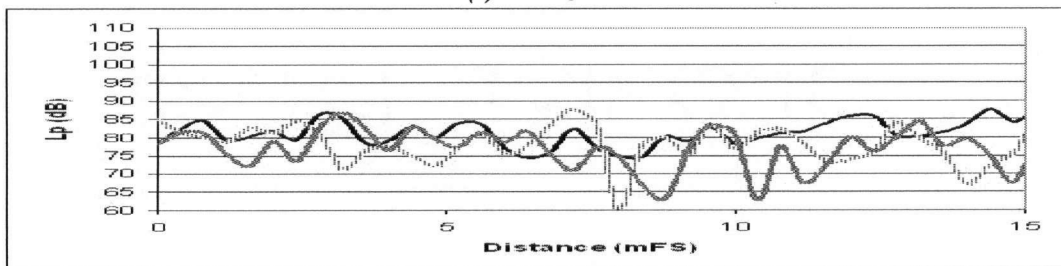
(a) 31.5 HzPT



(b) 63 HzPT

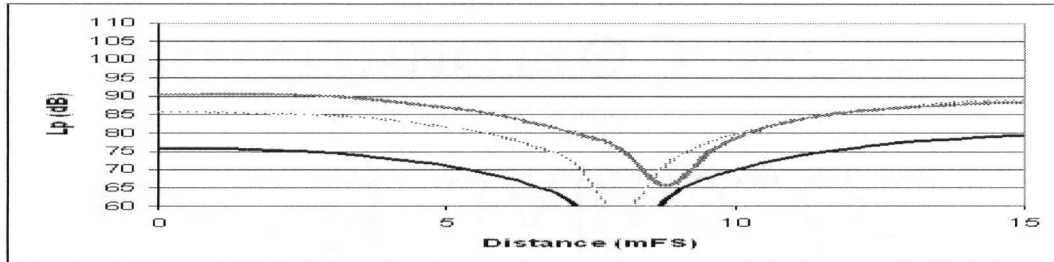


(c) 125 HzPT

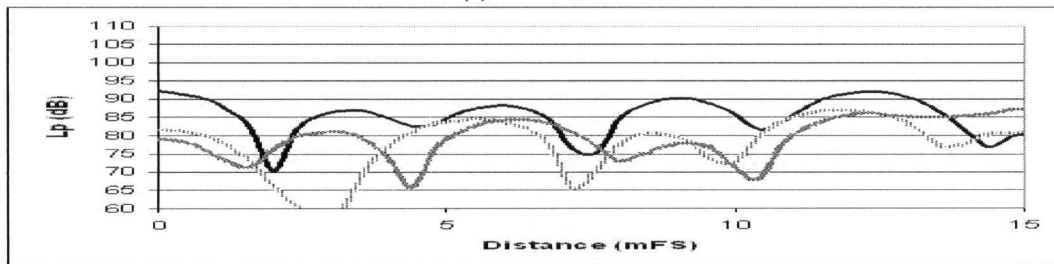


(d) 250 HzPT

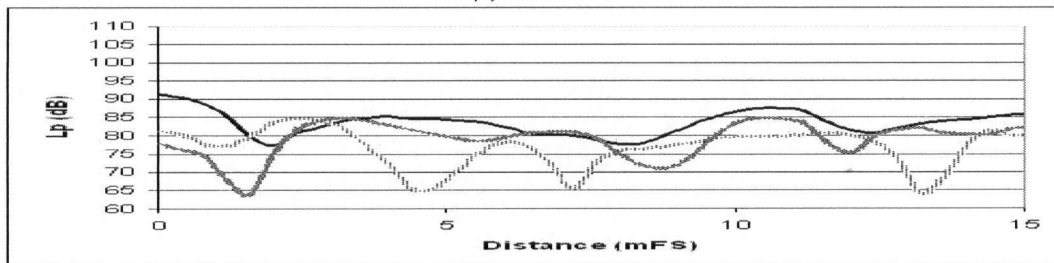
Figure 2.15. Measurements along Line 2 with the source output at 31.5, 63, 125 and 250 Hz pure tone. (Solid Black line – Empty, Dotted line – Small Fittings, Grey line – Large Fittings)



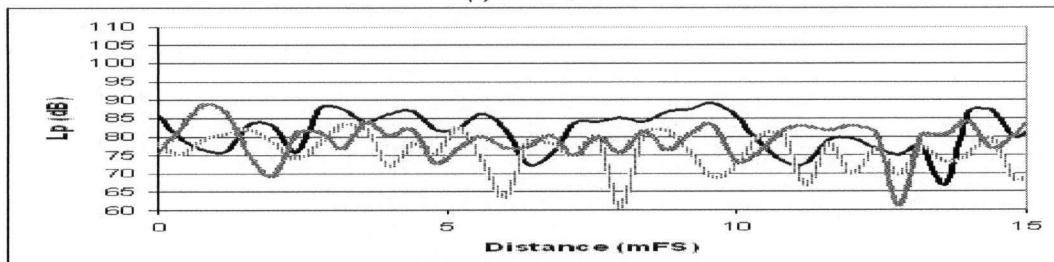
(a) 31.5 HzPT



(b) 63 HzPT



(c) 125 HzPT

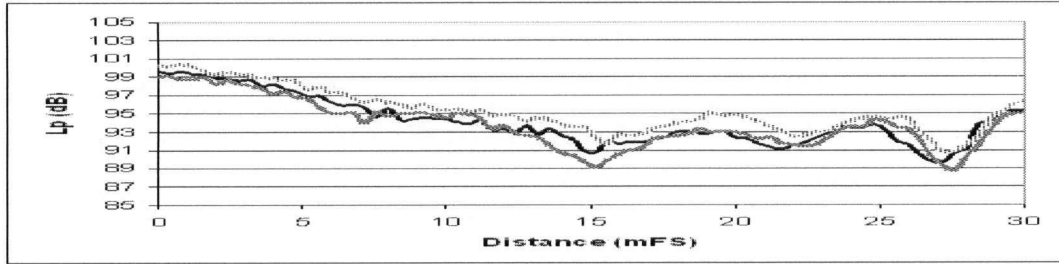


(d) 250 HzPT

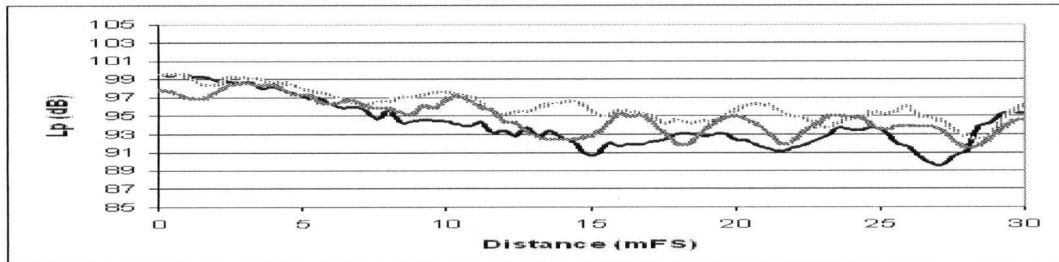
Figure 2.16. Measurements along line 3 of the source output at 31.5, 63, 125 and 250Hz pure tone. (Solid Black line – Empty, Dotted line – Small Fittings, Grey line – Large Fittings)

Figures 2.15 and 2.16 show the measured sound pressure levels along Lines 2 and 3, respectively, with pure tone output from the source. The trends follow those of Figure 2.14, with the small fittings tending to smooth the variation in sound pressure level and the higher frequencies having smaller peaks and dips than at the lower frequencies. As frequency is increased, the spatial variation in the sound pressure level is also increased. At 125 Hz along Line 2, the variation in sound pressure level with the small fittings is very similar to that of the large fittings. At 31.5 and 63 Hz along Line 3, the measured sound pressure level with both small and large fittings matches that of the empty case, suggesting that at very low frequencies, and far from the source, the fittings merely shift the modes slightly. This is also seen somewhat at 31.5 Hz along Line 2, with the small fittings. Moreover, at 31.5 Hz, both the large fittings and small fittings increased the overall sound level far from the source, as shown in the measurements along Line 3. At other frequencies, the addition of the fittings lowered the average sound level slightly.

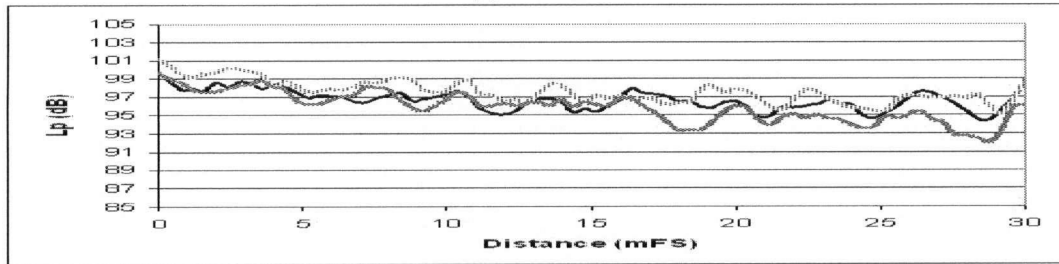
With octave band filtered noise output from the source, there was little modal response measured in the room. Figures 2.17, 2.18 and 2.19 show the measurement of sound pressure level along Lines 1, 2 and 3, respectively, with octave band limited noise output from the source. The addition of the fittings do not change the sound pressure level very much overall, and especially at the higher frequencies, 125 and 250Hz. This is in contrast to the measurements taken in the real workroom, which showed a highly



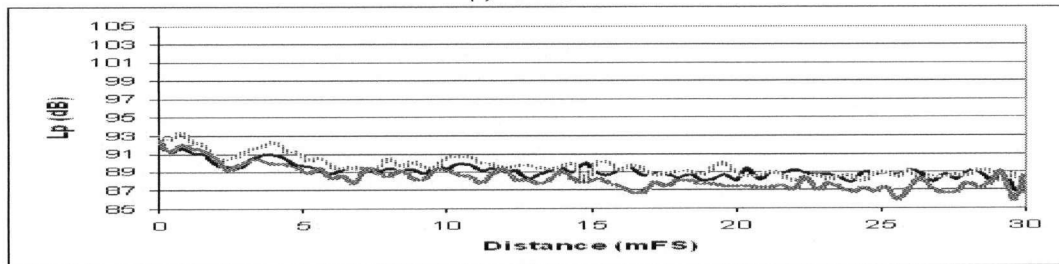
(a) 31.5HzOB



(b) 63HzOB

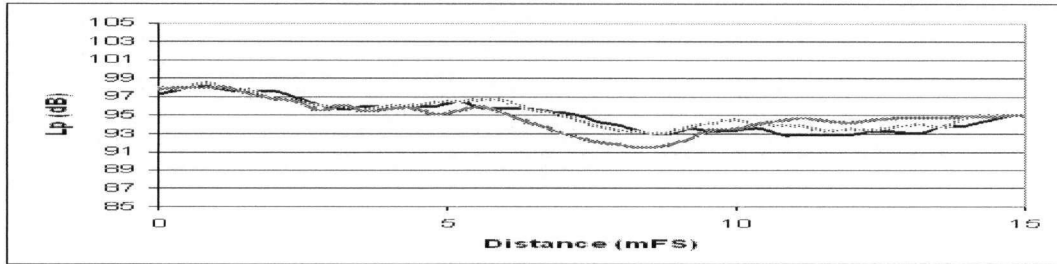


(c) 125HzOB

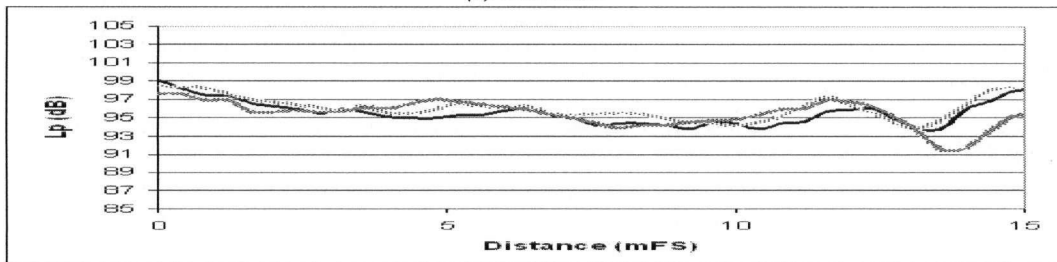


(d) 250 HzOB

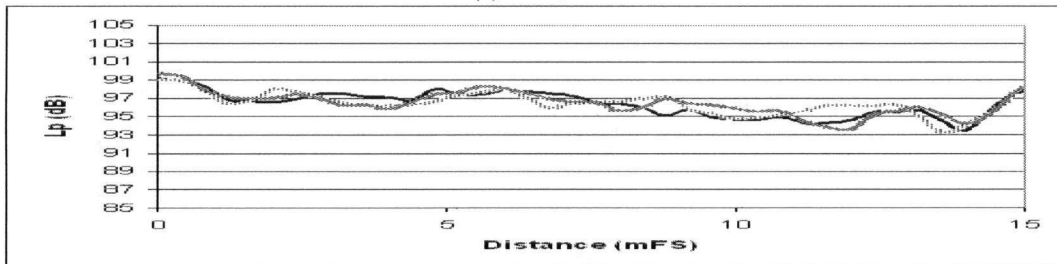
Figure 2.17. Measurements along Line 1 of the source output at 31.5, 63, 125 and 250Hz octave band. (Solid Black line – Empty, Dotted line – Small Fittings, Grey line – Large Fittings)



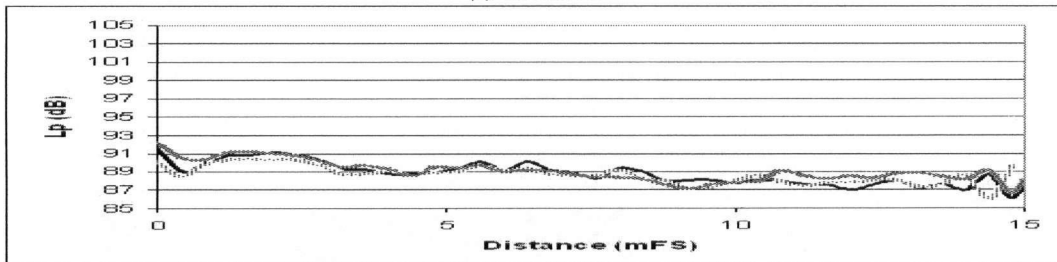
(a) 31.5HzOB



(b) 63HzOB

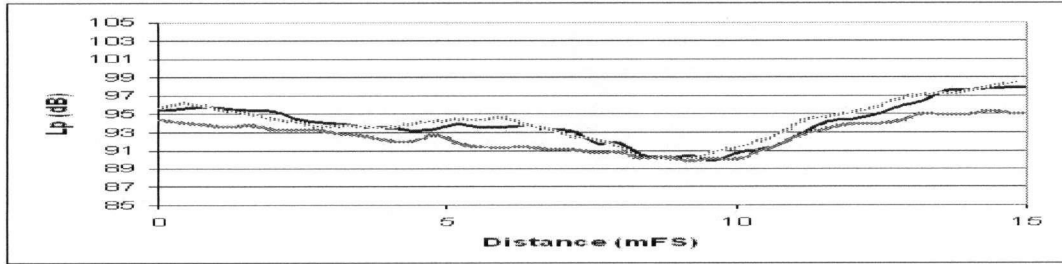


(c) 125HzOB

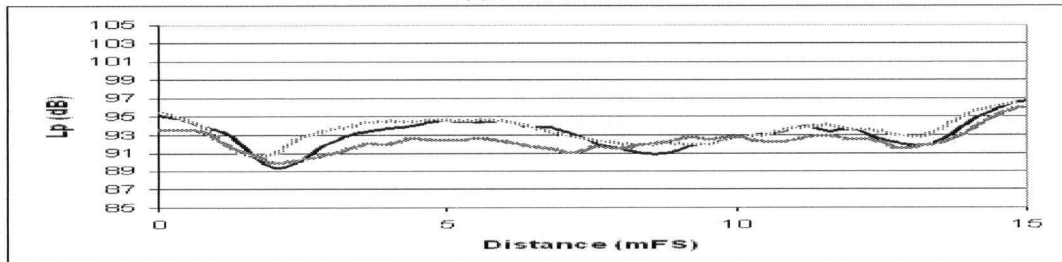


(d) 250 HzOB

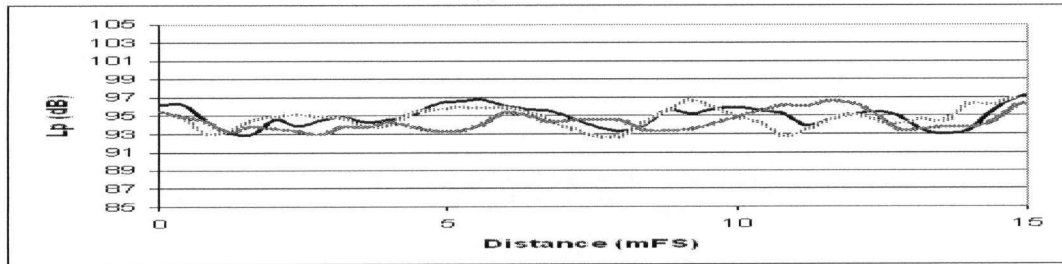
Figure 2.18. Measurements along line 2 of the source output at 31.5, 63, 125 and 250HzOB. (Solid Black line – Empty, Dotted line – Small Fittings, Grey line – Large Fittings)



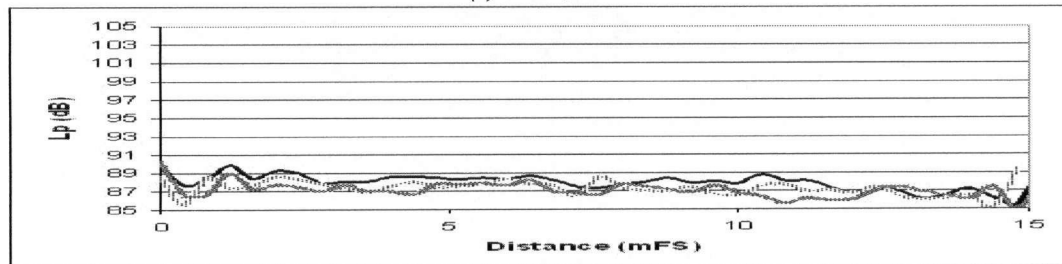
(a) 31.5HzOB



(b) 63HzOB



(c) 125HzOB



(d) 250 HzOB

Figure 2.19. Measurements along line 3 of the source output at 31.5, 63, 125 and 250HzOB. (Solid Black line – Empty, Dotted line – Small Fittings, Grey line – Large Fittings)

modal pattern in the room, with octave band noise output. At all of the measurements with the octave band noise, the sound pressure level at the far end of the room from the source increased, to a maximum at the wall.

2.2.4 Summary

With pure tone output from the source, the small fittings tended to smooth the variation in sound pressure level along the length and widths of the room. Both the large and small fittings affected the sound field in the room to a large degree. As frequency increased, the modal variation also increased, as expected because of the shorter wavelengths of higher frequency sound. With octave band filtered noise output from the source, the measured lines showed very little difference in the sound pressure level with the introduction of both the small and large fittings. Very little modal response was measured, in this case.

2.3 Comparison between scale-model and real workroom measurements

In both the scale model workroom and in the real workroom, it was found that the addition of fittings caused a dramatic change in the sound field in the room, despite their small sizes relative to the wavelength. However, with octave band limited noise output from the source, the scale model measurements did not show any modal-type response as

was measured in the real workroom. Also, increased variation in the sound field in the room was expected with increased frequency – this was measured in the scale-model room, but not in the real workroom. The two empty configurations are similar in that they display a smooth decrease in the sound level with increasing distance from the source, as expected.

2.4 Anechoic Chamber Tests

2.4.1 Equipment Setup

In order to determine the effect of the fittings without the influence of the room, an experiment was devised in a hemi-anechoic environment to measure the effect of the fittings on the sound field with only the influence of the source, floor, and the fittings. A floor consisting of $\frac{3}{4}$ " plywood was placed over the mesh floor of the anechoic chamber, effectively rendering it a hemi-anechoic chamber. The floor-plan dimensions of the scale-model room were outlined on the floor, and the measurements were taken along the same lines and at the same scale as the scale model measurements. The microphone was set at the same height and positions along the layout plan of the floor. The same source and fittings were used in the anechoic chamber, with the three setups – empty, large fittings, small fittings – as before. The only difference was that the walls and ceiling were absent.

2.4.2 Results and Discussion

The measurement results along Line 1 are shown in Figure 2.20 below. At each of the frequencies the empty case shows the expected result of a monotonically decreasing sound pressure level with increasing distance from the source. At 31.5 and 63 Hz pure tone with the addition of the small fittings, there is little variation on the sound pressure level with distance. However, at 125 and 250 Hz pure tone, the small fittings cause some change in the measured sound field. At 250 Hz pure tone the small fittings caused a decrease in the sound pressure level close to the source, and a slight increase far from the source. Large fittings have a minimal effect on the sound field at 31.5 Hz pure tone, but with the higher frequencies tested, show quite a large difference from the empty case. The large fittings are 2 mFS in size, and with the wavelength of a 63 Hz pure tone being about 5.4 m long, the large fittings are almost half a wavelength long. At 125 and 250 Hz pure tone, the large fittings cause a decrease in the sound pressure level far from the source, while at 63 Hz pure tone, there are modal variations measured, caused by reflections between and among the fittings.

As with the measurements along Line 1, the Line 2 measurement results in Figure 2.21 show little effect of the small fittings on the sound pressure level with increasing

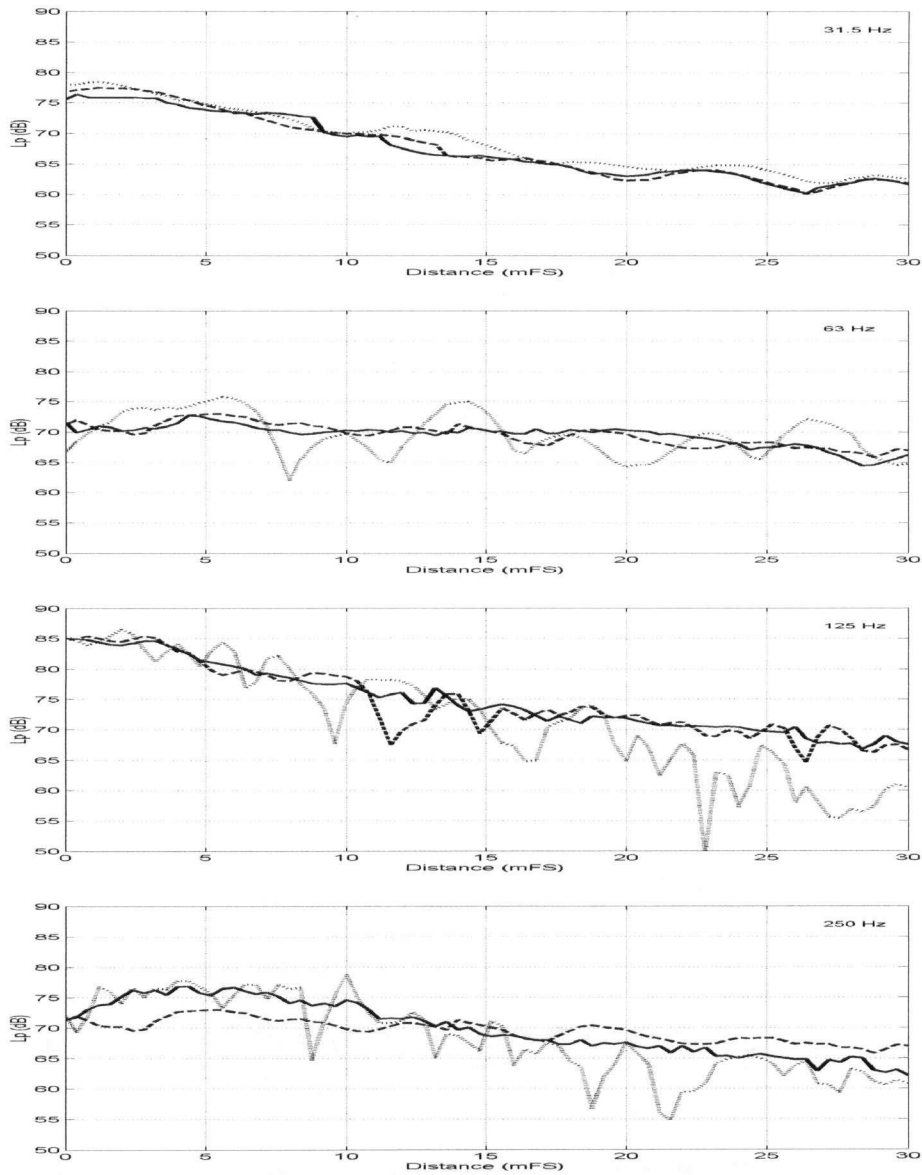


Figure 2.20. Measurements along Line 1 of the source output at 31.5, 63, 125 and 250 Hz pure tone. (Solid Black Line – Empty, Dashed Line – Small Fittings, Dotted Line – Large Fittings)

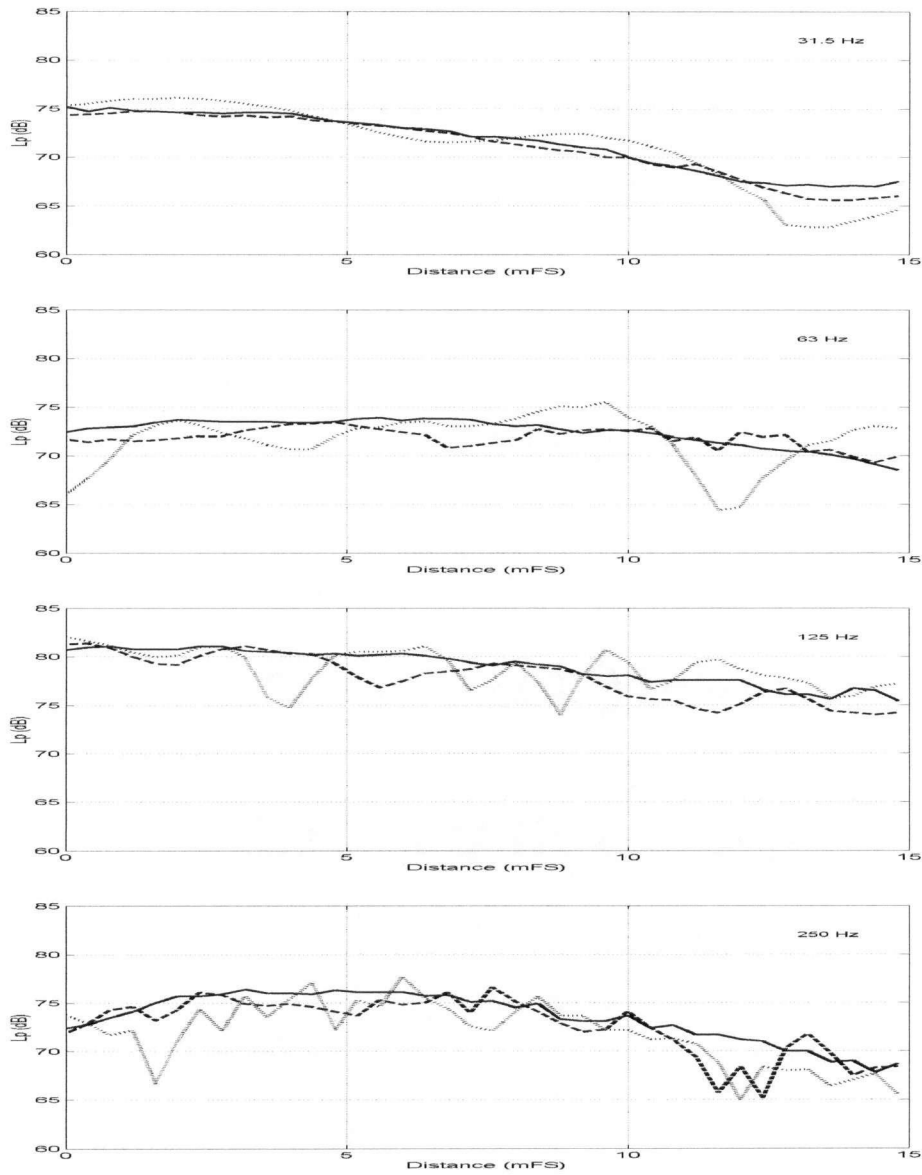


Figure 2.21. Measurements along Line 2 of the source output at 31.5, 63, 125 and 250 Hz pure tone. (Solid Black Line – Empty, Dashed Line – Small Fittings, Dotted Line – Large Fittings)

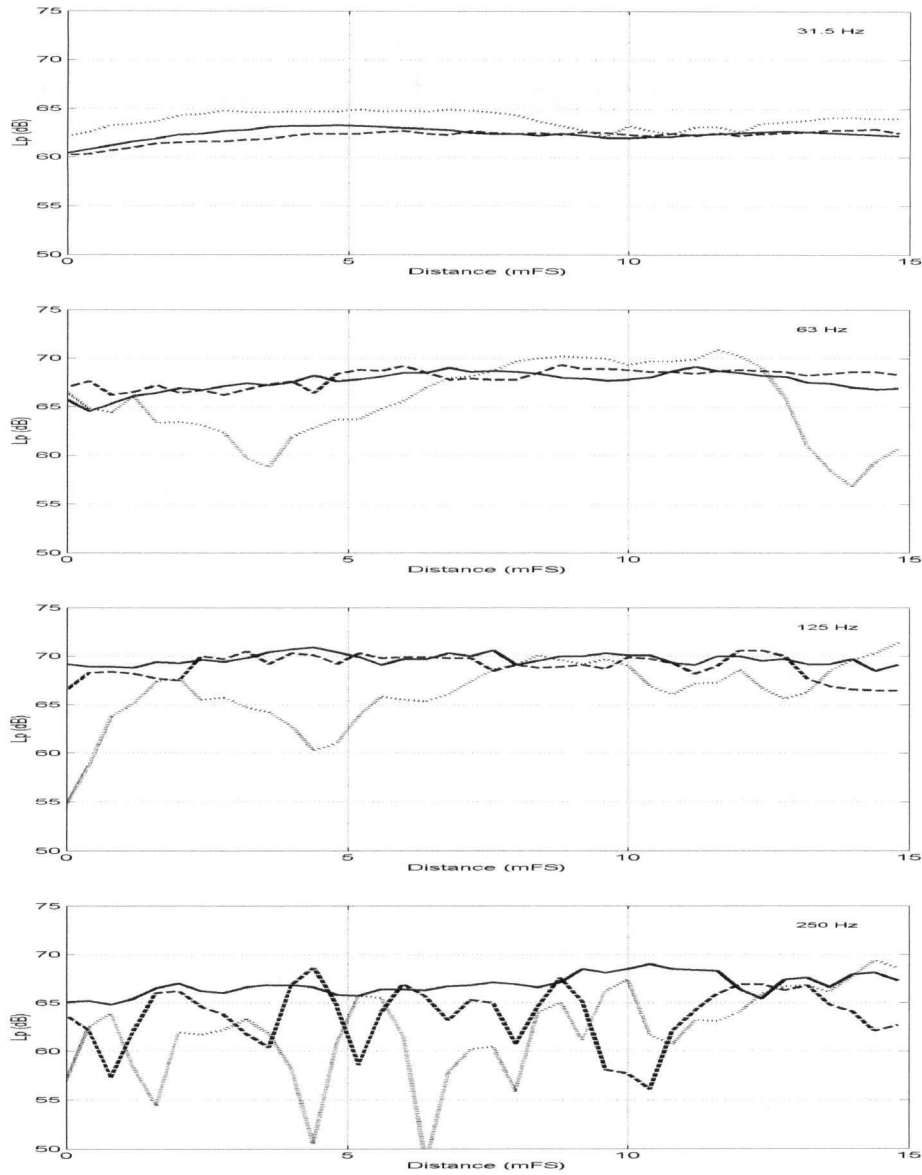


Figure 2.22. Measurements along line 2 of the source output at 31.5, 63, 125 and 250 Hz pure tone. (Solid Black Line – Empty, Dashed Line – Small Fittings, Dotted Line – Large Fittings)

distance from the source. The sound field is highly affected by the large fittings. More interference effects due to the fittings are present at the higher frequencies, where the fittings are approaching a size closer to a wavelength or half of a wavelength at the output frequency. With the addition of the fittings, there is no appreciable decrease in the sound pressure level with distance compared to the empty case, other than due to interference effects. This fits well with the fact that there is little damping in the room due to the fittings and the floor.

Along Line 3, across the width of the room, far from the source, the fittings have a much greater effect on the sound field. At 31.5 Hz, there is little variation from the empty case, although the L_p is consistently higher. At 63 Hz, there are two places where there is a large amount of cancellation. At 125 Hz, at 0 m, there is a large dip in the L_p of almost 15 dB and another at about 4.5 m, but the L_p matches the empty case from 7 m on up to 15 m. At 250 Hz, with the small and large fittings, the L_p stays almost consistently below that of the empty case along Line 3. The large fittings cause a much higher level of interference effect than do the small fittings.

2.5 Comparison between the Anechoic Chamber and Scale-Model Measurements

At 31.5Hz, the introduction of the fittings in the anechoic chamber caused very little change in the sound-pressure level. In the scale-model room, however, there was a

lot of variation in the sound pressure level measured with increasing distance from the source. This shows that the room (and its interaction with the fittings) causes the same variation in sound pressure level as was measured in the scale model room. The fittings alone cause little change in the sound field without a room. This is supported by theory; sounds with wavelengths much, much larger than the obstacle are affected minimally by the fittings.

At higher frequencies in the scale-model room, the small fittings were found to smooth out the variation in sound pressure level in the room, with smaller and fewer dips and peaks when empty and containing large fittings. As mentioned in the scale-model measurement discussion, this may be caused by the small fittings breaking up some of the modes through small reflections and perturbations in the sound field (i.e., acting as diffusing objects), making a more diffuse room such that fewer modes are present in the room. In the anechoic chamber, however, the measurement results with the fittings showed that there were some reflections and interference effects occurring in the room at the higher frequencies tested.

Chapter 3

Prediction

3.1 Approaches

Two suitable prediction approaches – a modal model and an image-phase model – were chosen to attempt to model the sound field in the workroom and the scale model under the empty condition (no fittings). With low-frequency sound and its long wavelengths, and the application of this work in the use of active noise control, it was necessary to take phase into account. Phase was also required to accurately model the non-infinite-impedance walls, which greatly affect the modal pattern in the room because of their complex reflection characteristics. Both the modal and image-phase models include phase, predict at single discrete frequencies, and take into account the reflection coefficients of the bounding surfaces.

A third prediction approach – the finite-element method - was employed to model the effects of the fittings in a room. Whereas the modal and image-phase models only work with empty rooms, the finite element method is able to calculate the sound field in a room based on the boundary conditions, including those associated with fittings.

FEMLAB was used to develop a model to predict the sound field in a hemi-anechoic environment, when empty and fitted.

3.2 The Modal Model

The modal model calculates the sound field in an enclosed space through a summation of the contributions of each mode that is excited in the room by a point source. The model is based on solutions to the inhomogeneous Helmholtz equation for a rigid-walled rectangular room, to which a modifying damping term is added to determine the room response with lightly damped walls [16].

The Helmholtz equation for the eigenfunctions, ψ_n , of a rigid-walled enclosure is given by,

$$\nabla^2 \psi_n(x) + k_n^2 \psi_n(x) = 0, \quad (3.1)$$

as before (Eq. (1.2)). Using a Green's Function to solve the Helmholtz equation, assuming initially that there is no wall vibration contributing to the pressure field within the enclosure and that there is a volume-velocity point source within the enclosure, we can derive the following equation [10],

$$p(x) = \sum_{n=0}^{\infty} \frac{j\omega\rho_o c_o^2 \psi_n(x)}{[\omega c_o D_{nn} - j(\omega^2 - \omega_n^2)]} \int_V q_{vol}(y) \psi_n(y) dV \quad (3.2)$$

where ω is the source excitation frequency, ρ_o and c_o are the density and speed of sound in air, respectively, D_{nn} is a modifying damping term, and $q_{vol}(y)$ is the source volume

velocity, with y used to denote the position of the source within the enclosure. D_{mn} is defined by the following integral,

$$D_{mn} = \frac{1}{V} \int_S \beta(y) \psi_n(y) \psi_n(y) dS, \quad (3.3)$$

where $\beta(y)$ is the normalized acoustic admittance of the surface, defined as the inverse of the normalized acoustic impedance of surface S , $Z(y)$,

$$\beta(y) = \frac{\rho_o c_o}{Z(y)}. \quad (3.4)$$

We can specify a point monopole source as a delta function, such that $q_{vol}(y) = q_s \delta(y-y_s)$, with y_s being the position of the source in the enclosure. This simplifies the integral of Eq. (3.2),

$$p(x) = \sum_{n=0}^{\infty} \frac{j\omega\rho_o c_o^2 \psi_n(x)}{V[\omega c_o D_{mn} - j(\omega^2 - \omega_n^2)]} q_s \psi_n(y_s). \quad (3.5)$$

Thus with Eq. (3.5), we can calculate the pressure at any given point in the room, $x=(x_1, x_2, x_3)$, due to a source at position $y=(y_1, y_2, y_3)$. Appendix B describes the derivation of the Green's Function solution for the Helmholtz equation in more detail.

3.2.1 Implementation

The modal model was programmed in MATLAB. It first requires calculation of the eigenvalues of the room by way of Eq. (1.6). The number of modes to include depends on the frequency of the source output and the dimensions of the room. As

frequency is increased, the number of modes in the room increases. Thus, a higher number of modes must be included in the calculations. Room dimensions also play a role in the modes, since the frequency (or wavelength) of the modes generated are related to the distances between opposite walls (Eq. (1.5)). If the source output frequency is below the frequency of the modes possible in the room, few of the higher modes will be excited, so fewer modes need to be included in the calculation. If the room dimensions are large, many low-frequency modes will be excited by the source and more modes must be included.

After calculation of the eigenfrequencies, the specifications of the room are input and the sound pressure level at a specified receiver points throughout the room are calculated. The inputs required are the source excitation frequency, the dimensions of the room, the surface impedance, the horizontal grid spacing of the receiver points and the number of modes to include in the calculation. Through an iterative summation of the contribution of the modes, the program calculates the contribution of each mode using Eq. (4.9).

3.3 Image-Phase Model

The image-phase model [10] calculates the sound field at a receiver point by summing the energy received directly from the source, as well as through reflections.

Where a boundary is present, an image is placed symmetrically on the far side of the boundary. This allows the simple calculation of the energy propagated to the receiver

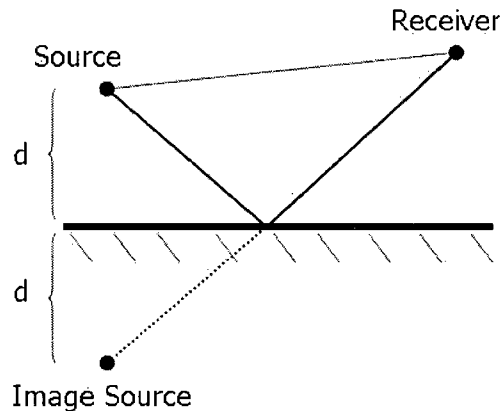


Figure 3.1. Illustration of the image-phase model concept.

point along a line, accounting for the impedance of the boundary. Figure 3.1 illustrates the source, image source, receiver and the reflecting boundary.

The model can be extended to calculate the sound field in a room, taking into account each boundary that reflects. The number of images then corresponds to the number of reflections taken into account in the calculations. If we let q be the complex source strength and Z_r the complex acoustical transfer impedance from the real source to the receiver, we can specify the complex sound pressure radiated by the point source to be

$$p(r) = qZ_r = q \frac{i\omega\rho_0 e^{-ikr}}{4\pi r}, \quad (3.6)$$

where r is the distance from the source to the receiver position, ω is the source output frequency, ρ_o is the density of air and k is the wavenumber. With six walls, as would exist in a rectangular room, assuming they are rigid, the reflections/images must be taken into account in the transfer impedance as [10]

$$Z_r(X, X') = \frac{i\omega\rho_o}{4\pi} \sum_{p=1}^8 \sum_{r=-\infty}^{\infty} \left[\frac{e^{-ikR_p}}{R_p} + \frac{e^{-ikR_r}}{R_r} \right], \quad (3.7)$$

$X=(x,y,z)$ are the coordinates of the source position and $X'=(x',y',z')$ are the coordinates of the receiver position. R_p represents the eight vectors given by the eight permutations over \pm of $R_p = (x\pm x', y\pm y', z\pm z')$. r is the integer vector triplet (n, l, m) , with $R_r = 2(nL_x, lL_y, mL_z)$ for the enclosure dimensions (L_x, L_y, L_z) .

With the addition of damping terms to account for the vibration and absorption of each of the non-rigid walls, the acoustical transfer impedance becomes the following:

$$Z_r(X, X') = \frac{i\omega\rho_o}{4\pi} \sum_{p=0}^l \sum_{r=-\infty}^{\infty} \beta_{x1}^{|n-q|} \beta_{x2}^{|n|} \beta_{y1}^{|l-j|} \beta_{y2}^{|l|} \beta_{z1}^{|m-s|} \beta_{z2}^{|m|} \frac{e^{-ik|R_p+R_r|}}{|R_p+R_r|}, \quad (3.8)$$

where R_p is now expressed in terms of the integer vector $p = (q, j, s)$ as

$$R_p = (x - x' + 2qx', y - y' + 2jy', z - z' + 2sz'), \quad (3.9)$$

to account for the images of the images. β_{x1} , β_{x2} , β_{y1} , β_{y2} , β_{z1} , and β_{z2} are the pressure reflection coefficients of the six walls, assumed to be independent of the angle of

incidence. The β are complex, and can describe both the absorption and vibration characteristics of a wall.

The image-phase model requires input of the room dimensions, the source positions, the receiver positions, and the reflection coefficients of the walls. Also required is the image number, which determines the number of images to consider in the calculation of the sound field. The number of images and the resolution of the receiver grid are directly related to the computational time of the program.

3.3.1 Validation

In order to validate the modal model, predictions were first made to test convergence of the model. A simple case of a square room, 5m x 5m x 1m high was considered and several predictions run using an increasing number of modes to investigate convergence. The resolution, or the grid spacing for the receiver points was set at 0.10m, and the receiver height was set at half of the height of the room, 0.5m. The reflection coefficients of the room surfaces were set to 1, for complete reflection. The results of the modal-model predictions were plotted using Matlab, and the profiles compared. As Figure 3.2 shows, the results do not change significantly when more than 1000 modes are taken into account. These results were also compared to hand calculations of the modes present in the room, and they compare favourably. Next, comparisons were made with the Image-

Phase model. Predictions of the sound field in the empty scale-model room were also performed.

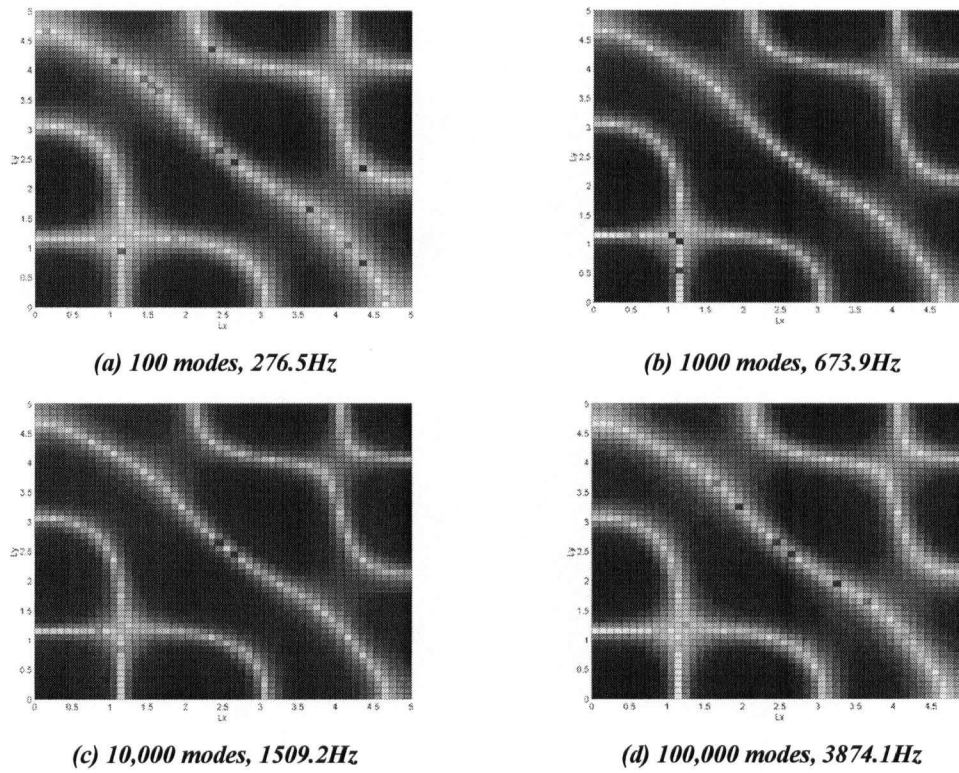
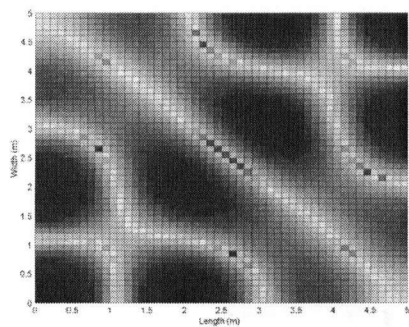


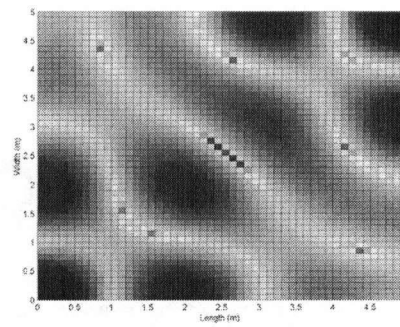
Figure 3.2. Test for convergence of the Modal Model.

3.3.2 Comparison between the Modal Model and the Image Phase Model

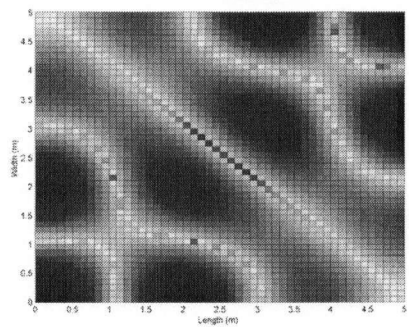
With the convergence and validation of the modal model investigated, the next step was to validate the image-phase model. The same inputs were used in the image-phase model: room dimensions of 5m x 5m x 1m, source in one corner of the room (0,0,0), reflection coefficient of 1, receiver-grid spacing of 0.10 m and a receiver height of 0.5 m. Figure 3.3 shows the results for 50, 100 and 150 images compared to the modal-model prediction with 100,000 modes.



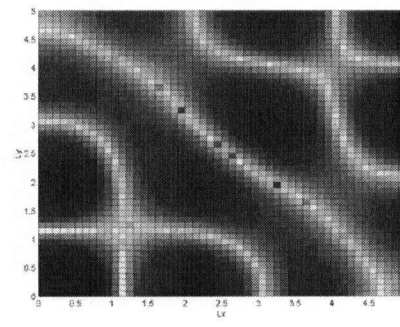
(a) Image-Phase prediction with 50 Images



(b) Image-Phase prediction with 100 Images



(c) Image-Phase prediction with 150 Images



(d) Modal Model prediction with 100,000 modes

Figure 3.3. Comparison of the modal model with the Image-Phase model.

With 50 images, the Image-phase model compares well with the modal-model, except that the dips in the modes are less well defined. Increasing the number of images increases the accuracy of the prediction and gives a better-defined picture of the modes in the room. However, this is not the case with 100 images - the prediction shows even less well-defined modes in the room. The number of images was increased yet again to 150 to find a convergent result from the image-phase model: the results proved to be quite comparable to the modal-model result. With a higher reflection coefficient the image-phase model required more images to reach convergence; with a lower reflection coefficient, the energy dissipated faster, and convergence to the true sound pressure level reached sooner. With each successive image, there would be very little decay in the energy from the source to the receiver position, and the only decay would come from air absorption. Thus if no air absorption were present, theoretically an infinite number of images must be taken into account in the prediction of a room with no damping of the walls. With the modal model, we have an exact representation of the sound field with zero damping and convergence is quite rapid as long as a sufficient number of modes are taken into account. In Eq. (3.5), as the modal number, n , increases, ω_n becomes large and the contribution of the higher modes becomes small.

The calculation times for the modal model are relatively short – with the precalculation of the eigenvalues, even taking into account the first 350,000 modes,

Matlab requires less than 30 minutes of processing time. For the image-phase model, however, the processing times are very long, and they are dependent on the 'measurement grid', the number of images, and the reflection coefficient of the surfaces of the room. For the 5m x 5m x 1m room, a resolution of 0.1m over the entire room, 150 images and a reflection coefficient value of 1, the model requires well over a day to run on a Pentium 4 1.8 GHz computer with 512 MB of RAM.

With calculation times in mind, for the comparison of the modal model with the image-phase model, reflection coefficients smaller than 1, as well as a lower resolution, were used. In anticipation of modeling the scale-model room, using the transfer-matrix approach described in Appendix C, an approximate impedance (and the corresponding reflection coefficient value) was calculated with the scale model's surface properties, as listed in Table 3.1. The predicted boundary impedances and reflection coefficients of the plywood walls are listed in Table 3.2. These values were used in both of the prediction models and the predictions compared.

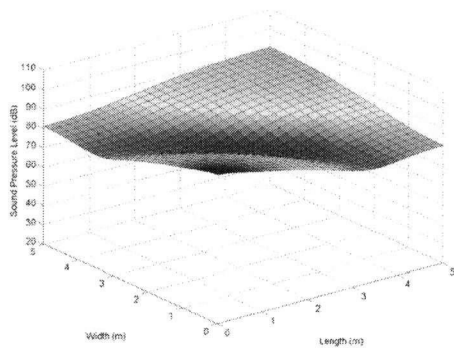
Table 3.1 Average properties of plywood, as used in the calculation of the impedance of the scale-model walls.

| <i>Plywood Property</i> | <i>Value</i> |
|-------------------------|----------------------|
| Poisson's ratio, ν | 0.4622 |
| Young's Modulus, E | 2.049×10^9 |
| Density | 575 kg/m^3 |

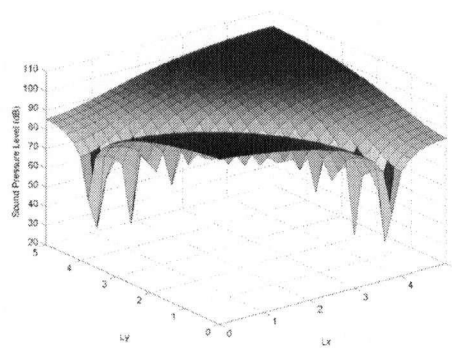
Table 3.2. Complex impedances and reflection coefficients calculated by the transfer-matrix method using the scale model plywood boundary properties.

| | <i>31.5Hz</i> | <i>63Hz</i> | <i>125Hz</i> | <i>250Hz</i> |
|--|---------------|-------------|--------------|--------------|
| <i>Normalized Complex Impedance, Z</i> | 1 + 3.4827i | 1 + 6.9654i | 1 + 13.8202i | 1 + 27.6405i |
| <i>Real Reflection Coefficient, R</i> | 0.7520 | 0.9238 | 0.9795 | 0.9948 |

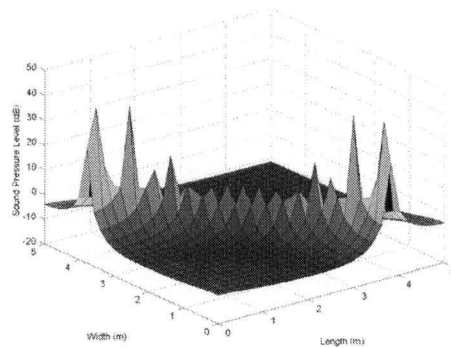
The room was defined as a 5m x 5m x 1m high room, as before, with the receiver at 0.5 m high, and the receiver grid with 0.2m resolution. The comparison at 31.5Hz is shown in Fig. 3.4, along with a graph of the difference between the two outputs (image-phase output minus modal-model output). The major difference between the image-phase and the modal-model is along the modal node that runs diagonally across the room. The modal model predicts much greater cancellation, and lower levels, along the modal dip than does the image-phase model. Also, as can be seen from the difference graph, the modal-model is shown to predict about 10 dB higher levels overall compared to the image-phase model. This may be caused by the lack of convergence in the image-phase model. Fig. 3.5 shows plots with the image-phase model re-run to include 175 images. The difference in output between the image-phase model and the modal-model remains 10 dB. Fig. 3.6 shows the results with the frequency now increased to 63 Hz, and the image order set to 75. The difference between the two models is now less than 2 dB, other than at the modal nodes.



(a) Image-phase model, 75 Images



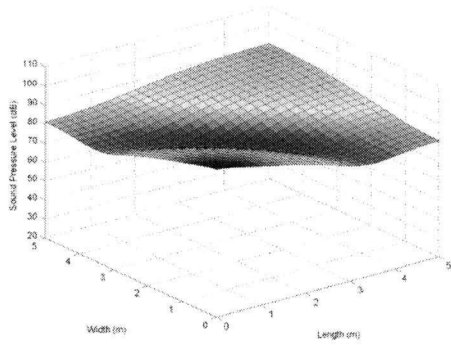
(b) Modal model, 100,000 modes



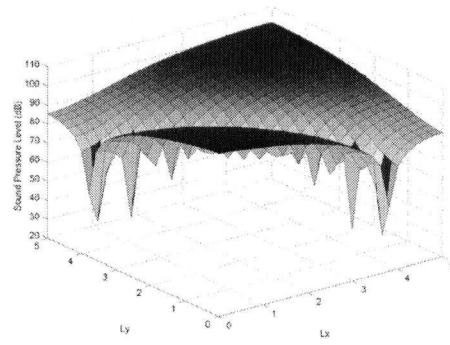
(c) Difference

Figure 3.4. 31.5Hz in the 5x5x1 room, with 75 images and 100,000 modes.

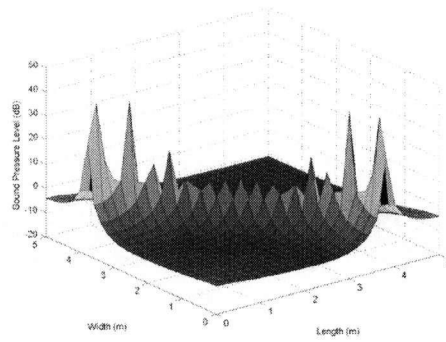
Increasing the number of images to 175, shown in Fig. 4.7, shows little difference compared to using 75 images. At 125 Hz, the difference in overall sound pressure level is very small, with the only differences again being at the modal nodes. Very little difference is seen with an increase in image order to 175. At 250 Hz, there is a large difference between the two prediction models.



(a) Image-phase model, 175 Images

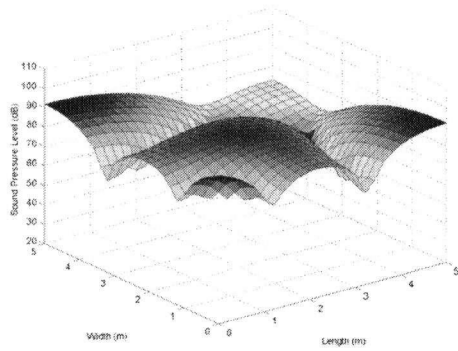


(b) Modal model, 100,000 modes

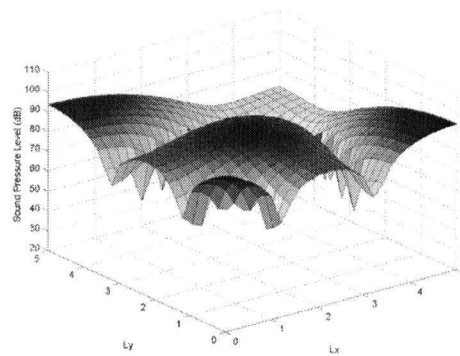


(c) Difference

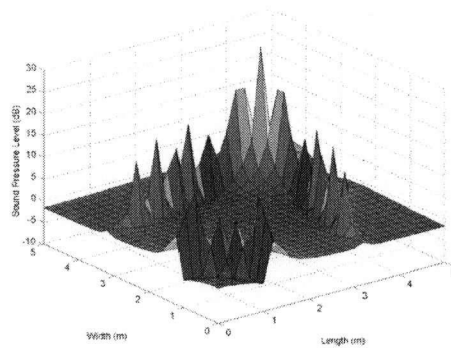
Figure 3.5. 31.5Hz in the 5x5x1 room, with 175 images and 100,000 modes.



(a) Image-phase model, 75 Images

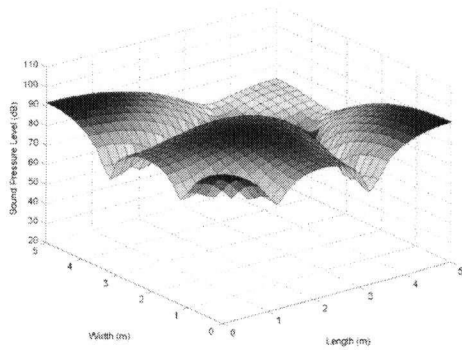


(b) Modal model, 100,000 modes

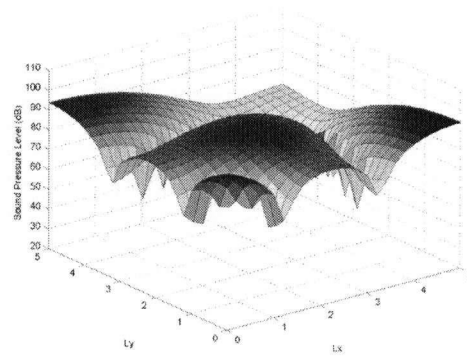


(c) Difference

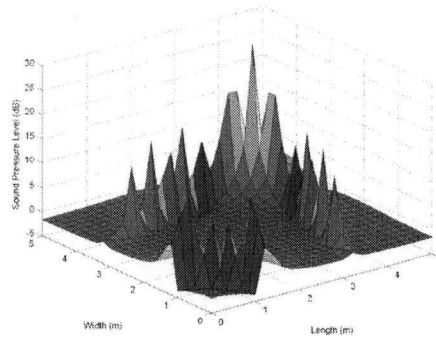
Figure 3.6. 63Hz in the 5x5x1 room, with 75 images and 100,000 modes.



(a) Image-phase model, 175 Images

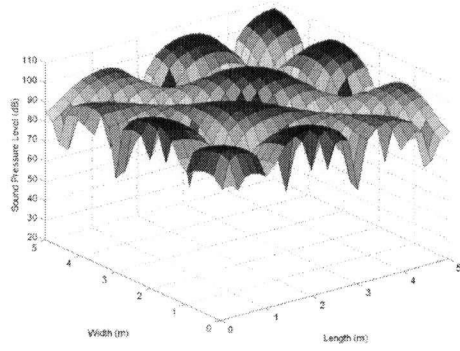


(b) Modal model, 100,000 modes

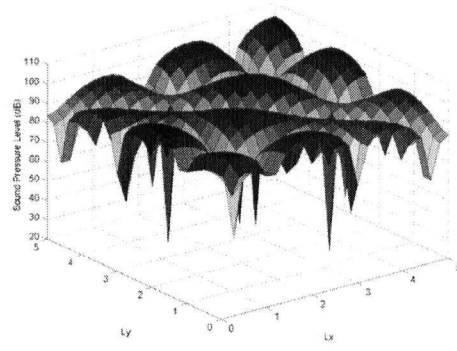


(c) Difference

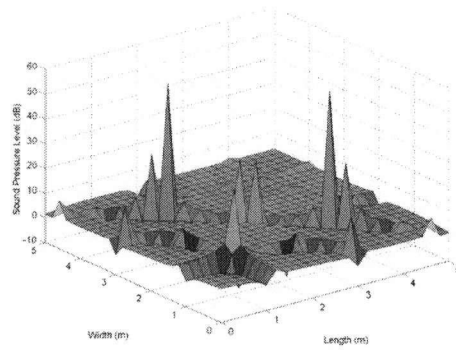
Figure 3.7. 63Hz in the 5x5x1 room, with 175 images and 100,000 modes.



(a) Image-phase model, 75 Images

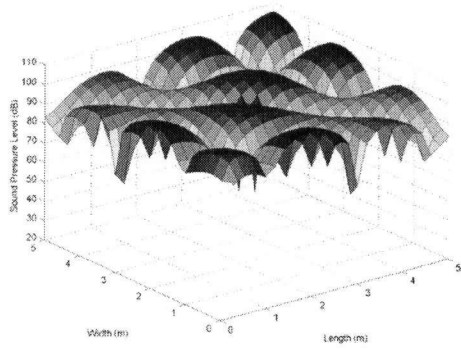


(b) Modal model, 100,000 modes

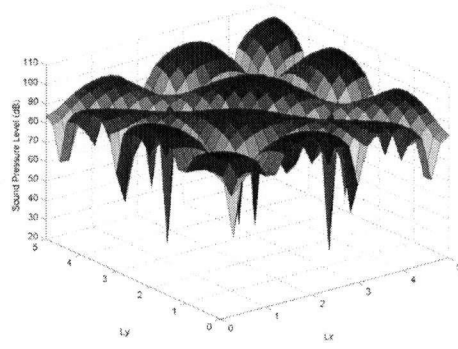


(c) Difference

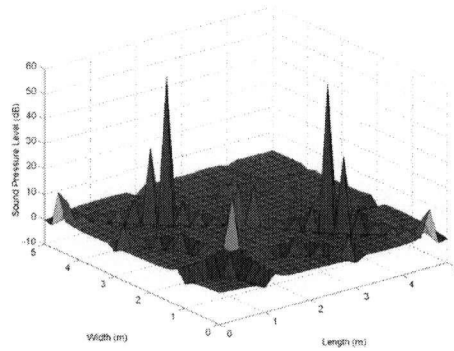
Figure 3.8. 125Hz in the 5x5x1 room, with 75 images and 100,000 modes.



(a) Image-phase model, 175 Images

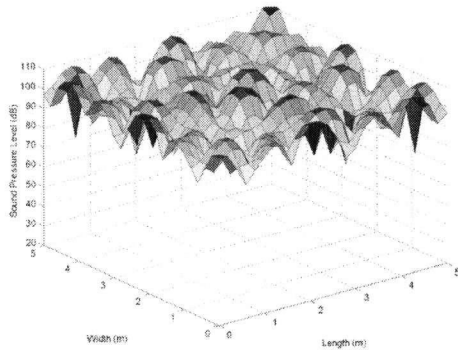


(b) Modal model, 100,000 modes

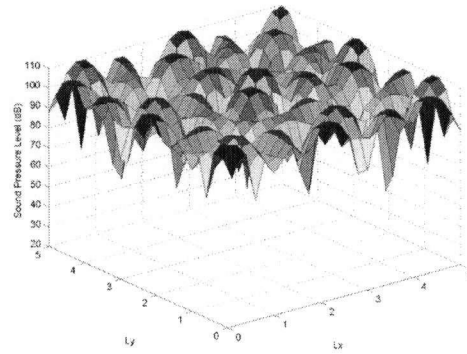


(c) Difference

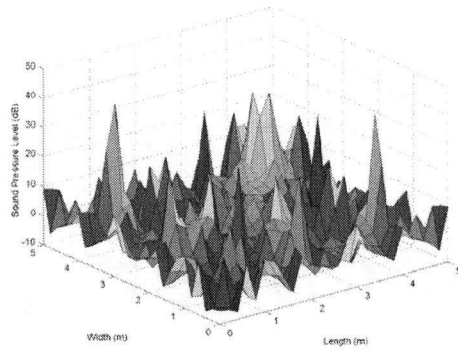
Figure 3.9. 125Hz in the 5x5x1 room, with 175 images and 100,000 modes.



(a) Image-phase model, 75 Images



(b) Modal model, 100,000 modes



(c) Difference

Figure 3.10. 250Hz in the 5x5x1 room, with 75 images and 100,000 modes.

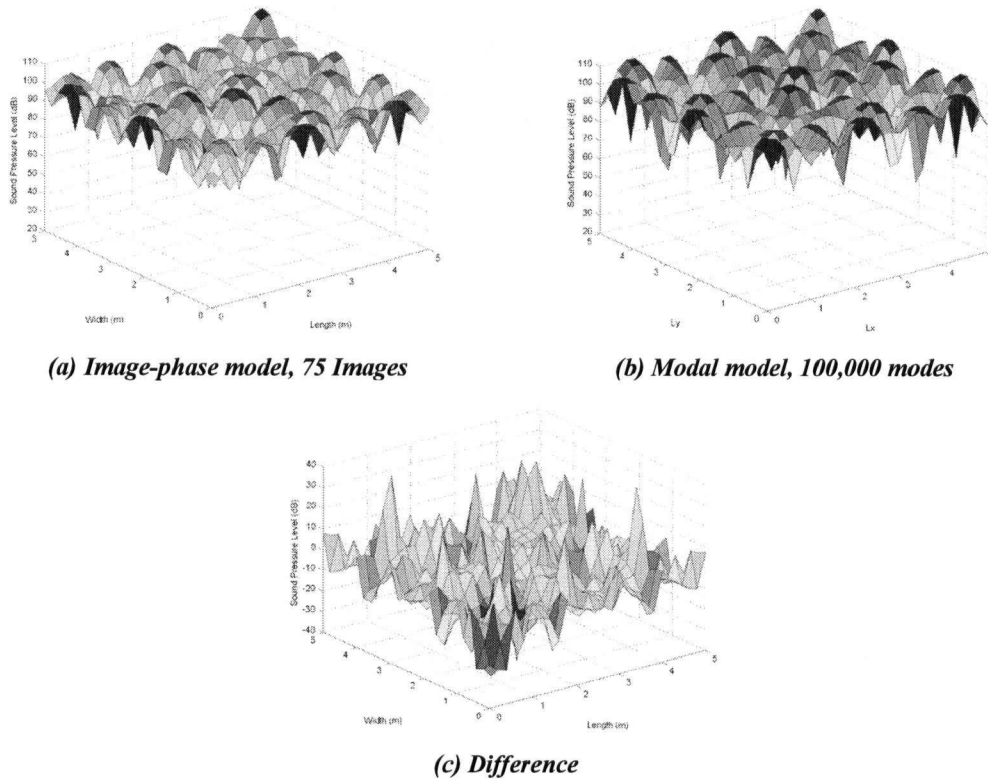


Figure 3.11. 250Hz in the 5x5x1 room, with 75 images and 100,000 modes.

Overall, the outputs of the two models match reasonably well, with both predicting similar modal patterns. Some differences are seen in the prediction of the modal nodes, and also in differences in the magnitudes of the sound pressure levels in the room. This may be due to the slight difference in boundary-condition inputs to the two models. The modal-model works with the complex impedance, while the image-phase model only accepts real impedances. Since the complex impedance affects both the

phase as well as the magnitude of the reflected wave, the phase change upon reflection is not accounted for in the purely real reflection coefficient. The image-phase prediction model only accounts for the decrease in magnitude of the reflected wave. This may account for the slight differences in the two models.

3.3.3 Scale Model

The sound field in the scale model was modeled using both the image-phase and the modal models. The full-scale dimensions and the measured absorption coefficient of the scale model were input into the models, and the predictions were performed for the same pure-tone frequencies as tested in the scale model. Since the measured absorption coefficients were real-valued and not complex, a real absorption coefficient was input to the modal model. The predicted results were compared along the same measurement lines as in the scale model.

Fig 3.12 shows the measured and predicted sound pressure levels along Line 1 in the scale-model room. At 31.5 Hz the shape of the measured modes in the scale model room shows some similarities to the two predicted curves. The modal nodes measured with the modal model at about 7.5 m, 18 m and at 26 m were also predicted with the modal model. The measured sound pressure level in the scale-model room shows some influence of higher

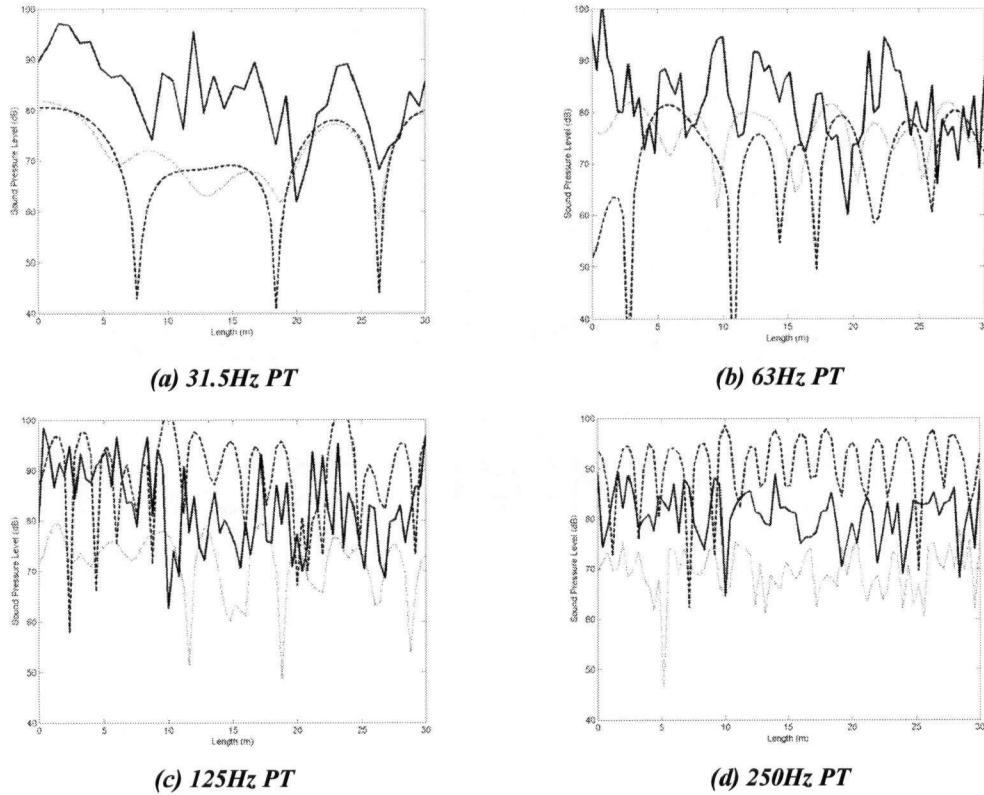


Figure 3.12 Measured and predicted sound pressure levels along Line 1 in the scale model room. Solid line indicates measured, dashed is modal model, and dotted is image-phase model.

frequencies, indicated by the many more peaks and dips in the measured sound pressure level. The measured sound pressure level response at higher frequencies - 63, 125 and 250 Hz - show much less resemblance to the predicted response. This may be due to the influence of the wall vibration that was present during measurement (the source was located close to the lightweight walls which experiences strong acoustical excitation and

reradiated sound) and is not accounted for in either of the models. The influence of the wall vibration is also not accounted for in the absorption coefficient determination.

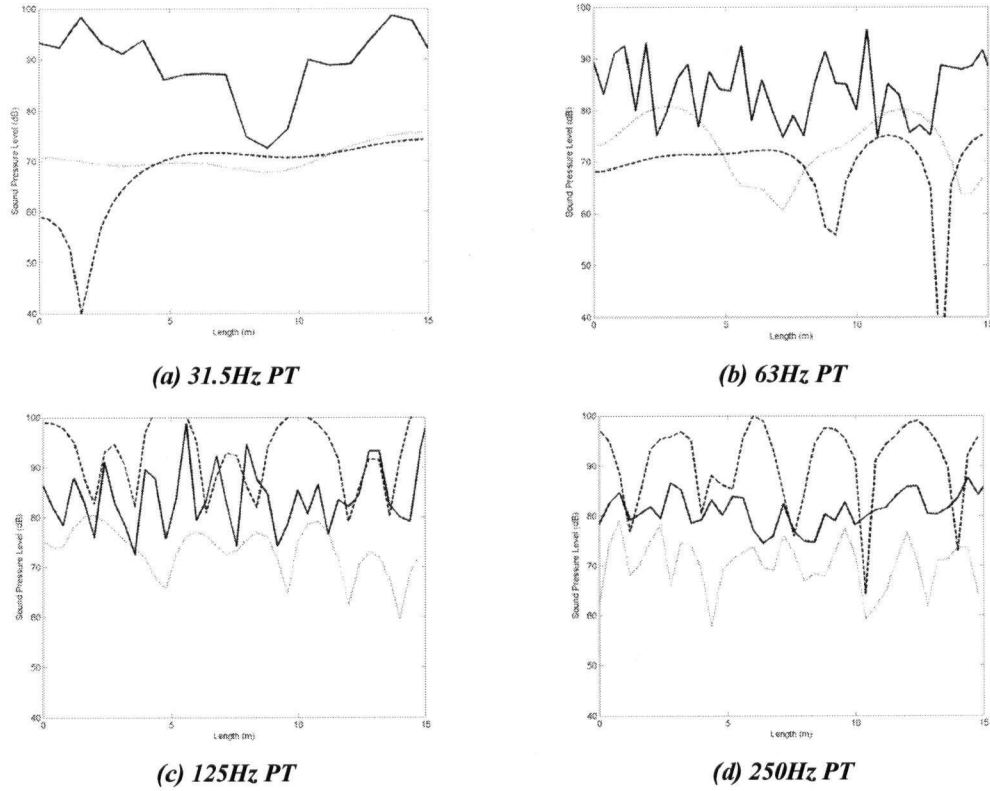


Figure 3.13 Measured and predicted sound pressure level along Line 2 in the scale model room. Solid line indicates measured, dashed is modal model, and dotted is image-phase model.

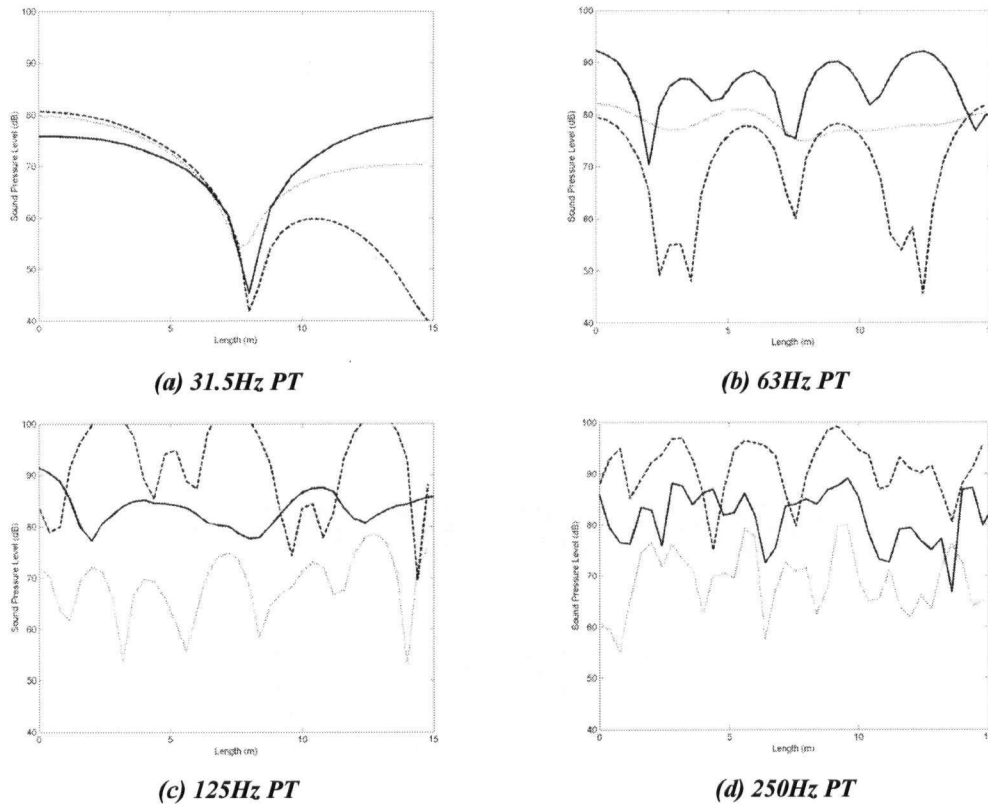


Figure 3.14 Measured and predicted sound pressure level along Line 2 in the scale model room. Solid line indicates measured, dashed is modal model, and dots is image-phase model.

3.4 Modeling the Fittings using Finite Elements

The author is not aware of any work that has been performed on modeling arrays of fittings in a room. Due to the size of the room and the fittings, the sound wavelength and computer processing power, it proved difficult to model the scale-model room with

high accuracy. Thus, unfortunately, due to time and computational limitations, the modeling of the fittings in the room was not performed. However, the investigation into the modeling of fittings in the hemi-anechoic chamber was pursued.

3.4.1 The Finite-Element Model

The FEMLAB finite-element package was used to develop a model of the hemi-anechoic room, with and without fittings. The Helmholtz equation was solved using the numerical finite-element technique. Initially, the source was modeled as a cylinder with rigid walls and one vibrating surface - emulating the speaker used in the measurements - and the room was rectangular and its surfaces fully absorbing, to model anechoic conditions as closely as possible. This proved to give erroneous results due to the unrealistic boundary conditions. Using a Neumann boundary condition such that the walls were fully absorptive, it was found that, if the energy incident from the source was not normal to the wall, the solution gave results indicative of a non-fully-absorbing wall. This was resolved by specifying the room as one-eighth of a sphere, with the source in the corner. Simplifying further, the source was also modeled as one-eighth of a sphere. With this geometry, the energy incident from the source was always normal to the walls, and the absorption occurred correctly, giving a good simulation of the anechoic chamber.

The room was one-eighth of a 34 m sphere, while the source was modeled as one-eighth sphere with a 0.5 m radius, and placed in the corner of the room. The fittings and

the floor were modeled as having infinite impedance surfaces, and the positions of the fittings were placed as close to the actual measurement orientations as possible. The outer walls of the sphere were fully absorbent, simulating a free-field condition.

For the predictions of the anechoic chamber, it was found that it was necessary to use on the order of 10^5 elements to produce meaningful results with the small fittings. Work by Maluski et al. [17, 18] on the transmission of sound between rooms using a finite-element model determined optimum mesh sizes and number of elements required for accurate results. It was expected that at least six elements per wavelength were required, but through validation with a scale model, element sizes of less than 1/6 of the wavelength were found to produce errors within 10%. That prediction, however, was for a simpler case with two empty rooms, and one flat panel wall. For predictions with fittings, with many small objects in the room and a much larger room volume, many more elements per wavelength were required to accurately model the enclosure and fittings.

3.4.2 Fitted Anechoic Fitted Room Results

The finite-element model was run at only 31.5 and 63 Hz, since higher frequencies required more elements per wavelength to achieve a reasonably accurate result and the memory capacity of the computer was insufficient to support such calculations.

The finite-element empty-room predictions were compared against measurement to ensure that the model was giving reasonable results. These are shown in Figures 3.15 and 3.16. At 31.5 Hz, the prediction and measured results match quite closely, with the same expected decay rate of 6 dB per doubling of distance. Across the width of the room - Lines 2 and 3 - the curves match well. At 63 Hz, there are some general trends and matching between the measured and predicted results. Line 1 shows a predicted result with more peaks and dips in the sound field than was measured. Lines 2 and 3 show similar differences between the predicted and measured sound pressure levels.

At 31.5 Hz, the finite element model gives results which match the measurements very well. At 63 Hz there is more of a difference between the two; however, the results are similar, and the predictions with fittings also match reasonably well, giving evidence that with more computing power, it would be possible to model the room and fittings with very good accuracy, and could be extended to predicting higher frequencies.

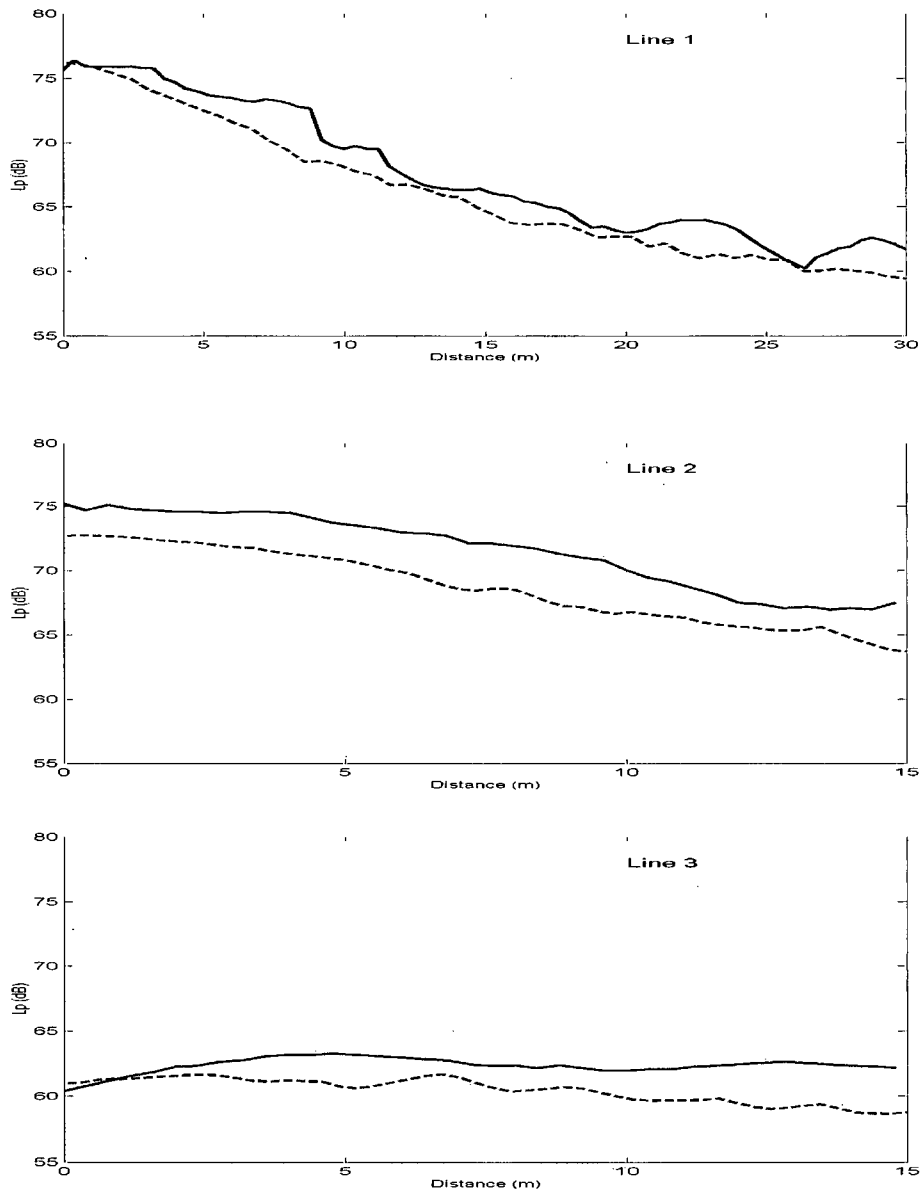


Figure 3.15. Comparison of the 31.5 HzFS hemi-anechoic chamber measurement (solid line) with the FEM prediction (dotted line) in the empty room.

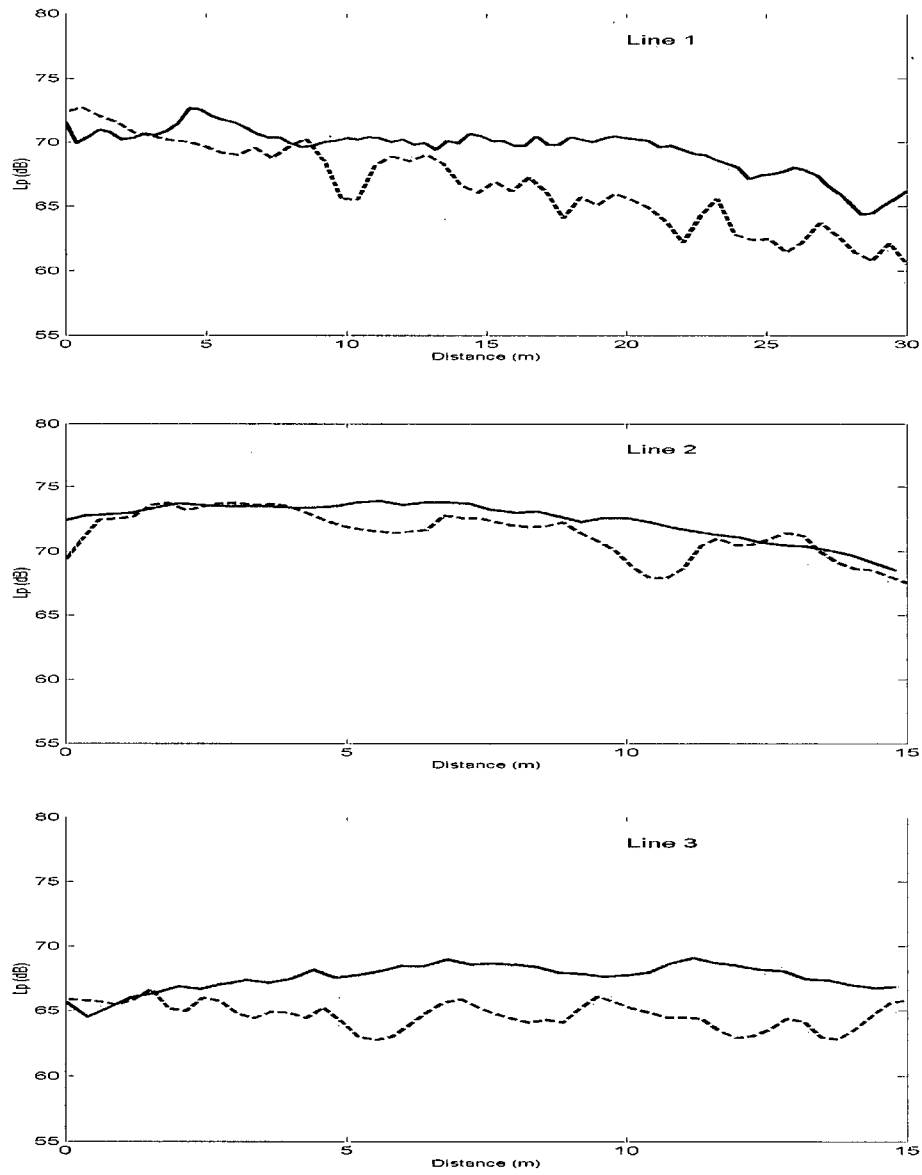


Figure 3.16. Comparison of the 63 HzFS hemi-anechoic chamber measurement (solid line) with the FEM prediction (dotted line) in the empty room.

The comparisons of predictions at 31.5 Hz with the hemi-anechoic room measurements are shown in Figures 3.17 and 3.18 for the small and large fittings cases. In the small fittings case, the decay with increasing distance from the source matches the measurement results. Both measurement and prediction show that the small fittings do not influence the sound field to a great extent in the predictions, as was found with the measurements. With the large fittings, however, along Line 1 the prediction results show a faster decay of the sound pressure level with distance than was measured. Moreover, some wave reflection and cancellation is predicted and shown by dips in the sound pressure level curves. Along Line 2, the prediction showed less decay than measurement; along Line 3, far from the source, the curves matched very well.

At 63 Hz with the small fittings, Figure 3.19, the curves generally do not match very well. Along Line 1, the finite-element model predicts more variation of the sound pressure level, while the measurement showed little effect of the small fittings. The finite-element model predicts a large dip in the sound pressure level in Line 2 at about the 12 m point. Along Line 3, there is little variation in sound pressure level predicted, as was measured. With the large fittings (Figure 3.20) very good agreement was found between the prediction and measurement. Along all three of the measurement lines, the contours match very well. The predictions with the larger fittings may have matched measurement better because of the fewer elements required to model the larger fittings. There are fewer large fittings; also, because they are larger, they require fewer (and larger)

elements to model. The small fittings, on the other hand, are greater in number, and also require smaller element sizes. The restriction on the total number of elements due to the memory limitation of the computer perhaps does not allow enough elements to calculate the sound field of a source outputting 63 Hz, or to account for the small fittings in the room.

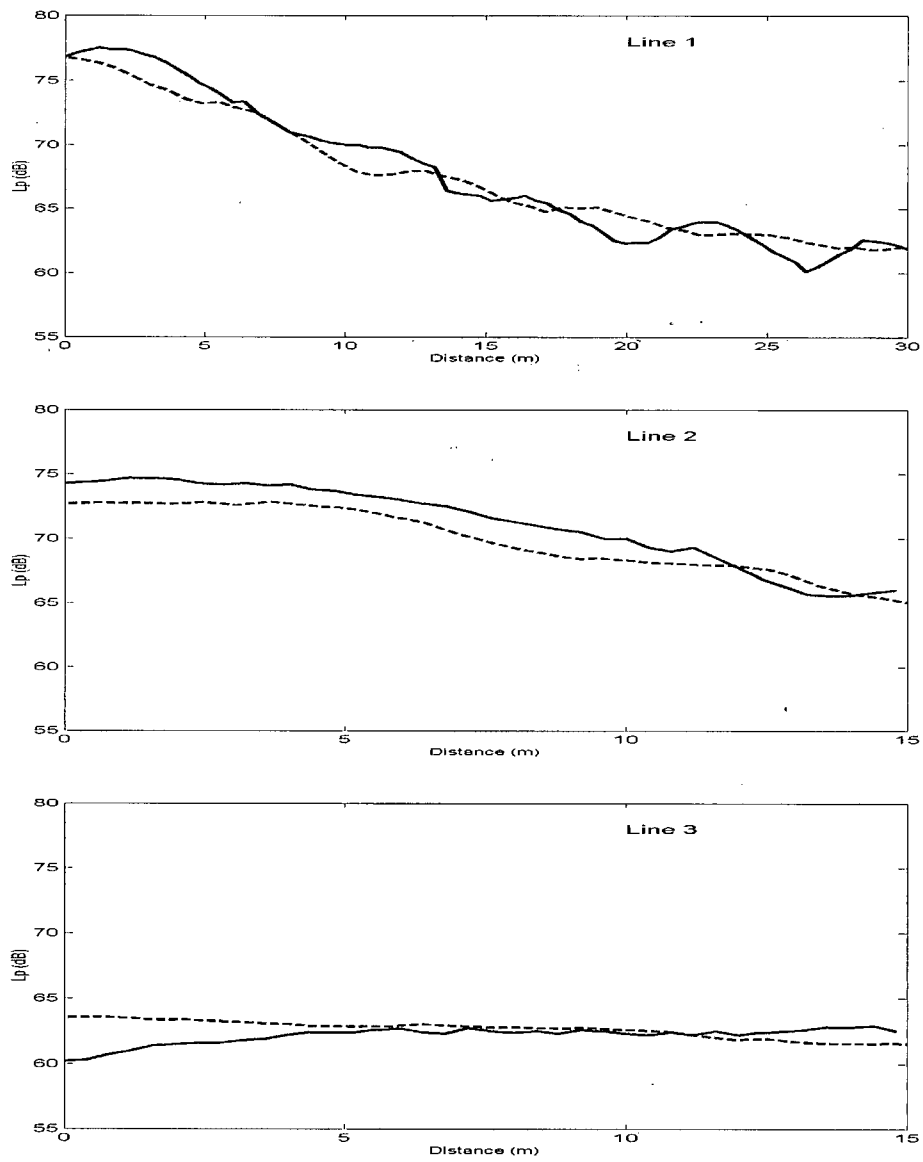


Figure 3.17. Comparison of the 31.5 Hz hemi-anechoic chamber measurement (solid line) with the FEM prediction (dotted line) with small fittings.

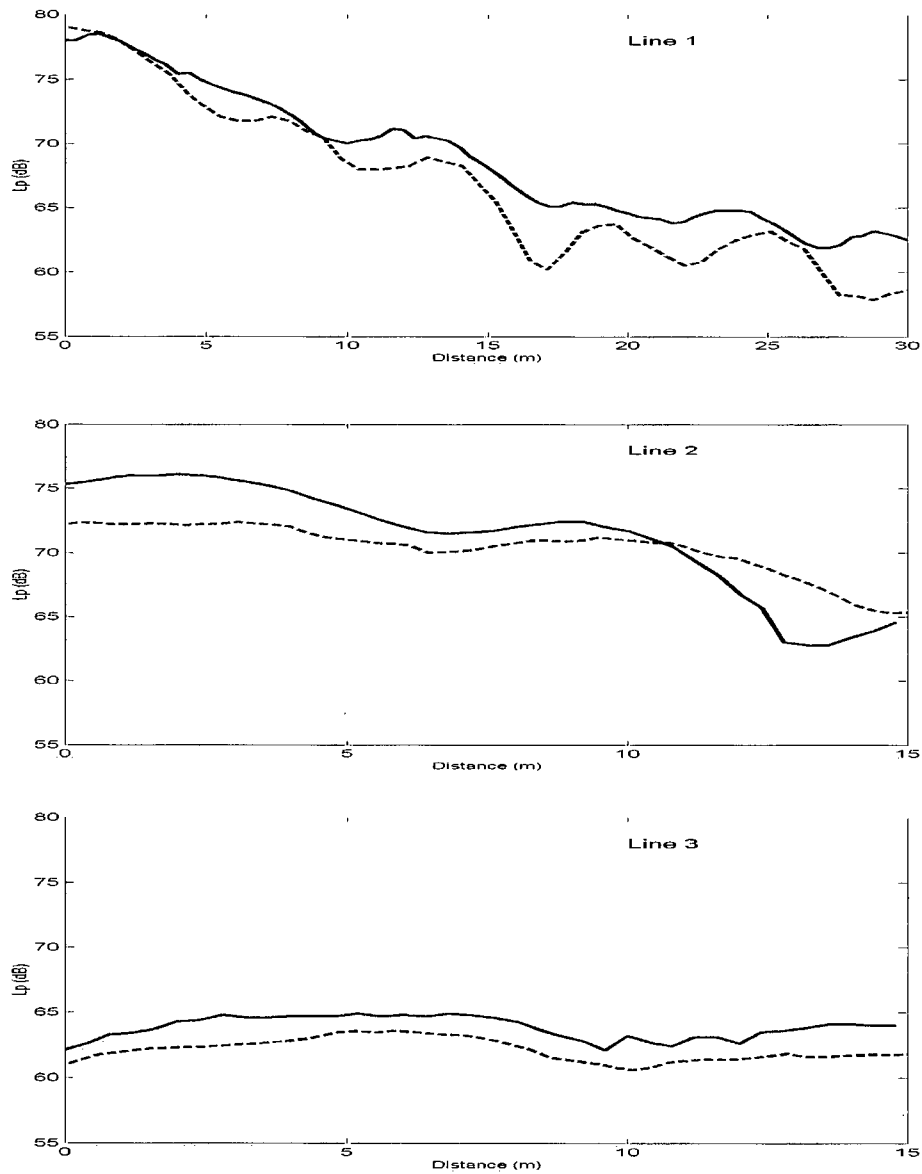


Figure 3.18. Comparison of the 31.5 Hz hemi-anechoic chamber measurement (solid line) with the FEM prediction (dotted line) with large fittings.

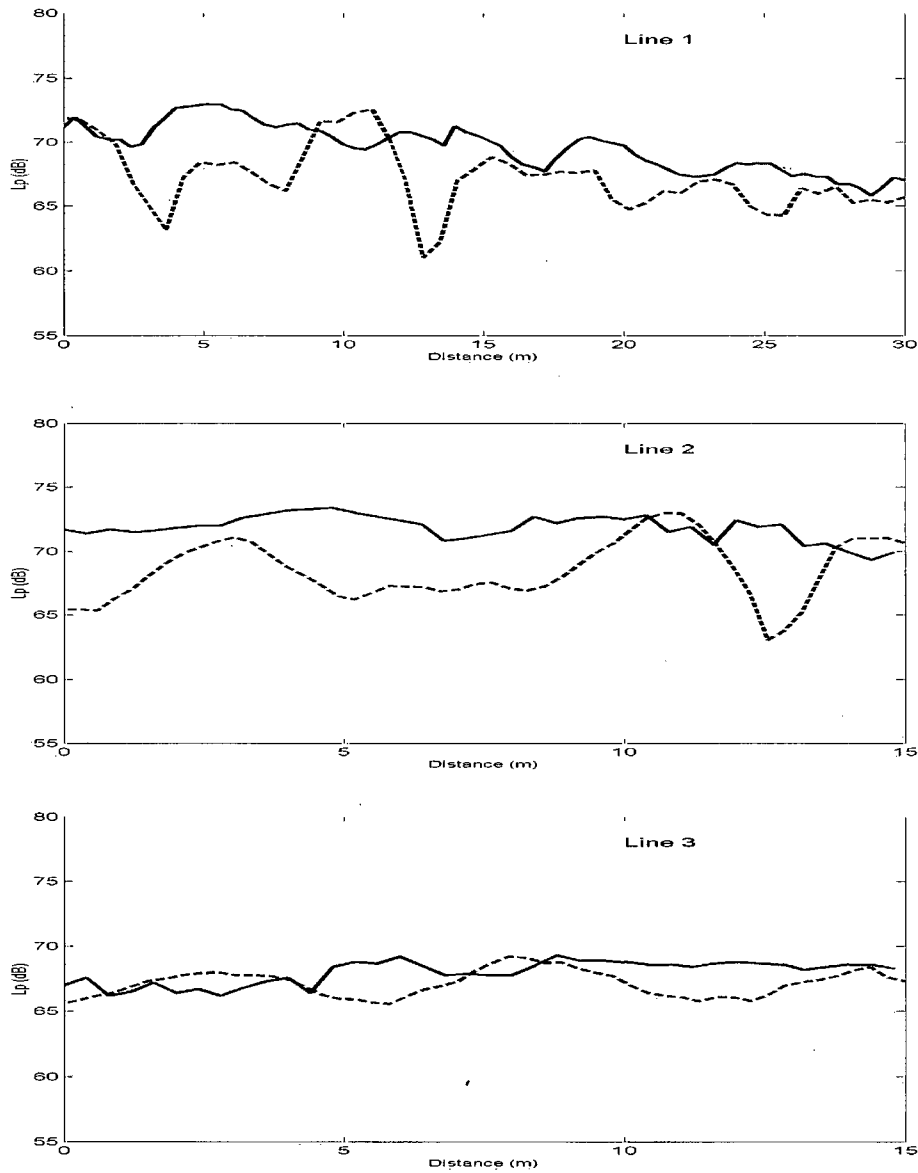


Figure 3.19. Comparison of the 63 Hz hemi-anechoic chamber measurement (solid line) with the FEM prediction (dotted line) with small fittings.

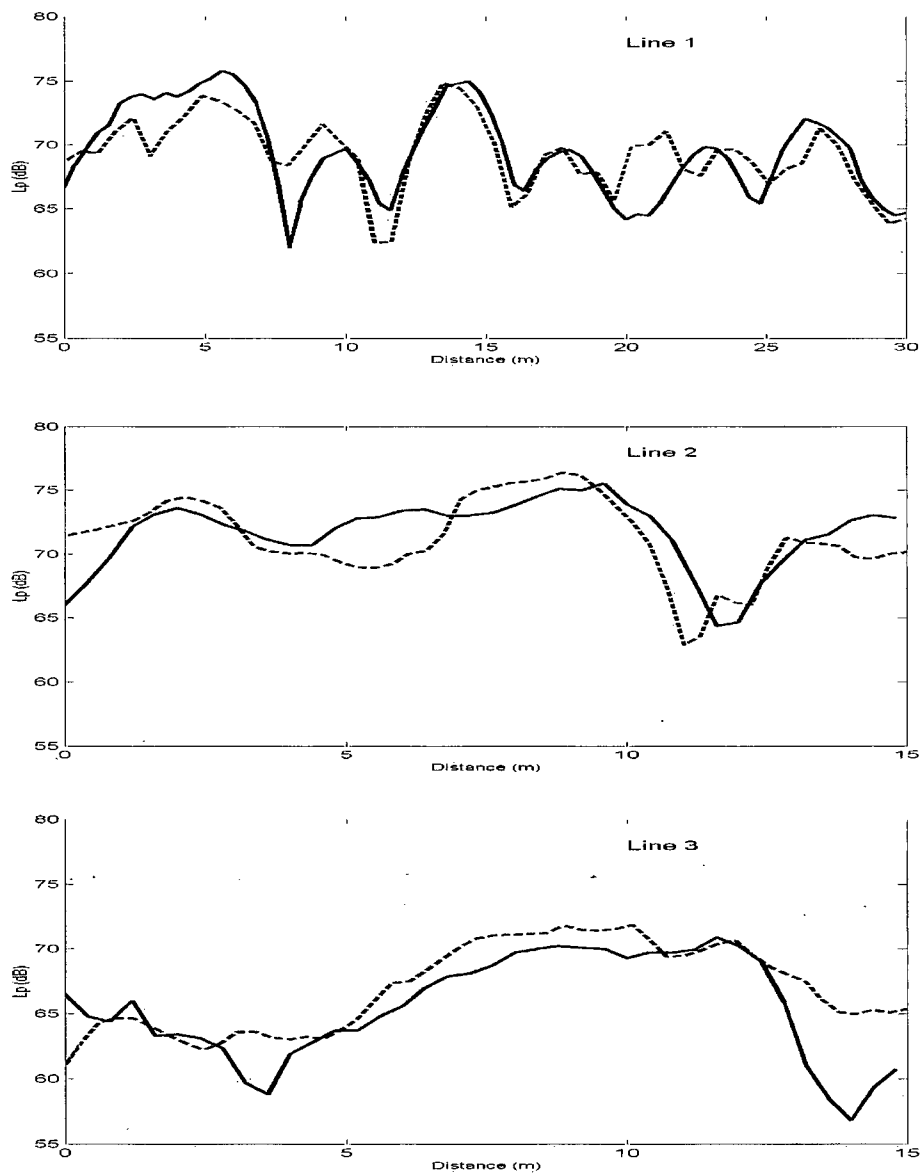


Figure 3.20. Comparison of the 63 Hz hemi-anechoic chamber measurement (solid line) with the FEM prediction (dotted line) with large fittings.

3.4.3 Summary

The finite element model was found to be able to model the sound field of a hemi-anechoic chamber under certain conditions. The limitations mainly depended on the amount of computational memory available to run the model with the number of elements needed for the size of room and source frequency of interest. At 31.5 Hz, the model was able to predict with reasonable accuracy the sound field of the three conditions - empty, small and large fitted rooms. At 63 Hz, the model was found to predict the empty and large fitted case well, but with the small fittings, was unable to give a reasonable result. With more computing power, the effects of the fittings in a hemi-anechoic chamber could be further investigated to a higher frequency, as well as with more varied sizes of fittings.

Chapter 4

Conclusion

4.1 Conclusions

The investigation into the characteristics and modeling of low-frequency sound in workrooms was performed in order to extend knowledge on low-frequency sound propagation and increase the effectiveness of determining methods to decrease the amount of low-frequency noise exposure of workers working in environments with high levels of low-frequency noise. This work was performed as an extension of previous work by Hodgson [7] on the characteristics of mid- and high-frequency noise propagation in workrooms, and also as part of work into the active control of low-frequency noise in rooms by Li [12].

A review of the literature on low-frequency wave propagation and boundary conditions was performed. It was found that the scattering of low-frequency sound by fittings is a complex process, with increasing complexity due to the arbitrary shapes of fittings that are commonly found in workrooms. This makes it very difficult to calculate directly the effects of the fittings on the sound field, especially if there are many such

fittings in the workroom. The boundaries also play a large role in the sound field, reflecting and absorbing the sound energy, and altering the sound field in the process. Methods for controlling low-frequency sounds are limited in effectiveness due to their long wavelengths and their diffraction properties. Active noise control is one method of controlling low-frequency noise that has shown some promise, but much work still has to be done in developing it for practical use. Methods to calculate or otherwise determine low-frequency sound fields will aid in finding ways to effectively decrease worker exposure to low-frequency noise, and its damaging effects.

Measurements were performed in a real workroom with and without fittings using a low-frequency sound source, to determine the effect of fittings on the propagation of low-frequency sound. The introduction of fittings in the room was found to have a profound effect on the sound field in the room. This was surprising given their small size relative to the sound wavelengths. With fittings, many more peaks and dips in the sound pressure level were measured in the room indicating that more wave interference effects were occurring. Also performed were measurements of the high-frequency sound propagation in the room; results were found to differ somewhat from previous work by Hodgson [7].

A scale model was utilized to make more detailed measurements of low-frequency sound fields in a more controllable environment. The measurements performed in the scale-model room showed that with pure-tone noise, small fittings

tended to smooth or decrease the variation in the sound pressure level with distance from the source; that is, they acted as diffusers. Large fittings generally increased the modal variation in the room.

Measurements of the fittings in a hemi-anechoic chamber were utilized to determine the effects of an array of fittings on the sound field, without the effect of the boundary walls. It was found that small fittings caused little change in the sound field and that large fittings caused some modal effects. In comparison with the measurements in the scale-model room, there is evidence that the small fittings do cause a change in the sound field, although it may be a complex process, in combination with changes due to the boundary walls.

Two prediction models, the image-phase model and the modal model, were used to model the sound field in the empty scale-model workroom. Some correlation between the measured and predicted sound fields was found. It was difficult to predict the scale-model room due to uncertainties in the determination of the boundary properties; wall vibration may have accounted for some of the anomalies found in measurement. The applicability of the models to real-world cases is highly dependent on the correct determination of the boundary conditions of the room, as this plays a large part in shaping the sound field in the workroom.

The finite-element prediction method was found useful to be able to model fittings, whereas the other two models tested were only able to model empty rooms. This

prediction method was found to model the effects of low-frequency sound very well, but higher frequencies were more difficult to model accurately. The main limitation to prediction was computer memory and processing power; at higher frequencies, the wavelength decreases, and thus many more elements are needed. Also, with the small fittings, smaller element sizes are required, which also increases the total number of elements required for modeling.

The work presented here provides a basis for the direction of the advancement of the control of low-frequency noise in workrooms in applications using both passive and active noise control methods. With further investigation and development of the models, passive control methods may be predicted and optimized for different situations of room and fittings configurations. The same may be performed with active control, with better optimization of control sources and error microphones.

4.2 Future Work

This work has succeeded in elucidating some of the effects of low-frequency sound in workrooms, and developing and investigating models for use in modeling the low-frequency sound field in workrooms. Further investigations could include measurements of more real workrooms to further verify the low-frequency effects measured in this study. A comprehensive study or review of the low-frequency output of

typical sources used in workrooms should also be performed, in order to characterize and understand better the radiation of low-frequency noise from these sources.

The prediction of empty rooms was studied, assuming the boundary conditions were homogeneous. Workrooms inherently contain many different bounding surfaces, such as concrete walls, large equipment doors, and windows. These various surfaces should be considered in the modeling.

Fittings were modeled in a hemi-anechoic chamber using the finite-element method. The main limitations related to with computer memory and processing limits; thus methods of optimizing the numerical calculations such that modeling higher frequencies is possible, should be pursued. Due to time limitations, predictions of the scale-model room were not performed with the finite-element model. Future work could also use the finite-element method to perform predictions in empty and fitted rooms.

Bibliography

- [1] International Standards Organization (ISO) Standard 228:1997 (E) Annex A, Graphical illustration of equal-loudness level contours and minimum audible field (MAF) for pure tones under free-field listening conditions.
- [2] W. Tempest. *Infrasound and Low Frequency Vibration*. Academic Press, 1976.
- [3] Mills, J.H., et al. Temporary Threshold Shifts Produced by Exposure to Low-Frequency Noises. *J. Acoust. Soc. Am.* 73(3), 1983.
- [4] Burdick, C.K., et al. Threshold Shifts in Chinchillas Exposed to Octave Bands of Noise Centered at 63 and 1000 Hz for Three Days. *J. Acoust. Soc. Am.* 64(2), 1978.
- [5] Birgitta Berglund and Peter Hassmen. Sources and Effects of Low-Frequency Noise. *J. Acoust. Soc. Am.* 99(5), 1996.
- [6] Murray Hodgson. Measurements of the Influence of Fittings and Roof Pitch on the Sound Field in Panel-Roof Factories. *Applied Acoustics*. 16, 1983.
- [7] Murray Hodgson. On the Accuracy of Models for Predicting Sound Propagation in Fitted Rooms. *J. Acoust. Soc. Am.* 88(2), 1990.
- [8] P. M. Morse and K.U. Ingard. *Theoretical Acoustics*. Princeton University Press, 1968.
- [9] Heinrich Kuttruff. *Room Acoustics*. Applied Science Publishers Ltd., 1976.
- [10] Jon B. Allen and David A. Berkley. Image Method for Efficiently Simulating Small-Room Acoustics. *J. Acoust. Soc. Am.* 65(4), 1979.

-
- [11] Jingnan Guo and Murray Hodgson. Investigation of Active Noise Control in Non-Diffuse Sound Fields. ACTIVE 99 Conference Proceedings, 1999.
- [12] Desheng Li and Murray Hodgson. Active Noise Control in Non-Diffuse Three-Dimensional Enclosures with High Modal Density: Theoretical Studies. Canadian Acoustical Association 2003 Conference Proceedings, Sept. 2003.
- [13] Desheng Li and Murray Hodgson. Active Noise Control in Non-Diffuse Three-Dimensional Enclosures with High Modal Density: Experimental Studies. Canadian Acoustical Association 2003 Conference Proceedings, Sept. 2003.
- [14] M. R. Hodgson and R. J. Orłowski. Acoustic Scale Modeling of Factories, Part I: Principles, Instrumentation and Techniques. *Journal of Sound and Vibration*. 113(1), 1987.
- [15] American National Standards Institute. Method for the Calculation of the Absorption of Sound by the Atmosphere, ANSI S1.26 1978.
- [16] P.A. Nelson and S.J. Elliott. *Active Control of Sound*. Academic Press, 1992.
- [17] Maluski, Sophie P.S. and Gibbs, Barry M. Application of a Finite-Element Model to Low-Frequency Sound Insulation in Dwellings. *J. Acoust. Soc. Am.* 108(4), 2000.
- [18] Maluski, Sophie, and Bougdah, Hocine. Predicted and Measured Low-Frequency Response of Small Rooms. *Journal of Building Acoustics*. 4(2), 1997.
- [19] B. Brouard, D. Lafarge and J.-F. Allard. A General method of Modeling Sound Propagation in Layered Media. *Journal of Sound and Vibration*. 183(1), 1995.
- [20] Wareing, Andrew. Acoustical Modeling of Rooms with Extended-Reaction Surfaces. M.A.Sc. Thesis, 2003.

Appendix A

Source Characterization

A.1 Low-frequency source

The low-frequency source consisted of two 380 mm low-frequency speaker drivers mounted on opposite sides of a sealed 460 mm cubic wooden box (see Figure A1).

Both speakers were driven in phase.

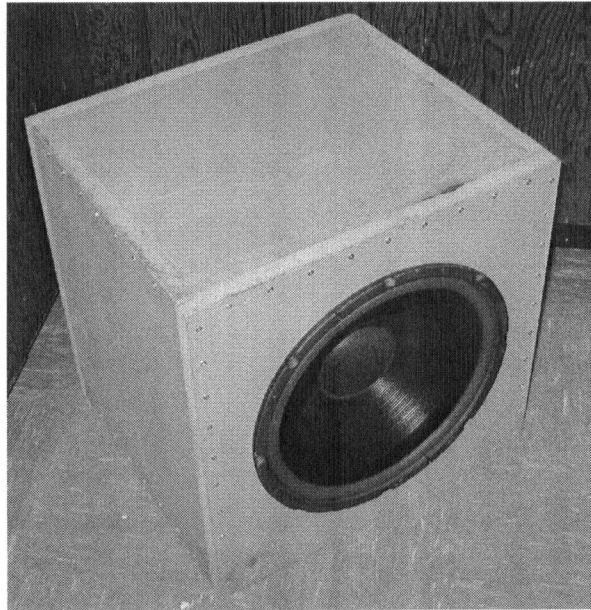


Figure A1 The low-frequency source.

The frequency response and horizontal-plane directivity of the low-frequency source were measured in the anechoic chamber. Figure A2 shows the frequency response of the source, measured using the MLSSA system.

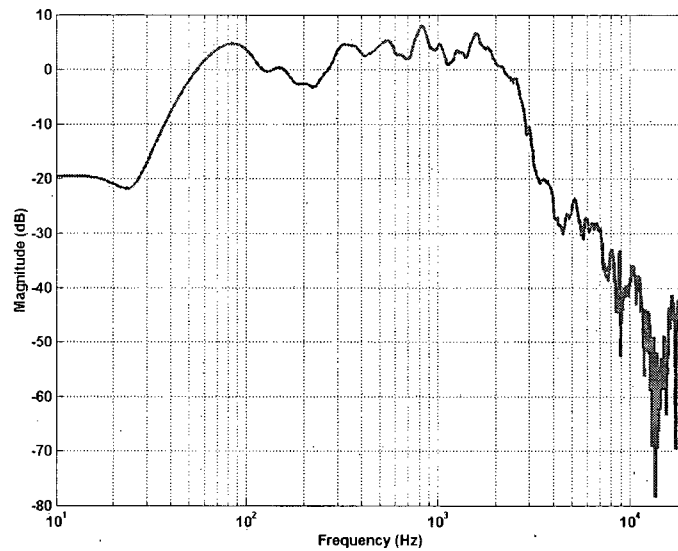


Figure A2 Frequency response of the low-frequency source, as measured at 1m, using MLSSA.

The source generates sound over the range 20 to 3000 Hz, and has a fairly flat response from between 50 to 2500 Hz. Figures A3 to A5 show the directivity of the low-frequency source using a 63 Hz pure tone, and 31.5 and 63 Hz octave-band-filtered noise, respectively. The loudspeaker was measured with the microphone at 1m in front of the loudspeaker (the 0° direction in the figures).

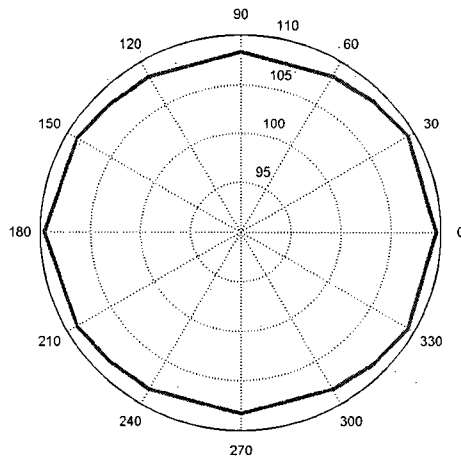


Figure A3 Directivity of the low-frequency source with a 63Hz pure tone output.

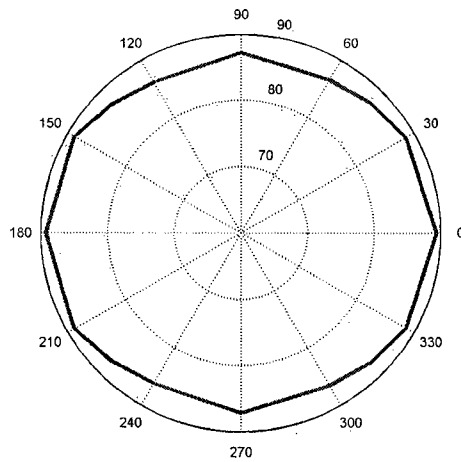


Figure A4 Directivity of the low-frequency source with a 31.5 Hz Octave Band filtered noise.

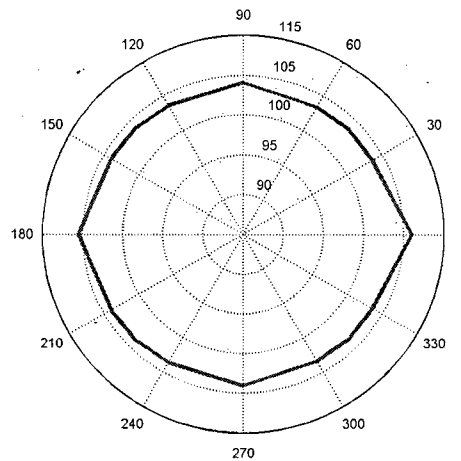


Figure A5 Directivity of the low-frequency source with a 63 Hz Octave Band filtered noise signal.

The source radiates most strongly on the main axes of the driver units. The speaker shows relatively uniform response as a function of angle, varying less than 5dB at the sides relative to in front.

A.2 Scale Model Source

A small 4 in. speaker driver was built into a small box for use as the source in the scale-model and anechoic-chamber experiments. The frequency response of the driver

and box are shown in Figure A6 below, measured with MLSSA. The frequencies used in the scale model were 250, 500, 1000 and 2000 Hz; their full-scale equivalent frequencies are 31.5, 63, 125 and 250 Hz. The source has decent output from about 250 Hz to 4000 Hz. A peak occurs at 800 Hz, and there is a large dip in the frequency response at about 1500 Hz. This may affect the octave-band noise outputs (most notably the 1000 Hz octave-band), where some frequencies within the octave-band will be emphasized over others. The measurements in the scale model room did not show any unexpected response variations in the 1000 Hz (125 HzFS) octave band, compared to the other frequencies used.

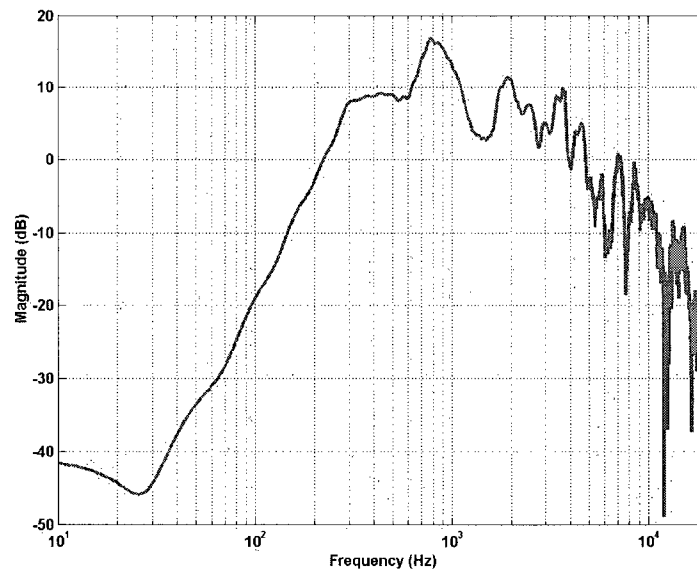


Figure A6 Frequency response of the scale model source, measured using MLSSA

Figure A7 and A8 show the horizontal-plane directivities measured with pure tones and octave-band noise, respectively. At 31.5 HzFS pure tone, the source outputs about 3 dB higher in front of the speaker, than behind. At 250 Hz, the directivity is increased, being 13 dB higher in front. With the octave-band noise, a similar trend is found, with only 3 dB difference between the front and rear of the source at 31.5 Hz, and 13 dB difference at 250 Hz.

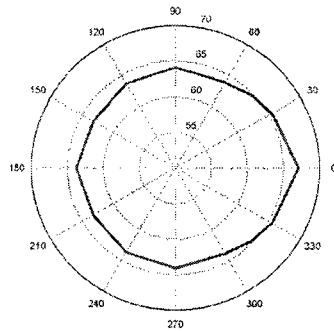
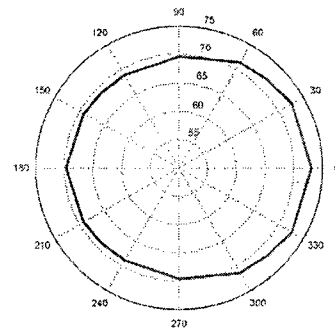
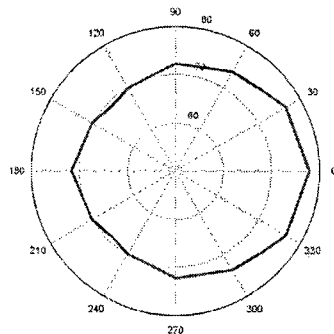
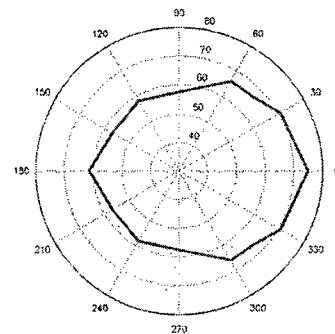
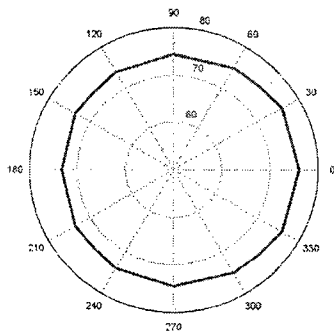
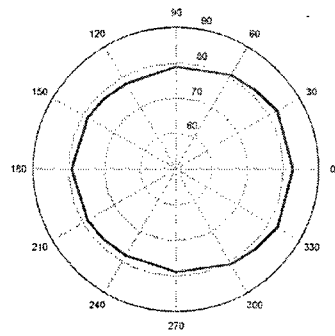
**31.5 Hz PT****63 Hz PT****125 Hz PT****250 Hz PT**

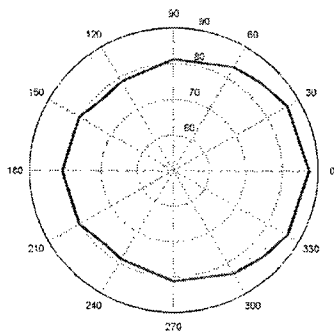
Figure A7 Directivity of the scale model source, measured using pure tones.



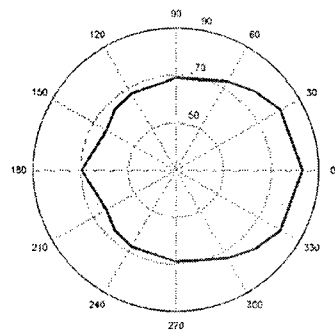
31.5 HzOB



63 HzOB



125 HzOB



250 HzOB

Figure A8 Directivity of the scale model source, measured with octave-band noise.

Appendix B

Green's Function Solution for the Helmholtz Equation

The analysis that follows derives from the treatment in Nelson and Elliott [21], with a modification in the calculation to consider a volume-velocity point source, and not a distribution of volume sources within the enclosure, nor excitation by the surfaces of the enclosure.

In solving for the inhomogeneous Helmholtz equation with boundary conditions, the Green's function is useful. In particular, the Green's function for the inhomogeneous Helmholtz equation is,

$$(\nabla^2 + k^2)G(x|y) = -\delta(x-y), \quad [\text{B-1}]$$

where $G(x|y)$ is the Green's function, which quantifies the spatial dependence of the complex pressure field produced by a point source at position y . To satisfy the rigid-walled boundary condition, $\nabla G(x|y) \cdot n = 0$, such that,

$$G(x|y) = \sum_{m=0}^{\infty} b_m \psi_m(x), \quad [\text{B-2}]$$

where the b_m are arbitrary complex coefficients to be found. Thus, with substitution into Eq. (A-1),

$$\sum_{m=0}^{\infty} b_m (k^2 - k_m^2) \psi_m(x) = -\delta(x - y). \quad [\text{B-3}]$$

Using the properties of the Dirac delta function, Green's function is found,

$$G(x|y) = \sum_{n=0}^{\infty} \frac{\psi_n(x)\psi_n(y)}{V(k_n^2 - k^2)}. \quad [\text{B-4}]$$

Ultimately, the following equation is to be solved,

$$\nabla_y^2 p(y) + k^2 p(y) = -Q_{vol}(y), \quad [\text{B-5}]$$

which is the Helmholtz equation, where $p(y)$ is the pressure field due to a volume velocity source $Q_{vol}(y)$. If we multiply Eq. (A-5) by $G(x|y)$, subtract it from Eq. (A-1) multiplied by $p(y)$, we get the following,

$$G(y|x)\nabla_y^2 p(y) - p(y)\nabla_y^2 G(y|x) = -Q_{vol}(y)G(y|x) + p(y)\delta(y-x). \quad [\text{B-6}]$$

Integration of both sides of the equation over the volume of the enclosure gives,

$$\int_V [G(y|x)\nabla_y^2 p(y) - p(y)\nabla_y^2 G(y|x)] dV + \int_V Q_{vol}(y)G(y|x) dV = p(x), \quad [\text{B-7}]$$

for x within V . Using Green's theorem, the first integral can be changed and by reciprocity $G(y|x) = G(x|y)$ such that we get,

$$p(x) = \int_S G(x|y)\nabla p(y) \cdot ndS + \int_S p(y)\nabla G(x|y) \cdot ndS + \int_V Q_{vol}(y)G(x|y) dV. \quad [\text{B-8}]$$

Since there will be no contribution to the sound field from vibration of the walls, the gradient, $\nabla G(x|y) \cdot n = 0$, and the second integral equals zero,

$$p(x) = \int_S G(x|y) \nabla p(y) \cdot n dS + \int_V Q_{vol}(y) G(x|y) dV, \quad [\text{B-9}]$$

If we have finite-impedance surfaces for the walls, then we can express the particle velocity in terms of the derivative of the complex pressure with respect to the direction normal to the wall. Using this with the assumption of a harmonic wave source, we get,

$$\nabla p(y) \cdot n = -j\omega\rho_0 u(y). \quad [\text{B-10}]$$

In terms of the normalized specific acoustic admittance, Eq. (3.8) above, then,

$$\nabla p(y) \cdot n = -jk\beta(y)p(y). \quad [\text{B-11}]$$

Substituting Eq. (A-11) for the wall impedance into Eq. (A-9), we get,

$$p(x) = \int_V Q_{vol}(y) G(x|y) dV - \int_S jk\beta(y) p(y) G(x|y) dS. \quad [\text{B-12}]$$

With $G(x|y)$ as in Eq. (A-4),

$$p(x) = \int_V Q_{vol}(y) \sum_{n=0}^{\infty} \frac{\psi_n(x)\psi_n(y)}{V(k_n^2 - k^2)} dV - \int_S jk\beta(y) p(y) \sum_{n=0}^{\infty} \frac{\psi_n(x)\psi_n(y)}{V(k_n^2 - k^2)} dS, \quad [\text{B-13}]$$

Letting $p(y) = \sum_{m=0}^{\infty} a_m \psi_m(y)$ and rearranging,

$$p(x) = \sum_{n=0}^{\infty} \psi_n(x) \left[\frac{1}{(k_n^2 - k^2)} \left\{ \frac{1}{V} \int_V Q_{vol}(y) \psi_n(y) dV - jk \sum_{m=0}^{\infty} a_m D_{nm} \right\} \right], \quad [\text{B-14}]$$

$$\text{with } D_{nm} = \frac{1}{V} \int_S \beta(y) \psi_n(y) \psi_m(y) dS.$$

When n is not equal to m , the value of D_{nm} is small and may be ignored. Also, $D_{nm} = 0$ if $\beta(y)$ is uniform over each wall and any two corresponding modal integers are dissimilar in n and m . Thus the equation for $p(x)$ becomes,

$$p(x) = \sum_{n=0}^{\infty} \psi_n(x) \left[\frac{1}{(k_n^2 - k^2)} \left\{ \frac{1}{V} \int_V Q_{vol}(y) \psi_n(y) dV - jka_n D_{nn} \right\} \right], \quad [\text{B-15}]$$

Simplifying the equation and letting the source term $Q_{vol}(y)$ be rewritten in terms of a distribution of volume sources, $Q_{vol}(y) = j\omega\rho_o q_{vol}(y)$, we get,

$$p(x) = \sum_{n=0}^{\infty} \frac{\omega\rho_o c_o^2 \psi_n(x)}{V(\omega c_o D_{nn} - j(\omega^2 - \omega_n^2))} \int_V j\omega\rho_o q_{vol}(y) \psi_n(y) dV. \quad [\text{B-16}]$$

Letting the source be a point source, $q_{vol}(y) = q_s \delta(y - y_s)$, we get

$$p(x) = \sum_{n=0}^{\infty} \frac{j\omega\rho_o c_o^2 \psi_n(x)}{V[\omega c_o D_{nn} - j(\omega^2 - \omega_n^2)]} q_s \psi_n(y_s). \quad [\text{B-17}]$$

Appendix C

Transfer Matrix Impedance Calculation

In order to determine the surface impedance of the different enclosures measured in this work, the transfer matrix method of calculation using the properties of the boundary materials was used. Full details of the equations used and the method of calculation can be found in Allard [17] and UBC Mechanical Engineering Andrew Wareing's M.A.Sc. thesis [19].

The velocity and stress components of an elastic-solid material, expressed as a vector, from the incident side of the material (N_1) through to the transmitted side (N_2) can be related through a transfer matrix, T,

$$V(N_1) = T \cdot V(N_2). \quad [\text{C-1}]$$

The deformations in an elastic-solid material can be quantified in terms of scalar and vector potentials:

$$\vec{u} = \nabla\phi + \nabla \times \psi, \quad [\text{C-2}]$$

where $\nabla\phi$ and $\nabla \times \psi$ represent the compressional and shear waves in the elastic-solid medium.

$$\nabla^2 \varphi = \frac{\rho}{\lambda + 2\mu} \frac{\partial^2 \varphi}{\partial t^2}, \quad [\text{C-3}]$$

$$\nabla^2 \psi = \frac{\rho}{\mu} \frac{\partial^2 \psi}{\partial t^2}, \quad [\text{C-4}]$$

$$\rho \frac{\partial^2 u_i}{\partial t^2} = (\lambda + \mu) \frac{\partial \theta}{\partial x_i} + \mu \nabla^2 u_i + B_i, \text{ where } i = 1, 2, 3. \quad [\text{C-5}]$$

where ρ is the density of the medium, and λ and μ are the Lamé coefficients, dependent on Poisson's ratio and the Young's modulus of the medium.. The system of equations to be solved represents the four unknowns of the system, namely the normal and tangential velocity components, and the normal and shear stress components.

$$\begin{Bmatrix} v_1(N_1) \\ v_3(N_1) \\ \sigma_{33}(N_1) \\ \sigma_{13}(N_1) \end{Bmatrix} = T_s \cdot \begin{Bmatrix} v_1(N_2) \\ v_3(N_2) \\ \sigma_{33}(N_2) \\ \sigma_{13}(N_2) \end{Bmatrix}, \quad [\text{C-6}]$$

where T_s is the transfer matrix:

$$\Gamma^s(x_3) = \begin{bmatrix} \omega k_l \cos(k_{p3} x_3) & -j \omega k_l \sin(k_{p3} x_3) & j \omega k_{s3} \sin(k_{s3} x_3) & -\omega k_{s3} \cos(k_{s3} x_3) \\ -j \omega k_{p3} \sin(k_{p3} x_3) & \omega k_{p3} \cos(k_{p3} x_3) & \omega k_l \cos(k_{s3} x_3) & -j \omega k_l \sin(k_{s3} x_3) \\ -D_1 \cos(k_{p3} x_3) & j D_1 \sin(k_{p3} x_3) & 2j N k_1 k_{s3} \sin(k_{s3} x_3) & -2N k_1 k_{s3} \cos(k_{s3} x_3) \\ 2j N k_1 k_{p3} \sin(k_{p3} x_3) & -2N k_1 k_{p3} \cos(k_{p3} x_3) & N(k_{s3}^2 - k_l^2) \cos(k_{s3} x_3) & -j N(k_{s3}^2 - k_l^2) \sin(k_{s3} x_3) \end{bmatrix} \quad [\text{C-7}]$$

$$k_i = \frac{\omega}{c} \sin(\theta)$$

$$k_{p3} = \sqrt{k_p^2 - k_i^2} \quad \text{and} \quad k_{s3} = \sqrt{k_s^2 - k_i^2}$$

$$k_p = \frac{\omega}{c_p} \quad \text{and} \quad k_s = \frac{\omega}{c_s}$$

$$c_p = \sqrt{\frac{\lambda + 2\mu}{\rho}} \quad \text{the compressional wave speed in an elastic-solid}$$

$$c_s = \sqrt{\frac{\mu}{\rho}} \quad \text{the shear wave speed in an elastic-solid}$$

$$D_1 = \lambda(k_{p3}^2 + k_i^2) + 2\mu k_{p3}^2$$

$$\lambda = \frac{\nu E}{(1+\nu)(1-2\nu)}$$

$$\mu = \frac{E}{2(1+\nu)}$$

for Young's modulus E , and Poisson ratio ν

$\sigma_{ij} = \lambda\theta\delta_{ij} + 2\mu e_{ij}$ gives the stress-strain relationship for isotropic elastic media

$\theta = e_{11} + e_{22} + e_{33}$ is the volumetric strain

$$\delta_{ij} = \begin{cases} 1 & \text{if } i = j \\ 0 & \text{if } i \neq j \end{cases}$$

$$e_{ij} = \frac{1}{2} \left(\frac{\partial u_i}{\partial x_j} + \frac{\partial u_j}{\partial x_i} \right), \text{ strain tensor}$$

Appendix D

Pictures at X- Positions



Figure D1 Position X1.



Figure D2 Position X2.

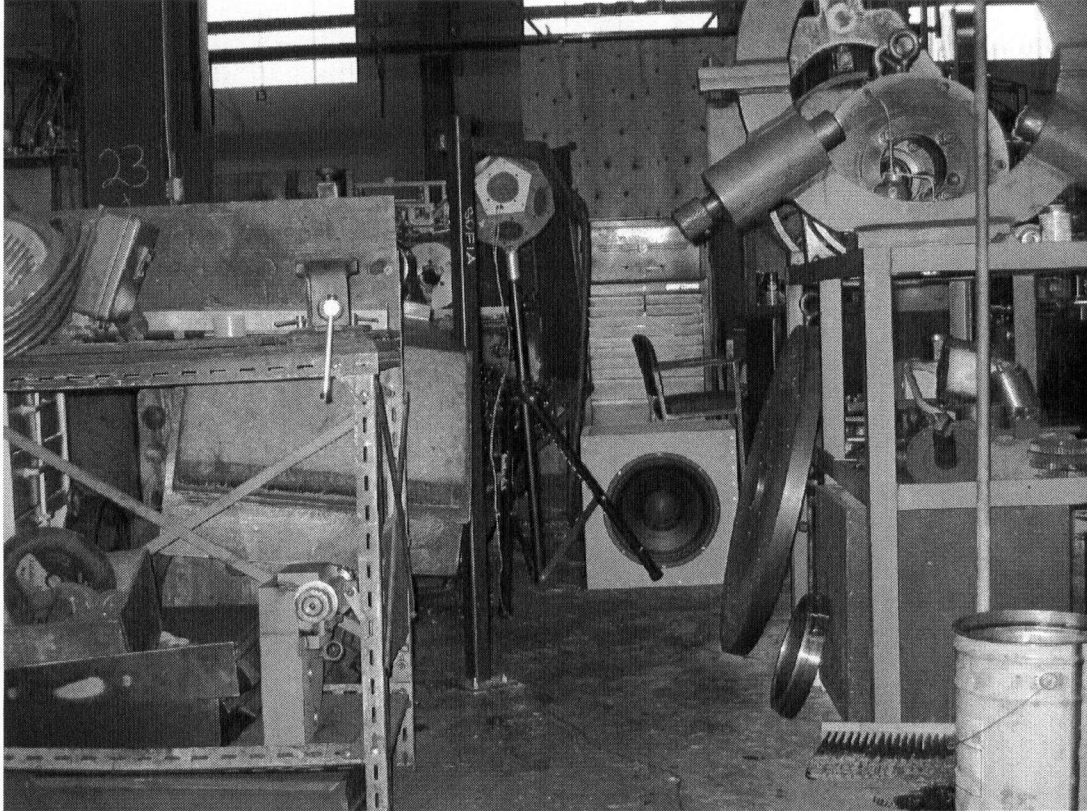


Figure D3 Position X3.

Appendix E

Matlab Code

```
% Eigenvalues.m
% Galen Wong 2004
%
% Calculates the eigenvalues of a given room, giving the mode numbers and
% natural frequencies of the room.
%
% Lx, Ly, Lz = Room dimensions [m]
% N = Number of modes to calculate in each dimension

% Variables

Lx = 30.16; Ly = 15.12; Lz = 7.52; % Dimensions of the room [m]
N = 100; % Number of modes to calculate

% Constants

co = 343; % Speed of air [m/s]

% Calculating all the eigenvalues for the room

d = 0 : N;
e = 0 : N;
f = 0 : N;
fx2 = (d.*(co/(2*Lx))).^2;
fy2 = (e.*(co/(2*Ly))).^2;
fz2 = (f.*(co/(2*Lz))).^2;
freq = null(1);
for l = 1 : length(d)
    for m = 1 : length(e)
        for n = 1 : length(f)
            wave(l, m, n) = sqrt( fx2(l) + fy2(m) + fz2(n) );
```

```
        freq = [freq; [l-1, m-1, n-1, wave(l, m, n)]];
    end
end
end

sortedF = sortrows(freq, 4);

save('SM_RealDimensions.mat', 'sortedF', 'Lx', 'Ly', 'Lz', '-MAT');
```

```
% SM_Script.m
% Input values for running modal.m

clear all;

beta = {1./[(4.1500e+002+1.4453e+003i)*ones(1,4), 999999, 4.1500e+002
+1.8210e+002i];
1./[(4.1500e+002 +2.8906e+003i)*ones(1,4), 999999, 4.1500e+002
+3.6416e+002i];
1./[(4.1500e+002 +5.7354e+003i)*ones(1,4), 999999, 4.1500e+002
+7.2256e+002i];
1./[(4.1501e+002 +1.1471e+004i)*ones(1,4), 999999, 4.1500e+002
+1.4451e+003i]; };

fs = [31.5, 63, 125, 250];
Lw = 80;
Lq = [0.2, 0.2, 0.2];
Height = 0.5;
delta = 0.2;
Nstart = 1;
Nend = 50000;
MatName = 'sortedF_val3.mat';

for i = 1:length(beta);
    [x, y, p, pressure] = Modal(fs(i), Lw, Lq, beta{i}, Height, delta, Nstart, Nend,
    MatName);
    Freq = num2str(fs(i));
    beta_i = num2str(beta{i});
end
```

```
% Modal Prediction Model
% Galen Wong 2004
%
% This program calculates the sound field at a specified height in a rectangular
room
% due to the contributions of the modes excited by a point source.
%
% Inputs
%
% fs = Source excitation frequency [Hz]
% Lw = Source power level [dB]
% Lq = Position of the source [Lqx Lqy Lqz] [m]
% beta = Complex wall impedance of the walls at [x0 xL y0 yL z0 zL]
% delta = Resolution [m]
% Nstart, Nend = Calculate the contribution of modes from the list of eigenvalues
in
% sortedF.mat created by Eigenvalues.m
% Height = Height of the receiver [m]
%
% Lx, Ly, Lz = Room dimensions [m] are retrieved from the .mat eigenvalues file

function [Xaxis, Yaxis, P_dB, P] = Modal(fs, Lw, Lq, beta, Height, delta, Nstart,
Nend, MatName)

Po = 2e-5; % Reference Pressure [Pa]
po = 1.210; % Density of air [kg/m^3]
co = 344; % Speed of air [m/s]

%
% Main program
%

load(MatName) % Loading up precalculated eigenfrequencies of the room

% Calculating Volume and Surface Area of the room;
Vol = Lx*Ly*Lz;
SurfX = Lx*Lz;
SurfY = Ly*Lx;
SurfZ = Lz*Ly;
```

```
SurfTot = 2*(SurfX + SurfY + SurfZ);
```

```
w = 2 * pi * fs; % Changing the frequency into radians
```

```
kw = w / co; % Wavenumber of the driving frequency
```

```
Xaxis = 0 : delta : Lx;
```

```
Yaxis = 0 : delta : Ly;
```

```
Zaxis = 0 : delta : Lz;
```

```
W = 10.^(Lw/10 - 12); % Power of the source
```

```
q = sqrt( (W * 8 * pi * co) / (w * w * po) ); % Volume velocity of the point source
```

```
% Main calculation
```

```
% Initialization
```

```
P = 0;
```

```
syms x y z
```

```
% For each mode N from the list, calculate its contribution to the total pressure level
```

```
for m = Nstart : Nend
```

```
    n1 = sortedF(m,1); n2 = sortedF(m,2); n3 = sortedF(m,3);
```

```
    kx = n1 * (pi/Lx); ky = n2 * (pi/Ly); kz = n3 * (pi/Lz);
```

```
    wn = sortedF(m,4)*2*pi;
```

```
    if sortedF(m,1) == 0 e1 = 1; else e1 = 2; end
```

```
    if sortedF(m,2) == 0 e2 = 1; else e2 = 2; end
```

```
    if sortedF(m,3) == 0 e3 = 1; else e3 = 2; end
```

```
    ei = sqrt(e1 * e2 * e3);
```

```
    % PsiX
```

```
    PsiX_x = cos(Xaxis * kx);
```

```
    PsiX_y = cos(Yaxis * ky);
```

```
    PsiX_Height = cos(Height * kz);
```

```
    PsiX = ei * PsiX_Height * PsiX_y * PsiX_x;
```

```
    Dnn
```

```

if kx == 0 SurX = Lx/2; else SurX = (cos(kx * Lx) * sin(kx * Lx) + kx*Lx)/(2*kx);
end
if ky == 0 SurY = Ly/2; else SurY = (cos(ky * Ly) * sin(ky * Ly) + ky*Ly)/(2*ky);
end
if kz == 0 SurZ = Lz/2; else SurZ = (cos(kz * Lz) * sin(kz * Lz) + kz*Lz)/(2*kz); end

% Calculate the effect of the surface impedance on the modes
Sur_x0 = beta(1) * SurY * SurZ; % * cos(kx*0)
Sur_xL = beta(2) * cos(kx*Lx) * SurY * SurZ;
Sur_y0 = beta(3) * SurX * SurZ; % * cos(ky*0)
Sur_yL = beta(4) * cos(ky*Ly) * SurX * SurZ;
Sur_z0 = beta(5) * SurX * SurY; % * cos(kz*0)
Sur_zL = beta(6) * cos(kz*Lz) * SurX * SurY;

Dnn = double((1/Vol) * ei * ei * (Sur_x0 + Sur_xL + Sur_y0 + Sur_yL + Sur_z0
+ Sur_zL));

% PsiY

PsiY(m) = ei * cos(kx * Lq(1)) * cos(ky * Lq(2)) * cos(kz * Lq(3)) * q;

% Calculation of the final pressure

Num = w * po * co * co * PsiX;
Den = Vol * ((w * co * Dnn) + j * (w * w - wn * wn));
pn = (Num / Den) * PsiY(m);
P = P + pn;

end

% Change to dB
P_dB = 20.*log10(abs(P./(Po)));

Xaxis_norm = Xaxis/Lx;
Yaxis_norm = Yaxis/Ly;

% Graphs

```

```
figure,  
surf(Xaxis, Yaxis, P_dB), colormap jet,  
ylabel('Ly'), xlabel('Lx'), zlabel('Sound Pressure Level (dB)')
```